Alma Mater Studiorum · Università di Bologna

Scuola di Scienze
Dipartimento di Fisica e Astronomia
Corso di Laurea Magistrale in Fisica

Study of the external background on the SAND detector

Relatore:

Prof. Sergio Bertolucci

Correlatore:

Dott. Matteo Tenti
Dott. Michele Pozzato

Presentata da:

Vlad Fabbri

Anno Accademico 2019/2020

Contents

Sommario **2**

Abstract **3**

Introduction **4**

1 Neutrino **7**

1.1 Neutrino mass 7
1.2 Three flavour vacuum oscillations 8
1.3 CP violation 11
1.4 Two flavour oscillation in vacuum 12
1.5 Neutrino oscillation in matter 12
1.6 Neutrino oscillation experiments 14
  1.6.1 Experimental results of neutrino oscillation parameters 16
1.7 State of the art and and pending questions in the neutrino sector 21

2 DUNE **23**

2.1 The LBNF neutrino beam 23
2.2 The DUNE detectors 25
  2.2.1 Reference Far Detector Design 25
  2.2.2 Far Detector Alternative design: Dual-Phase LArTPC 31
  2.2.3 Near Detector 33
2.3 DUNE's scientific programme 35
  2.3.1 Sensitivities and systematics 36
  2.3.2 Neutrino mass ordering and CP violation 37
  2.3.3 Precision measurements of oscillation parameters 46
  2.3.4 Proton decay measurements 47
  2.3.5 Supernova neutrino measurements 48
  2.3.6 Oscillation physics with atmospheric neutrinos 49
  2.3.7 Near Detector Physics 51

3 System for on-Axis Neutrino Detection 52
3.1 Requirements . . . 52
3.2 The SAND detector . . . 52
3.2.1 The superconducting magnet . . . 53
3.2.2 The electromagnetic calorimeter . . . 54
3.2.3 Inner tracker . . . 54
3.3 Physics program . . . 60
3.3.1 Reducing the systematic uncertainties for the neutrino oscillation studies . . . 60
3.3.2 Precise measurements and searches for new physics . . . 61

4 Simulation tools 64
4.1 General Geometry Description . . . 64
4.1.1 The ECAL geometry . . . 64
4.1.2 The STT geometry . . . 71
4.2 Neutrino MC events generator: GENIE . . . 71
4.2.1 The neutrino events generation . . . 72
4.3 EDEP-SIM: particle propagation . . . 73
4.4 Signal digitization . . . 75
4.4.1 The ECAL digitization . . . 76
4.4.2 The STT digitization . . . 78
4.5 Recontruction . . . 78
4.5.1 SAND ECAL: reconstruction . . . 79
4.5.2 The track reconstruction . . . 80

5 Selection of neutrino interaction event 83
5.1 Reconstruction of neutrino interactions . . . 84
5.1.1 Validation of the track reconstruction . . . 84
5.1.2 The vertexing algorithm . . . 89
5.1.3 Choice of *max dz*, *max IP* and *merging radius* . . . 89
5.2 Preliminary results . . . 92
5.3 Background events . . . 96
5.4 Timing cut . . . 103
5.5 Track direction cut . . . 104
5.5.1 Track length . . . 104
5.5.2 Track direction reconstruction . . . 104

Conclusions and outlooks 108

Sommario

Il Deep Underground Neutrino Experiment (DUNE) è un esperimento il cui scopo è di studiare il fenomeno delle oscillazioni dei neutrini. Sarà composto da un sistema di Near Detector (ND), situato a poche centinaia di metri dalla sorgente di neutrini al Fermi National Accelerator Laboratory (FNAL, Fermilab), e da un sistema di Far Detector (FD) composto da quattro LArTPC con una massa fiduciale di decine di migliaia di tonnellate, situato al sito Sandford Underground Research Facility (South Dakota) distante 1300 km dalla sorgente del fascio. Il System for on-Axis Neutrino Detection (SAND), che sarà uno dei tre rivelatori del sistema di Near Detector, avrà come scopo principale quello di caratterizzare e monitorare il fascio di neutrini. A tale scopo è essenziale essere in grado di distinguere le interazioni di neutrino che hanno luogo nella regione interna del rivelatore SAND da fondo dovuto ad eventi esterni. Questo lavoro di tesi è finalizzato alla definizione, implementazione e valutazione di strategie per l'identificazione di interazioni di neutrino avvenute all'interno del rivelatore SAND. Inoltre, valuto le loro prestazioni in termini di purezza e del rapporto segnale su fondo. L'identificazione si basa sia sulla topologia dell'evento e sulla ricostruzione della posizione del vertice dell'interazione del neutrino, sia sullo sfruttamento delle informazioni temporali dell'evento.

Abstract

The Deep Underground Neutrino Experiment (DUNE) will be a next generation accelerator Long-Baseline experiment. It will be composed of a Near Detector (ND) system, located a few hundred meters from the neutrino source at the Fermi National Accelerator Laboratory (FNAL, Fermilab), and a Far Detector (FD) system composed of four multi-kiloton LArTPCs, located at the Sandford Underground Research Facility site (South Dakota) 1300 km far from the beam source. The System for on-Axis Neutrino Detection (SAND), that is one of three detectors of the Near Detector system, will have as its main purpose to to characterize and monitor the neutrino beam. For this purpose it is essential to distinguish the neutrino interactions occurring inside the internal volume of the SAND detector from the external background. In this work of thesis I define and implement strategies for the identification of neutrino interactions occurring in the internal region of the SAND detector. Moreover, I evaluated their performance in terms of purity and signal-to-background ratio. The identification is based both on the topology of the event, on the reconstruction of the neutrino interaction vertex position and on the time information of the events.

Introduction

The discovery of the neutrino oscillation phenomenon is one of the most direct evidence that the Standard Model of particle physics is an incomplete theory and so must be reviewed. Even if the knowledge of neutrino oscillations have increased a lot thanks to dedicated experiments that measured the parameters governing this phenomenon, exploiting either the solar and atmospheric neutrino fluxes or the artificial ones produced by nuclear reactors and particle accelerators, there are still some open questions such the presence of CP-violation in the neutrino sector or the so-called neutrino mass ordering problem. DUNE will be a next-generation accelerator Long-Baseline experiment and among its aims will be to shed light on these unanswered questions. It will be composed by a Near Detector system located a few hundred meters from the neutrino source at the FNAL and a Far Detector system composed of four multi-kiloton LArTPCs located at the Sandford Underground Research Facility site (South Dakota), 1300 km far from the beam source. The ND system will be composed by three detectors: two movable subdetectors, a LArTPC and a Multi Purpose Detector (MPD) capable to measure neutrino flux and energy spectrum at off-axis positions and a fixed one, SAND. The SAND detector will consist of a superconducting solenoid magnet, a lead-scintillating fiber sampling electromagnetic calorimeter and a low density modular Straw Tube Tracker that integrates many different nuclear targets. Its main aim will be to characterize and monitor the neutrino beam. For this purpose it is essential to distinguish the neutrino interactions that take place inside the internal SAND region from external ones. The scope of this work of thesis is to study the capability of identifying the events in which the neutrino interactions take place inside the fiducial volume of the SAND detector and at the same time excluding the events in which the neutrino interactions occur outside the internal region of the SAND detector. The thesis is organized in five chapters:

- **Chapter 1** gives a brief neutrino physics theoretical overview mainly focused on the neutrino oscillation phenomenon and on the experimental of the art of the experimental results.
- **Chapter 2** describes DUNE experiment and its main physics goals.
- **Chapter 3** describes the SAND detector, its main aims and briefly its experimental physics opportunities.

- **Chapter 4** describes the softwares tools and the inputs of the Monte Carlo simulation used in this work of thesis.
- **Chapter 5** describes the study performed and the results obtained in this work of thesis.

Chapter 1

Neutrino

Neutrinos are chargeless and colorless fermions that interact with the other charged fermions and with the massive gauge bosons only via weak interactions. The knowledge of the properties of these particles has increased considerably in the last decades thanks to dedicated experiments. In the Standard Model (SM) theory neutrinos are assumed to be massless but the observation of neutrino oscillation phenomenon indicates that this assumption is wrong and thus the theory must be reviewed. In this chapter I expose the principal properties of neutrinos and I will describe the main experiments whose purpose was to shed light on neutrino features.

1.1 Neutrino mass

Neutrinos and antineutrinos, which take part in the charged current (CC) and neutral current (NC) weak interactions, are of three varieties, called also flavours: electron, muon and tau [1]. The neutrino flavour is defined by the charged lepton that the neutrino type produces in CC weak interactions:

$$\begin{aligned} \nu_e + X &\to e^- + Y \\ \nu_\mu + X &\to \mu^- + Y \\ \nu_\tau + X &\to \tau^- + Y \end{aligned} \tag{1.1}$$

In the Lagrangian a Dirac mass term

$$\mathcal{L} = m_D \left(\overline{\psi}\psi\right) = m_D \left(\overline{\psi}_L\psi_R + \overline{\psi}_R\psi_L\right) \quad \text{with } \overline{\psi}_R\psi_L = \left(\overline{\psi}_L\psi_R\right)^\dagger \tag{1.2}$$

is composed by two-components spinors ψ_L and ψ_R (also called Weyl spinors) which are the chiral components of the four-components spinor ψ [2]. As a consequence, to construct a Dirac mass term both a left and right chiral components are necessary. On the other hand, the neutrinos ν_α (antineutrinos $\overline{\nu}_\alpha$) are always product in weak interactions in left-handed (right-handed) helicity state [3]. For this reason, in the SM the right chiral component was not introduced, making impossible the construction of a Dirac mass term. As we will see in Section 1.2 the observation of neutrino flavour oscillation implies a non-null mass for neutrinos requiring an extension for the SM.

Since neutrinos are neutral, they could possibly be Majorana particles which could be described by a single Weyl spinor, ψ_L

$$\psi = \psi_L + \psi_L^C \quad \text{where } \psi_L^C = \mathcal{C}\overline{\psi}_L^T \tag{1.3}$$

implying that neutrino is its own antiparticle

$$\psi = \psi^C. \tag{1.4}$$

For Majorana particles a mass term could also be composed as:

$$\mathcal{L} = \frac{1}{2} m_M \overline{\psi}\psi^C + \text{h.c.} \tag{1.5}$$

Establishing if neutrinos are Majorana particles is still subject of investigation of many experiments. These experiments, such as Gerda, CUORE [5], search for the possible rare process called neutrinoless double β decay which could only occur in the case neutrinos are Majorana particles.

The neutrino oscillation experiments are not able of measuring the absolute value of the mass of these particles. Possible strategy are through cosmological studies, search of neutrinoless double β decay and measurements related to the β-decay kinematics. Only upper limits are reached to date.

Concerning the β-decay experiments they try to determine the neutrino mass measuring the spectrum of electrons near the end point. The most stringent limit was obtained using tritium by KATRIN [6], that improved the results of Mainz [7] and Troitzk [8].

$$\begin{aligned} m_{\nu_e} &< 1.1\,\text{eV} \quad \text{at } 90\%\,\text{CL} \quad \text{KATRIN} \\ &< 2.05\,\text{eV} \quad \text{at } 95\%\,\text{CL} \quad \text{Troitzk} \\ &< 1.3\,\text{eV} \quad \text{at } 95\%\,\text{CL} \quad \text{Mainz} \end{aligned} \tag{1.6}$$

Data from cosmological probe, such as Planck, can be used to obtain an upper limit on the sum of neutrino masses [9]; upper limit, depending on the data-set used, varies in the interval:

$$\sum_i m_j < (0.340 - 0.715)\ \text{eV} \quad \text{at } 95\% \ \ \text{CL} \tag{1.7}$$

1.2 Three flavour vacuum oscillations

The phenomenon of neutrino oscillations is a consequence of the presence of neutrino flavour mixing; the weak eigenstates (ν_e, ν_μ, ν_τ) are a linear combination of mass eigenstates (ν_1, ν_2, ν_3) according to

$$|\nu_\alpha\rangle = \sum_i U^*_{\alpha i}|\nu_i\rangle \qquad \alpha = e, \mu, \tau \qquad i = 1, 2, 3 \tag{1.8}$$

where U is the Pontecorvo-Maki-Nakagawa-Sakata (PMNS) unitary neutrino mixing matrix.

The PMNS matrix can be parametrized by 3 rotation angles and, depending on whether the neutrino are Dirac or Majorana particles, by 1 or 3 charge-parity (CP) symmetry violating phases

$$U = \begin{pmatrix} c_{12}c_{13} & sc & se^{-i\delta} \\ -s_{12}c_{23} - s_{12}s_{23}s_{13}e^{i\delta} & c_{12}c_{23} - s_{12}s_{23}s_{13}e^{i\delta} & s_{23}c_{13} \\ s_{12}s_{23} - c_{12}c_{23}s_{13}e^{i\delta} & -c_{12}s_{23} - s_{12}c_{23}s_{13}e^{i\delta} & c_{23}c_{13} \end{pmatrix} \times \mathrm{diag}\left(1, e^{i\frac{\alpha_{21}}{2}}, e^{i\frac{\alpha_{31}}{2}}\right) \tag{1.9}$$

where, $c_{ij} = \cos\theta_{ij}$, $s_{ij} = \sin\theta_{ij}$, $\theta_{ij} = \left[0, \frac{\pi}{2}\right]$ are the mixing angles, $\delta = [0, 2\pi]$ is the Dirac CP violation phase and α_{21}, α_{31} are two Majorana CP violation phases that are present only if neutrinos are Majorana particles.

The Hamiltonian of a neutrino mass eigenstate $|\nu_k\rangle$ can be written as

$$H|\nu_k\rangle = E_k|\nu_k\rangle \tag{1.10}$$

with energy eigenvalues

$$E_k = \sqrt{\vec{p}^2 + m_k^2}. \tag{1.11}$$

Substituting Eq. 1.10 into the Schrödinger equation (in natural units)

$$i\frac{d}{dt}|\nu_k(t)\rangle = H|\nu_k(t)\rangle \tag{1.12}$$

we derive that neutrino mass eigenstate state evolves in time as plane waves:

$$|\nu_k(t)\rangle = e^{-iE_kt}|\nu_k\rangle \tag{1.13}$$

The time evolution of a flavour state $|\nu_\alpha(t)\rangle$, which describes a neutrino created with a definite flavour at time $t = 0$, is obtained substituting Eq. 1.13 into Eq. 1.8 and reads:

$$|\nu_\alpha(t)\rangle = \sum_k U^*_{\alpha k}e^{-iE_kt}\nu_k. \tag{1.14}$$

with

$$|\nu_\alpha(t = 0)\rangle = |\nu_\alpha\rangle \tag{1.15}$$

Inverting the Eq. 1.8, $|\nu_k\rangle$ can be expressed in terms of flavour eigenstates

$$|\nu_k\rangle = \sum_\alpha U_{\alpha k} |\nu_\alpha\rangle \tag{1.16}$$

Substituting Eq. 1.16 in Eq. 1.14 we obtain

$$|\nu_\alpha(t)\rangle = \sum_{\beta=e,\mu,\tau} \left(\sum_k U^*_{\alpha k} e^{-iE_k t} U_{\beta k} \right) |\nu_\beta\rangle. \tag{1.17}$$

The transition probability between two different neutrino flavours is

$$P_{\nu_\alpha \to \nu_\beta}(t) = |\langle \nu_\beta | \nu_\alpha(t)\rangle|^2 = \sum_k U^*_{\alpha k} U_{\beta k} U_{\alpha j} U^*_{\beta j} e^{-i(E_k - E_j)t} \tag{1.18}$$

Since, due to its tiny mass, neutrinos are always ultrarelativistic, we can approximate the energy as

$$E_k \simeq E + \frac{m_k^2}{2E} \tag{1.19}$$

so that the term $E_k - E_j$ in the Eq. 1.18 becomes

$$E_k - E_j = \frac{\delta m^2_{kj}}{2E} \tag{1.20}$$

where $\delta m^2_{kj} = m^2_k - m^2_j$ and $E = |\vec{p}|$ is the neutrino energy. Since ultrarelativistic neutrinos propagate at the speed of light, we can approximate $t = L$. Hence the neutrino oscillation probability becomes:

$$P_{\nu_\alpha \longrightarrow \nu_\beta}(L, E) = \sum_{k,j} U^*_{\alpha k} U_{\beta k} U_{\alpha j} U^*_{\beta j} \mathrm{exp} \left(-i \frac{\delta m^2_{kj} L}{2E} \right) \tag{1.21}$$

Therefore, the oscillation probability depends on the squared mass differences δm^2_{kj}, the mixing angles θ_{ij} and the CP violating phase δ. As said there is no dependence on the absolute value of the mass eigenstates m_i, making impossible measuring these values in the neutrino oscillation experiments. In the three flavour mixing model only two of the three differences are independent: Δm^2_{31} and Δm^2_{21}, which are often referred to as atmospheric and solar mass differences. Since the sign of $|\Delta m^2_{31}|$ is unknown, there are two consistent scenarios for what concerns the ordering of the neutrino mass eigenvalues: the normal ordering (NO) and the inverted ordering (IO). In the normal mass ordering the mass eigenstates are ordered as $m_1 < m_2 < m_3$, in the inverted one as $m_3 < m_2 < m_1$ (Fig. 1.1).

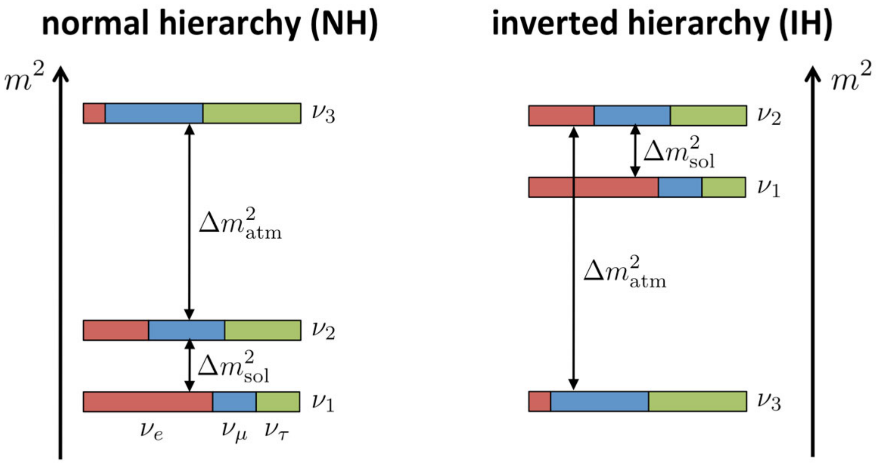

Figure 1.1: Normal (left) and inverted (right) ordering of the neutrino mass eigenvalues. The flavour composition of the three mass eigenstates is showed dividing the bars into colors: red for the ν_e, blue for the ν_μ and green for the ν_τ

1.3 CP violation

The CP violation in the neutrino sector manifests as a difference between $\nu_\alpha \to \nu_\beta$ and $\bar{\nu}_\alpha \to \bar{\nu}_\beta$ oscillation probabilities:

$$\Delta P^{CP}_{\alpha\beta} = P(\nu_\alpha \to \nu_\beta) - P(\bar{\nu}_\alpha \to \bar{\nu}_\beta) \quad \alpha \neq \beta \text{ with } \alpha, \beta = e, \mu, \tau. \tag{1.22}$$

As a consequence of the CPT theorem a CP asymmetry implies a T asymmetry allowing to have an other observable

$$\Delta P^{T}_{\alpha\beta} = P(\nu_\alpha \to \nu_\beta) - P(\nu_\beta \to \nu_\alpha) \quad \alpha \neq \beta \text{ with } \alpha, \beta = e, \mu, \tau. \tag{1.23}$$

In the three flavour mixing model, the CP violation magnitude can be expressed using the Jarlskog invariant J:

$$\Delta P^{CP}_{\alpha\beta} = -16 J^{CP}_{\alpha\beta} \sin\left(\frac{\Delta m^2_{21}}{4E} L\right) \sin^2\left(\frac{\Delta m^2_{31}}{4E} L\right) \tag{1.24}$$

where

$$J_{\alpha\beta} = \mathrm{Im}\left[U_{\alpha 1} U^*_{\alpha 2} U^*_{\beta 1} U_{\beta 2}\right] = \pm c_{12} s_{12} c_{23} s_{23} c^2_{13} s_{13} \sin\delta. \tag{1.25}$$

From Eq. 1.24 - 1.25 we observe that to have CP (or T) violation, all the three mixing angles should be not-null. The magnitude of the CP violation is still unknown since the value of the Dirac phase is still unknown [4]. In order to have significant effects due to CP violation, large values of $\sin\left(\frac{\Delta m^2_{31}}{4E}L\right)$ and $\sin\left(\frac{\Delta m^2_{21}}{4E}L\right)$ are needed. As a consequence, the experiments that search for CP asymmetry in neutrino oscillations have baseline and neutrino energy optimized to enhance the effects, as explained in Section 1.6.

1.4 Two flavour oscillation in vacuum

Many experiments are sensitive to oscillations driven by one single squared mass difference. In this case, the so called two flavour approximation, in which only two flavours are considered [2], can be applied. In this approximation the unitary transformation can be parameterized as:

$$\begin{pmatrix} \nu_e \\ \nu_\mu \end{pmatrix} = \begin{pmatrix} \cos\theta & \sin\theta \\ -\sin\theta & \cos\theta \end{pmatrix} \begin{pmatrix} \nu_1 \\ \nu_2 \end{pmatrix} \tag{1.26}$$

The transition probability can be obtained exploiting the formulas of the Section 1.2

$$P(\nu_e \to \nu_\mu) = \sin^2 2\theta \times \sin^2\left(\frac{\Delta m^2 L}{4E}\right). \tag{1.27}$$

The survival probability, that is the probability to observe the neutrino with the same flavour as the one with which it was created, is simply

$$P(\nu_e \to \nu_e) = 1 - P(\nu_e \to \nu_\mu). \tag{1.28}$$

The oscillation term can be rewritten as

$$\sin^2\left(\frac{\Delta m^2 L}{4E}\right) = \sin^2\left(\pi\frac{L}{L_0}\right) \tag{1.29}$$

with

$$L_0 = 4\pi\frac{E}{\Delta m^2} \tag{1.30}$$

where L_0 is the oscillation length and describes the length of a complete oscillation. This parameter is directly proportional to energy E and inversely proportional to the squared mass difference Δm^2. When the oscillation probability is maximal, i.e. $L = \frac{L_0}{2}$ ($E = \frac{\Delta m^2}{2}$) the oscillation amplitude is given only by the value of $\sin^2\theta$. From the Fig. 1.2 it can be noticed that if $\Delta m^2 L/2E \ll 1$ the oscillation probability is very small whereas if $\Delta m^2 L/2E \gg 1$, due to the finite experimental energy resolution, only the averaged transition probability, given by $\sin^2\theta/2$, can be measured.

1.5 Neutrino oscillation in matter

The neutrino oscillation probability in matter is different from that in vacuum due to the weak coherent scattering that neutrinos could have with the particles of the medium.

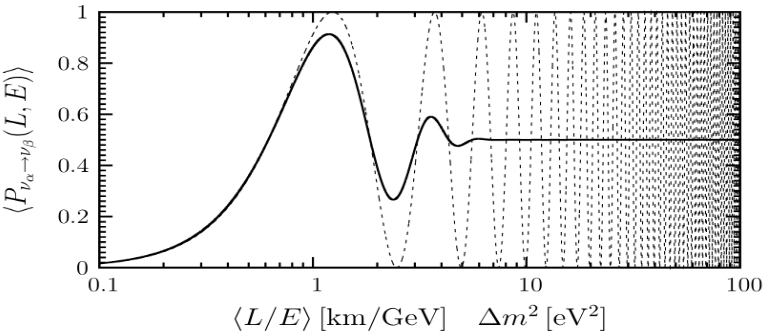

Figure 1.2: ν_α to ν_β transition probability as function of $\langle L/E \rangle$ with $\sin^2\theta$=1 (dashed line). Transition probability averaged on $\sigma = 0.2\langle L/E \rangle$ Gaussian distribution of L/E (continuous line).

Neutrinos can interact through neutral current (NC) interaction with the matter components (protons, neutrons and electrons) but, differently from muon and tau neutrinos, the electron ones can also have coherent charged current (CC) interactions [4]. Consequently, the Hamiltonian of the electron neutrinos has an extra potential term::

$$V_{CC} = \pm\sqrt{2} G_F N_e \tag{1.31}$$

where N_e is the electron density in the medium, G_F is the Fermi constant and the sign is positive for neutrinos and negative for antineutrinos. The Feynman diagram of the two processes are showed in Fig. 1.3.

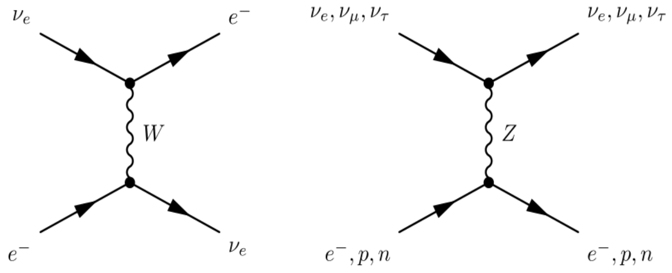

Figure 1.3: Feynmann diagram of CC electron neutrino interactions $\nu_e + e^- \to \nu_e + e^-$ (left) and of NC neutrino interactions $\nu_\alpha + e^- \to \nu_\alpha + e^-$

Considering for simplicity the case of oscillation between two families, the effective Hamiltonian which governs the propagation of neutrinos in matter, $\mathcal{H}_m$, contains an extra ν_e-ν_e element with respect to the vacuum one and can be written as

$$\mathcal{H}_m = \frac{\Delta m_m^2}{4E} \begin{pmatrix} -\cos 2\theta & \sin 2\theta \\ \sin 2\theta & \cos 2\theta \end{pmatrix} + \begin{pmatrix} V_{CC} & 0 \\ 0 & 0 \end{pmatrix}. \tag{1.32}$$

In the simple case where the matter density is constant, we can then diagonalize $\mathcal{H}_m$ to obtain an effective mixing matrix and mass eigenstates [11]. We can then denote the effective parameters as θ_m and Δm_m^2 and the oscillation probability becomes:

$$P(\nu_e \to \nu_\mu) = \sin^2 2\theta_m \sin^2\left(\frac{\Delta m_m^2 L}{4E}\right) \tag{1.33}$$

where

$$\Delta m_m^2 = C\Delta m^2, \qquad \sin 2\theta_m = \frac{\sin 2\theta}{C} \tag{1.34}$$

with

$$C = \sqrt{(\cos 2\theta - A)^2 + \sin 2\theta}, \qquad A = \frac{2\sqrt{2}G_F N_e E}{\Delta m^2}. \tag{1.35}$$

This is MSW effect named after Mikhaev, Smirnov and Wolfenstein which first predicted it [12, 13]. From these last formulas we can conclude that:

- Long-Baselines are needed to observe significant effects (if $\Delta m_m^2 L/4E \ll 1$ we find the vacuum oscillation probability).
- For the resonance condition, i.e. $A = \cos 2\theta$, the oscillation probability is enhanced respect to the vacuum one.
- The oscillation probability can be quite different between neutrinos and antineutrinos even in case of CP symmetry conservation due to the sign of the V_{CC}.
- The oscillation probability depends on Δm^2 and in particular on its sign

The last consequence is very important because it can be exploited to determine the neutrino mass ordering.

1.6 Neutrino oscillation experiments

The vast variety of neutrino oscillation experiments can be classified based on which type of measure is performed:

- Appearance experiments: when neutrinos flavour not initially present in the beam are searched for.
- Disappearance experiments: these experiments measure the survival probability of a neutrino flavour counting the number of interactions into the detector and comparing it with the expected one in the non oscillation hypothesis.

The second way to group neutrino experiments is based on the neutrino sources.

- Nuclear reactor: these experiments exploit the electron antineutrinos originated in the β^- decays of heavy isotopes produced in nuclear fission reactions. The antineutrinos have energies of the order of the MeV.
- Accelerator: in these experiments the detector is exposed to a beam of neutrinos produced by decays of pions, kaons and muons originated from the interaction of a proton beam with a target. The energy of the neutrinos varies from some few tens of MeV to some hundreds of GeV.
- Solar: these experiments detect neutrinos produced in the core of the Sun by thermonuclear reactions. The energy of the neutrinos is up to 15 MeV.
- Atmospheric: these experiments exploits neutrinos produced as a consequence of the interaction of the cosmic rays with the atmosphere. The energy of the neutrinos covers a wide range, from few hundreds of MeV to hundreds of GeV.

The neutrino energy and the baseline determine the mixing parameters that the experiments are sensitive to. As it was explained in Section 1.4, an experiment is sensitive to a certain value of Δm^2 if

$$\frac{\Delta m^2 L}{2E} \simeq 1. \tag{1.36}$$

So, the experiments can also be classified taking into account the value L/E, that determines which values of squared difference masses are sensitive to.

- **Short-Baseline (SBL)**: these are reactor and accelerator experiments. In the first case the experiments measure the survival probability of antineutrinos, the range of L/E covered and their sensitivity to Δm^2 are

  $$\frac{L}{E} \lesssim 1\,\mathrm{m/MeV} \quad \rightarrow \quad \Delta m^2 \gtrsim 1\,\mathrm{eV}^2 \tag{1.37}$$

  In accelerator SBL neutrino experiments the value of L/E varies depending on the energy of the beam

  $$\frac{L}{E} \lesssim 10^{-2}\,\mathrm{m/MeV} - 1\,\mathrm{km/GeV} \quad \rightarrow \quad \Delta m^2 \gtrsim 10^2\,\mathrm{eV}^2 - 1\,\mathrm{eV}^2 \tag{1.38}$$

- **Long-Baseline LBL**: in these kind of experiments the neutrino sources are the same of SBL experiments but the distances between sources and detectors are 2-3 orders of magnitude larger. In rectors LBL experiments the range is

  $$\frac{L}{E} \lesssim 10^3\,\mathrm{m/MeV} \quad \rightarrow \quad \Delta m^2 \gtrsim 10^{-3}\,\mathrm{eV}^2. \tag{1.39}$$

In the accelerator experiments the range is

$$\frac{L}{E} \lesssim 10^3 \text{ km/GeV} \quad \rightarrow \quad \Delta m^2 \gtrsim 10^{-3} \text{ eV}^2 \tag{1.40}$$

In this category are also included atmospheric neutrino experiments because of similar Δm^2 sensitiveness

$$\frac{L}{E} \lesssim 10^4 \text{ km/GeV} \quad \rightarrow \quad \Delta m^2 \gtrsim 10^{-3} \text{ eV}^2. \tag{1.41}$$

- **Very Long-BaseLine (VLB)**: these are experiments with a source-detector distance larger than LBL experiments by 10-100 times. For reactor VLB experiments the range is

  $$\frac{L}{E} \lesssim 10^5 \text{ m/MeV} \quad \rightarrow \quad \Delta m^2 \gtrsim 10^{-5} \text{ eV}^2 \tag{1.42}$$

  In the accelerator ones the range is

  $$\frac{L}{E} \lesssim 10^4 \text{ km/GeV} \quad \rightarrow \quad \Delta m^2 \gtrsim 10^{-4} \text{ eV}^2 \tag{1.43}$$

  Often solar neutrino experiments are associated with these experiments because of similar parameters sensibility

  $$\frac{L}{E} \lesssim 10^{12} \text{ m/MeV} \quad \rightarrow \quad \Delta m^2 \gtrsim 10^{-12} \text{ eV}^2 \tag{1.44}$$

1.6.1 Experimental results of neutrino oscillation parameters

θ_{12} and Δm^2_{12} experimental results

The solar neutrino experiments are predominantly sensitive to the solar mixing angle $\theta_{12} = \theta_\odot$ and the solar squared mass difference $\Delta m^2_{12} = \Delta m^2_\odot$ [10]. The two main detection techniques are: radiochemical and Cherenkov. Radiochemical experiments like Homestake, Gallex/GNO and SAGE are only sensitive to the interaction rate of electron neutrinos, but not to their energy or arrival time to the detector [15, 16, 17]. The Cherenkov technique pioneered by Kamiokande experiment [19] permits to measure neutrino interactions in real time allowing to measure the energy, direction and arrival time of the neutrino. The Kamiokande detector consisted of a tank of about 3000 t of pure water instrumented with about 1000 photomultiplier tubes positioned on the vessel walls. Another important experiment based on this technique was the Sudbury Neutrino Observatory (SNO) experiment that definitively confirms the neutrino oscillation phenomenon as the solution to the so-called solar neutrino problem [18]. Nowadays the main solar experiments still in activity are Borexino, at the Laboratori Nazionali del Gran Sasso that exploits a low background liquid scintillator detector [26] and SuperKamiokande, the evolution of the Kamiokande experiment, with an active mass of about of 50 kt pure water [20].

The experimental results obtained by solar neutrino experiments are complemented by the reactor VLB experiments. One of the most important is the KamLAND experiment, at Kamioka mines in Japan, which exploits the electronic antineutrino flux produced in several japanese nuclear reactors [27]. The allowed regions in the $\sin^2\theta_{12} - \Delta m^2_{21}$ are shown in Fig. 1.4. The best-fit values of $\sin^2\theta_{12}$ and Δm^2_{21} are displayed in Table 1.1.

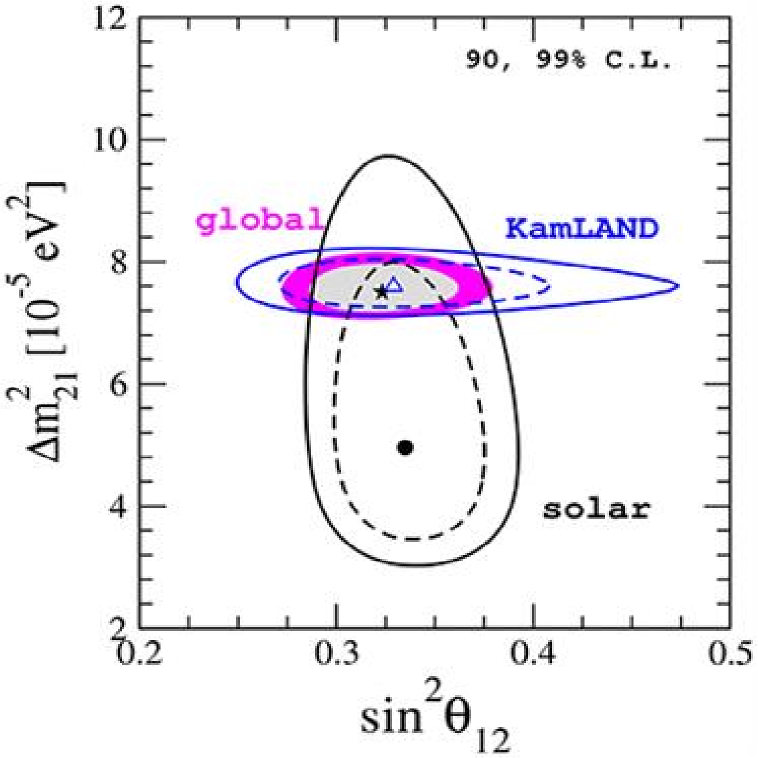

Figure 1.4: Allowed region at 90% (dashed line), and 99% (solid line) confidence level from the analysis of solar data (black), KamLAND (blue) and the global fit (colored regions) [10].

Parameter	best-fit	3σ
$\sin^2\theta_{12}$	0.297	0.250 - 0.354
Δm^2_{12} $[10^{-5}$ eV$^2]$	7.37	6.93 - 7.96

Table 1.1: Best-fit values and 3σ allowed ranges of the solar sector parameters [14].

θ_{13} experimantal results

Recently a new generations of Short-Baseline reactor neutrino experiments such as Daya Bay [29], Reno [30] and Double Chooz [31] have been able to measure the θ_{13} mixing angle. The main features of these reactor experiments are, on one hand, their increased reactor power compared to their predecessors such as CHOOZ [32] and Paloverde [33] and, on the other hand, the use of several identical detectors located at different distances from the reactor cores. The combination of these two features results in an impressive increase of detected event rate together with an enhanced control of systematic uncertainties. $\Delta\chi^2$ as a function of $\sin^2\theta_{13}$ obtained from the analysis of each single experiment and their combination, both for normal and inverted ordering, is shown in Fig. 1.5. Tables 1.2 and 1.3 report the best fit-value of θ_{13} obtained by the three experiments and by a global fit respectively.

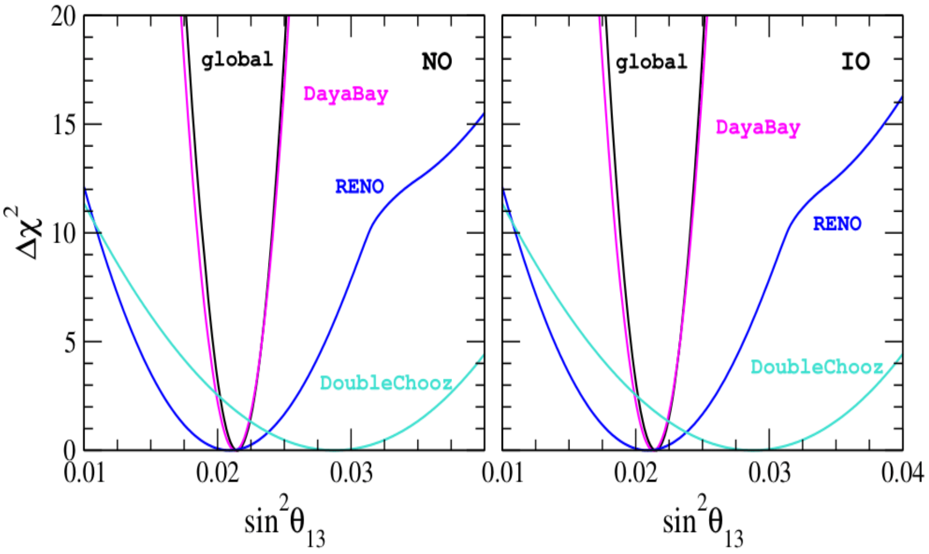

Figure 1.5: $\Delta\chi^2$ as a function of $\sin^2\theta_{13}$ obtained from the single experiments (Daya Bay, RENO and Double Chooz) and their combination. The left panel corresponds to normal mass ordering while the right panel to the inverted one [10].

Experiment	best-fit
Daya Bay	0.0841 ± 0.00027 (stat.) ± 0.00019 (syst)
RENO	0.082 ± 0.009 (stat.) ± 0.006 (syst)
Double Chooz	0.119 ± 0.0016

Table 1.2: Best fit-value of $\sin^2\theta_{13}$ obtained by the Daya Bay, Reno and DoubleChooz experiments.

Parameter	best-fit	3σ
$\sin^2\theta_{13}$, $\Delta m^2_{31} > 0$	0.0215	0.0190 - 0.0240
$\sin^2\theta_{13}$, $\Delta m^2_{31} < 0$	0.0216	0.0190 - 0.0242

Table 1.3: Best fit-values and 3σ allowed regions for $\sin^2\theta_{13}$ obtained by a global fit [14].

θ_{23} and Δm^2_{31} measurements

Several experiments have contributed to the determination of these parameters; initially in particular SuperKamiokande [20], MACRO [21] and recently also by ANTARES [22] and IceCube [23]. In Fig. 1.6 the allowed regions in the $\sin^2\theta_{23} - \Delta m^2_{31}$ plane obtained from atmospheric neutrino experiments are shown.

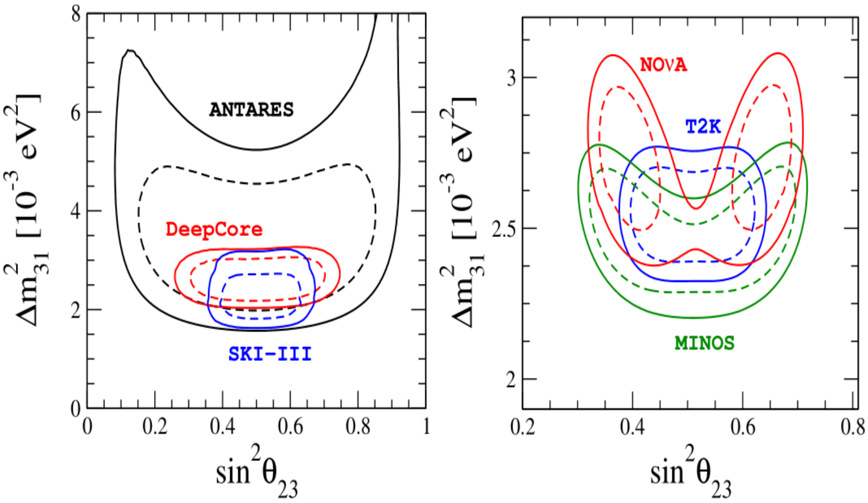

Figure 1.6: 90% and 99% C.L. (dashed line) regions in the plane $\sin^2\theta_{23} - \Delta m^2_{31}$ from atmospheric (left) and Long-Baseline accelerator (right) experiments, assuming normal mass ordering.

Parametro	best-fit	3 σ
$\sin^2\theta_{23}$, $\Delta m^2_{32} > 0$	0.425	0.381 - 0.615
$\sin^2\theta_{23}$, $\Delta m^2_{32} < 0$	0.589	0.384 - 0.636
Δm^2_{31} [10^{-3} : eV^2]	2.54	2.45 - 2.69

Table 1.4: Best-fit value and 3σ allowed ranges

The same parameters involved in the atmospheric neutrino oscillations can be studied in Long-Baseline accelerator experiments. Chronologically the first ones were the K2K [24] and the MINOS [25] experiments. They tried to probe the ν_μ disappearance oscillation channel in the same region of parameters indicated by atmospheric neutrinos. Long-Baseline experiments such as OPERA and ICARUS studied the appearance signal looking for signatures of ν_τ in beams of ν_μ. The OPERA experiment in particular found 10 ν_τ candidates confirming $\nu_\mu \rightarrow \nu_\tau$ oscillation at 5σ of confidence level [34]. Nowadays the main Long-Baseline experiments are T2K [35] and NOνA; they use ν_μ and $\overline{\nu}_\mu$ beams to study the $\nu_\mu \rightarrow \nu_\mu$ disappearance and the $\nu_\mu \rightarrow \nu_e$ appearance. The results of these experiments are shown in the right side of Fig. 1.6.

δ_{CP} measurements

As it was explained in the Section 1.3, the experiments aiming at measuring the CP violating phase are Long-Baseline accelerator experiments with ν_μ and $\bar{\nu}_\mu$ beams of energy of the order of the GeV, like the T2K and NOvA experiments. Recently the T2K experiment [35] was able to constrain the CP violating phase measuring the muon neutrino to electron neutrino oscillations and the corresponding antineutrino oscillations. Combining the reactor experiments data, the hypothesis of CP conservation ($\delta_{CP} = 0°, \pm 180°$) can be excluded at 90% confidence level for both the mass orderings. The 90% confidence level allowed region for δ_{CP} is [-2.95, -0.44] ([-1.47, -1.27]) for normal (inverted) ordering. The NOνA experiment obtained very similar results as shown in Fig. 1.7. The two best-fit values of a global analysis for the normal hierarchy are $\sin^2\theta_{23} = 0.404$, $\delta_{CP} = 1.48\,\pi$ and $\sin^2\theta_{23} = 0.623$, $\delta_{CP} = 0.74\,\pi$ and the inverted hierarchy is disfavoured at $>$ 93% confidence level [28].

Experimental results

The most recent global fit performed exploiting the results obtained by Long-Baseline experiments (NOνA, MINOS, T2K), reactor neutrino experiments (Daya Bay, RENO, Double Chooz) and solar neutrino experiments (SNO, Super-Kamiokande, Borexino), shows a growing significance towards the normal mass ordering: NO is favoured with a $\Delta\chi^2$ of 4.7 (Fig. 1.8). The indications become more stronger ($\Delta\chi^2 = 9.3$) if the data from the SuperKamiokande experiment are included in the analysis.

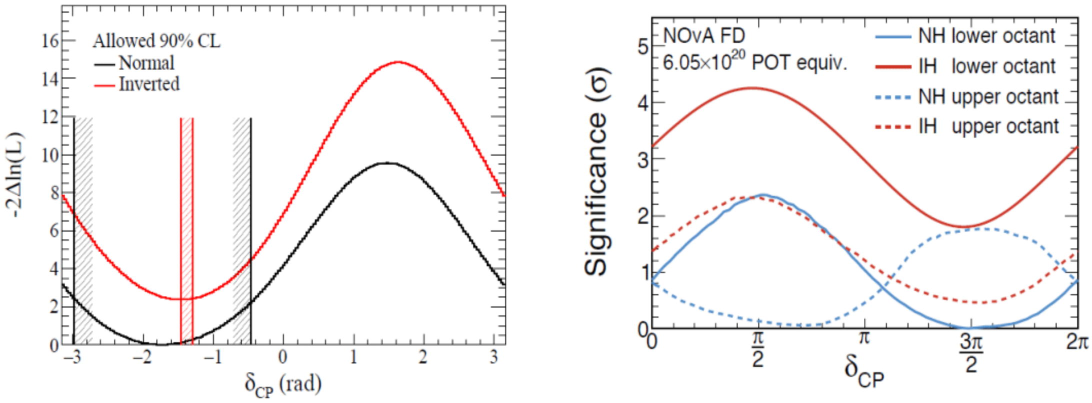

Figure 1.7: (Left) Negative log-likelihood as a function of δ_{CP} with 90% CL for normal (black) and inverted (red) ordering obtained by the T2K experiment. (Right) Significance as a function of δ_{CP} obtained by the NOνA experiment for NO and HI and for the two θ_{23} octants.

1.7 State of the art and and pending questions in the neutrino sector

Even if neutrino physics is now entering in its precision era, there are some pending questions still unanswered:

- The determination of the absolute mass of neutrinos and its origin (Majorana or Dirac);
- The measurement of the possible CP asymmetries in the leptonic sector;
- The determination of the mass ordering.

Among the Long-Baseline accelerator experiments DUNE will be the main neutrino oscillation experiment of the Fermi National Accelerator Laboratory (FNAL). Having access to MSW effect and to a neutrino beam capable of producing both ν_μ and $\overline{\nu}_\mu$, DUNE will be suitable to determine the mass ordering and possibly to observe CP violations. The description of the experiment and its goal will be the main subject of the Chapter 2.

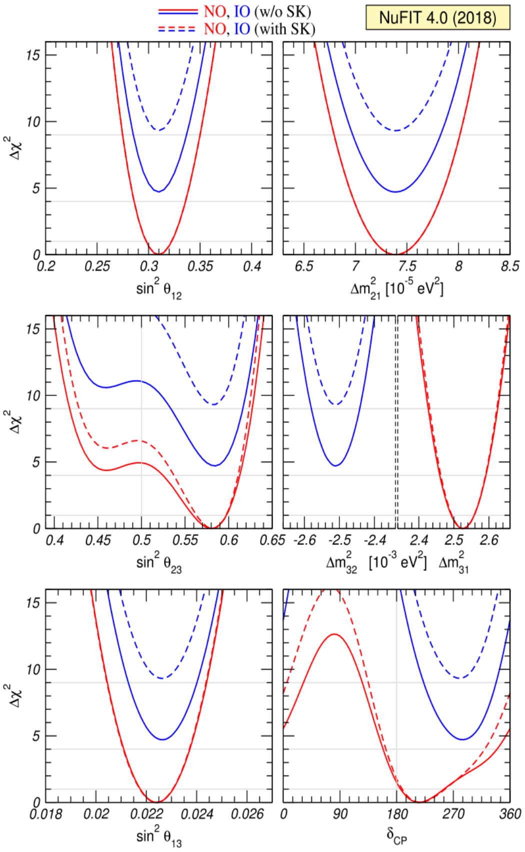

Figure 1.8: $\Delta\chi^2$ profile obtained from global analysis assuming the three neutrino mixing. The profiles are minimized in all non displayed parameters. The red (blue) full curves correspond to Normal (Inverted) Ordering. Solid (dashed) curves are without (with) adding the data from SuperKamiokande [14].

Chapter 2

DUNE

The Deep Underground Neutrino Experiment (DUNE) will be a new generation neutrino Long-Baseline experiment designed to bring fundamental contributions to neutrino physics, together with the capability to study supernovae in our galaxy detecting neutrinos coming from their collapses and to investigate proton decay channels predicted by Grand Unified Theories. The three main components of the experiment are:

- the neutrino beamline, located at the Fermi National Accelerator Laboratory (FNAL) and capable to produce both neutrino and antrineutrino beams;
- the Near Detector complex will characterize the neutrino beam before neutrino oscillations occur;
- the Far Detector, consisting of four similar 17-kt liquid Argon TPC, will be located at the Sandford Underground Research Facility site (South Dakota), 1300 km downstream of the source and 1.5 km underground.

Sections 2.1 and 2.2 are devoted to fully describe the DUNE main components while in Section 2.3 the scientific program is reported.

2.1 The LBNF neutrino beam

The LBNF Neutrino Beamline at Fermilab is designed and optimized to deliver the world's most intense neutrino beam. A schematic layout of the beamline is shown in Fig. 2.1. A proton beam with an energy range from 60 to 120 GeV is extracted from the Fermilab Main Injector and directed towards a target. The main parameters of the primary beam are listed in Table 2.1. Approximately 85% of the protons interact with the target producing mainly pions and kaons that are then sign-selected and focused by a set of magnetic horns into a 200 m long decay pipe, where they decay into muons and neutrinos. The energy spectrum of the resulting neutrino beam covers the first and

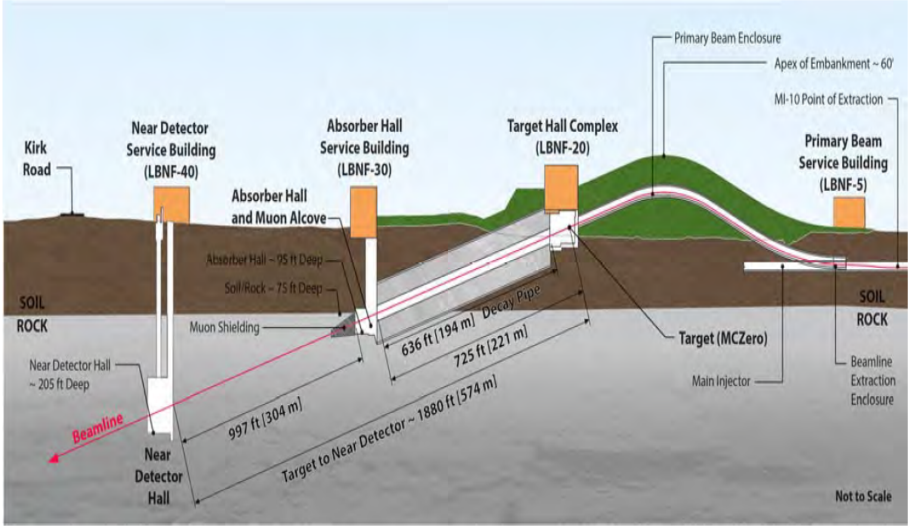

Figure 2.1: Schematic representation of the neutrino beamline [39].

Parameter	Value	
Energy	60 GeV	120 GeV
Protons per cycle	7.5×10^{13}	7.5×10^{13}
Spill duration	1.0×10^{-5} sec	1.0×10^{-5} sec
Protons on target per year	1.9×10^{21}	1.1×10^{21}
Cycle time	0.7 sec	1.2 sec
Beam Power	1.03 MW	1.2 MW
Beam size at target	1.5 to 1.7 mm	
Δ p/p	11×10^{-4} 99% $(28 \times 10^{-4}$ 100%)	
Transverse emittamnce	30π μm 99% (360π μm 100%)	
Beam divergence (x,y)	17 to 15 μrad	

Table 2.1: Summary of primary beam parameters for different values of proton energy

second oscillation maxima at 2.5 and 0.8 GeV for a 1300 km baseline. Inverting the horn current polarity both ν_μ or $\bar{\nu}_\mu$ beams with small contamination of ν_e, $\bar{\nu}_e$ and "wrong sign" muon neutrinos can be produced. The expected neutrino unoscillated fluxes at FD site with the 120 GeV proton beam are shown in Fig. 2.2, both for the horn positive and negative current polarity.

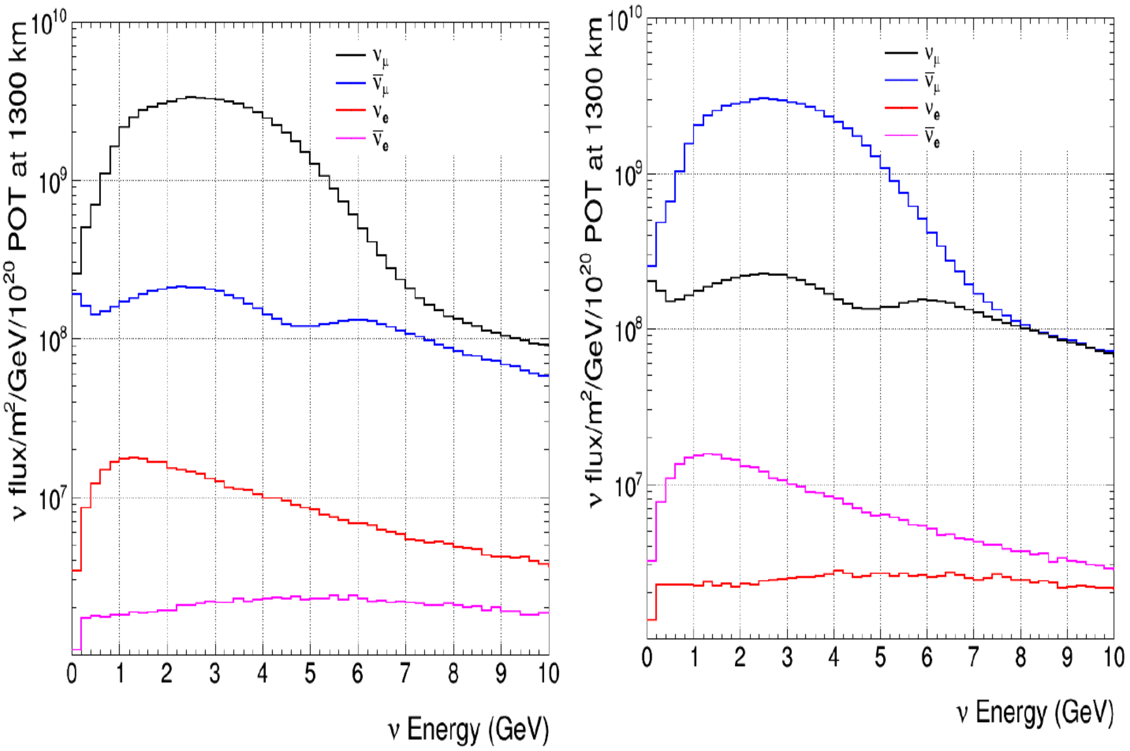

Figure 2.2: Expected unoscillated fluxes at the Far Detector produced with the 120 GeV proton beam and positive (left) and negative (right) horn current polarity [39].

2.2 The DUNE detectors

2.2.1 Reference Far Detector Design

The reference design of the DUNE FD consists of four Liquid Argon Time Projection Chamber (LArTPC) detectors each with a fiducial mass of 10 kt. In Fig. 2.3 and Fig. 2.4 an external and internal representations of a reference LArTPC module are shown. The LArTPC technology is a natural choice since its excellent tracking and calorimetry performances are very suitable for a neutrino experiment, such DUNE, where high signal efficiency, effective background discrimination, capability to identify and precisely measure neutrino events over a wide range of energies and high resolution reconstruction of kinematic properties are needed. Crossing a LAr volume the charged particles produce ionization charge and scintillation light. The fast scintillation light at 128 nm, once shifted into the visible spectrum, is collected by photon detectors providing an initial start time (t_0) for every event recorded by the TPC. The electron drifts in a constant electric field towards the segmented anode plane. On the other hand, the comparison of the arrival time of the ionization signal with t_0 allows the reconstruction of the event topology in the drift coordinate.

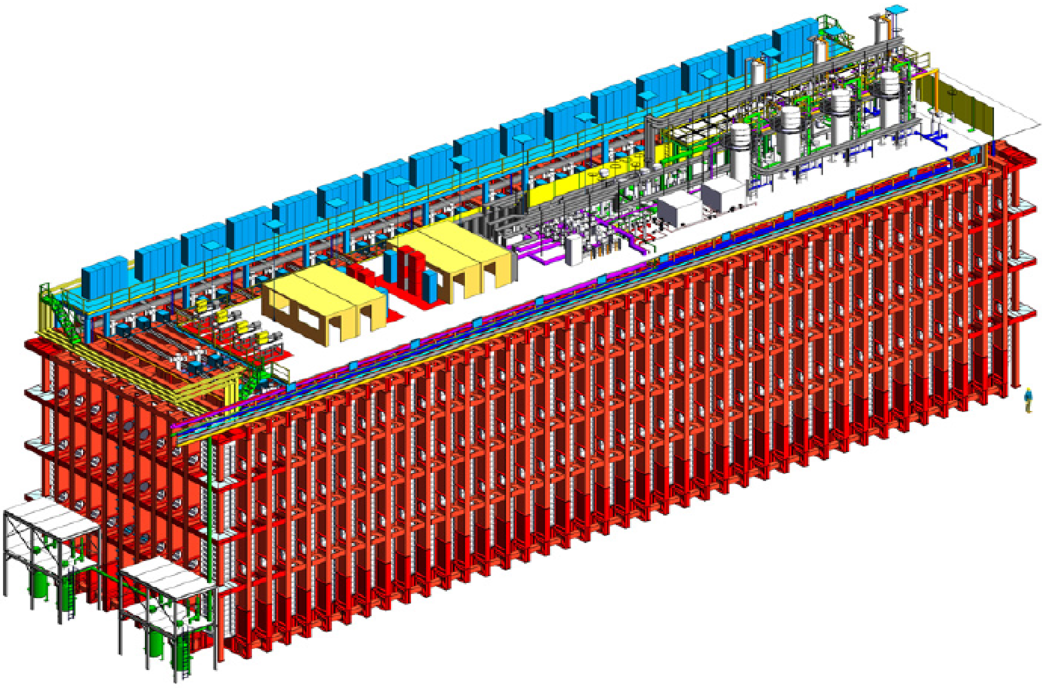

Figure 2.3: Illustration of a Reference Far Detector module seen from outside

Time Projection Chamber

The Time Projection Chamber is the key active detector of each DUNE Far Detector module. It is located in the cryostat vessel and it is completely submerged in LAr at 88 K. The TPC active volume is 12 m high, 14.5 m wide and 58 m long in the beam direction and it is composed of modular Anode Plane Assembly (APA), Cathode Plane Assembly (CPA) and field-cage modules. The APAs and CPAs are assemblies of wire planes and they are tiled into rows along the length of the cryostat to form 3 anode planes and 2 cathode planes parallel to the beam direction, as showed in Fig. 2.5.

Each APA is 2.3 m wide, 6 m high and 12 cm thick; two APAs are stacked vertically to cover the whole height of the TPC active volume. 25 of these stacks are placed side by side to form an anode plane filling the whole active volume length. The CPAs have the same width but half the height as an APA, so 4 CPA are stacked vertically to fill the active volume height. The drift volumes are surrounded by a field cage that ensures uniformity of the E field within that volume. The APAs consist of 4 wire layers wrapped on each side of a frame of lightweighted, rectangular stainless steel tubing: from outside

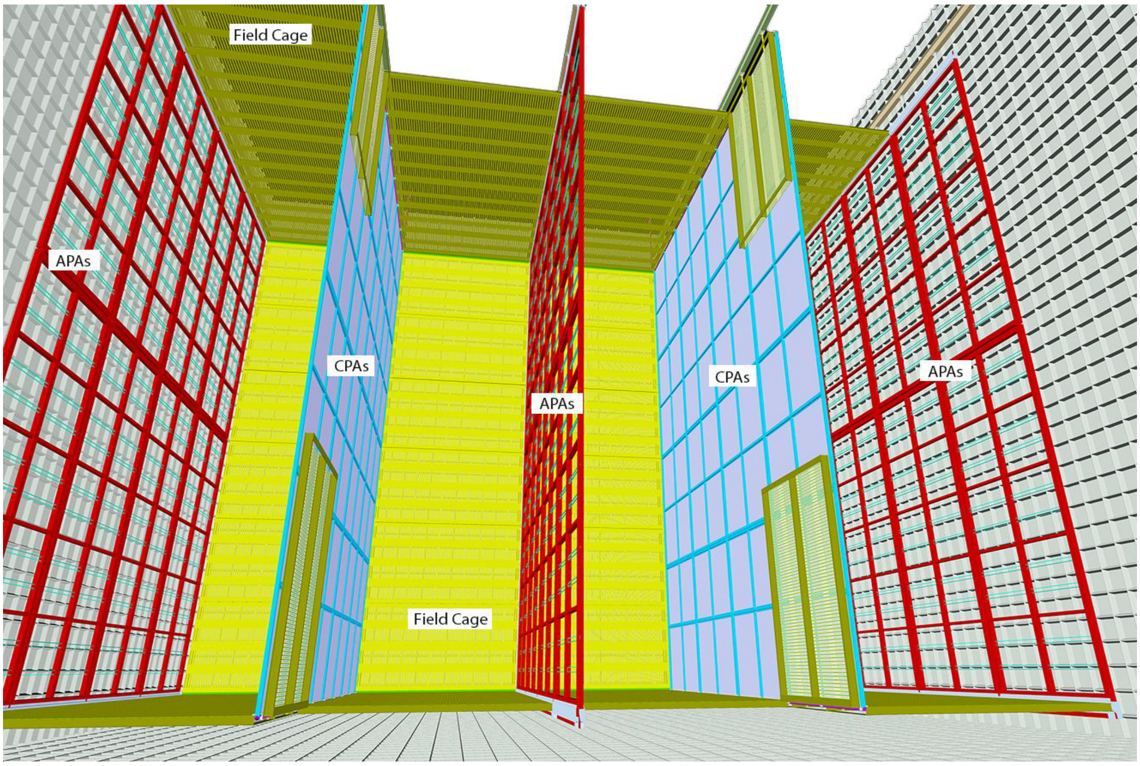

Figure 2.4: Illustration of a Reference Far Detector module seen from inside

we find a shielding plane (G), two induction planes (U and V), and the collection plane (X). The wiring scheme is shown in Fig. 2.6. Specific voltages are applied to the APAs and to the CPAs in order to form an electric field, perpendicular to the cathode and the anode planes, kept uniform by the field cage modules. When a charged particle traverses the volume between an anode and a cathode plane it produces a trail of ionization; the electrons drift toward the closest anode plane inducing a current signal to the front-end electronics circuits connected to the sensing wires. The maximum electron-drift distance between a cathode and an adjacent anode is 3.6 m and this requires that the cathode planes are set to a -180 kV bias voltage to reach the 500 V/cm nominal drift field. Different voltages are applied to the APA's wire layers in order to grant the ionization electrons drift toward the first three wire layers and they are collected into the collection plane X (see Table. 2.2). The waveforms are then digitized and transmitted through cold cables submerged in the liquid Argon to data acquisition system outside the cryostat. The DAQ is required to collect data of beam and atmospheric neutrino and of proton decay candidates with a very high uptime (the goal is $> 99\%$). For this reason each Far Detector modules has its own independent DAQ to reduce dead time.

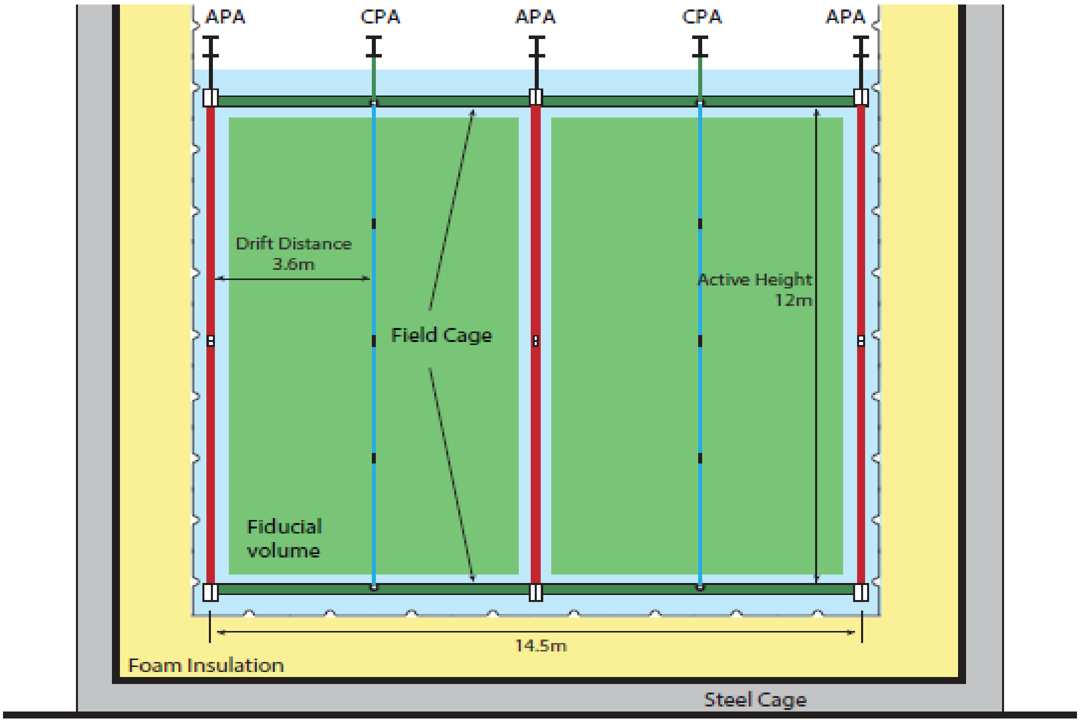

Figure 2.5: Front view of a TPC module of Dune Far Detector. The beam is perpendicular to this view [40].

Label	Function	Orientation	Bias Voltage (V)
G	Shield Plane	0°	-665
U	Induction plane	+35.7°	-370
V	Induction plane	−35.7°	0
V	Collection plane	0	+820

Table 2.2: The parameters of the APA wire planes [40].

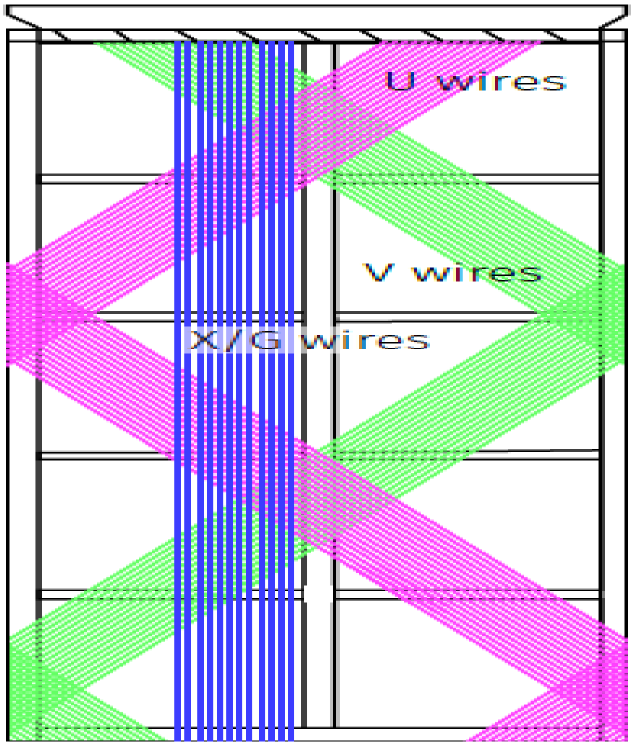

Figure 2.6: Illustration of the APA wire wrapping scheme [40].

Photon Detection System

The mean energy needed to produce a photon in LAr at zero field is 19.5 eV, so a charged particle passing through LAr produces a lot of light (40000 photons/MeV) at 128 nm. When an electric field is applied to the LAr, as in the Far Detector TPCs, about a fourth of the photons produced are promptly emitted with an average lifetime of about 6 ns, while the others have a lifetime of 1110-1600 ns. The fast components of the emitted light so arrive at the photon detectors (PDs) nanoseconds after production, providing a t_0 for each events.

The photons are collected by devices called X-ARAPUCAs mounted in the APA. They consist of layers of dichroic filter and wavelength-shifter that shift the VUV scintillation light into the visible range, trap the visible photons and transport them to SiPMs devices. In Fig. 2.7 the XARAPUCA cell is shown. PD modules are 209 cm×12 cm×2 cm bars and each hold 24 X-ARAPUCAs cells; on each of this module 48 SiPMs detect the light from the 24 cells. Ten PD modules are mounted in each APA between the wire layers, as it is shown in Fig. 2.8

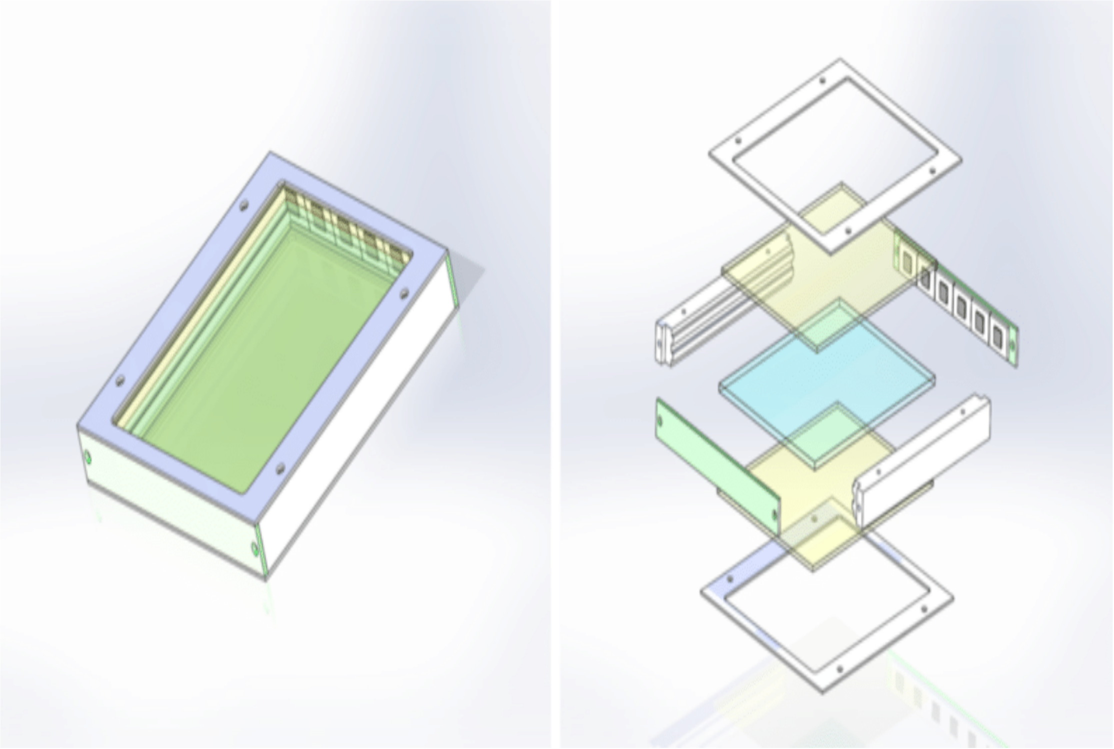

Figure 2.7: (Left) An X-ARAPUCA module. (Right) An exploded view of the X-ARAPUCA cell; the blue sheet is the wavelength-shifting (WLS) plate while the yellow sheets are the dichroic filters [42].

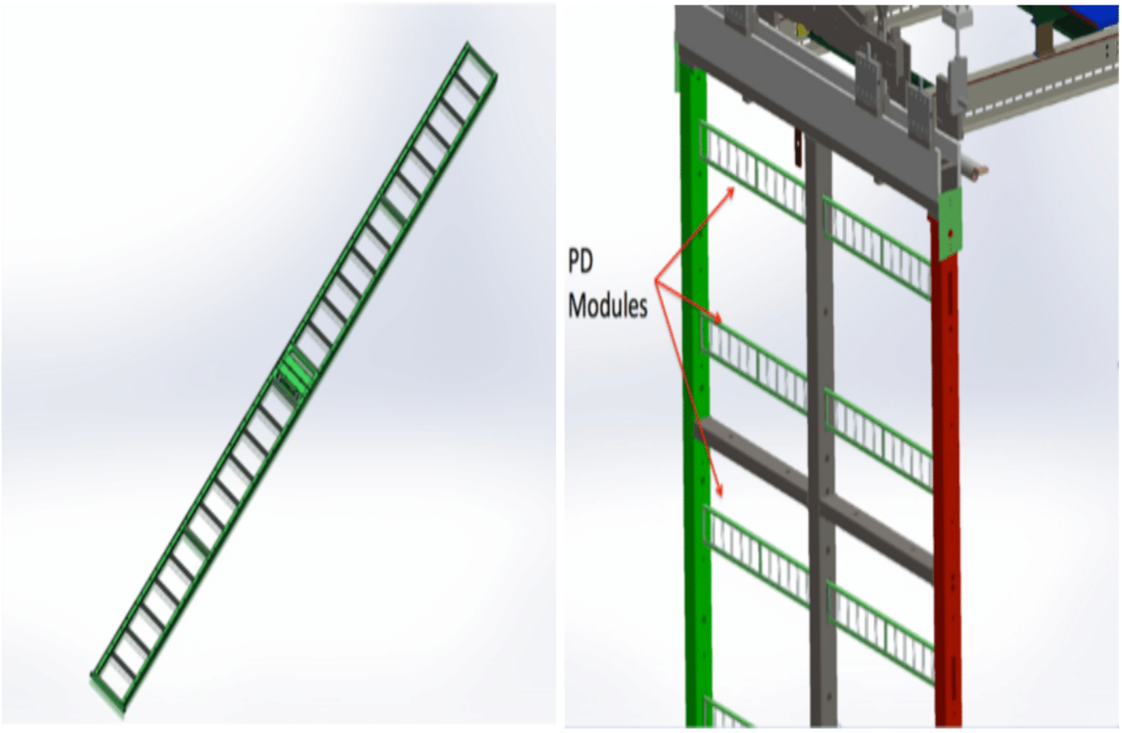

Figure 2.8: (Left) An X-ARAPUCA PD module. The 48 SiPMs that detect the light from the 24 cells are along edges of the module. (Right) X-ARAPUCA PD modules mounted inside an APA [42].

2.2.2 Far Detector Alternative design: Dual-Phase LArTPC

The Dual-Phase (DP) LArTPC is a possible alternative design for one Far Detector module. A representation of this design module is shown in Fig. 2.10. The key feature is that the ionization signal, produced in LAr, is amplified in an avalanche process that occurs in a region where there is gaseous Ar. The DP LArTPC consists of a tank of fully homogeneous liquid Argon in which the ionization electrons drift vertically upward towards an extraction grid placed just below the gaseous Argon volume. The ionization signal is amplified and collected on a finely segmented anode. The operating principle of a DP LArTPC is illustrated in Fig. 2.9. This design offers several advantages over the reference one such as an higher gain that leads to an improved signal-to-noise ratio, larger fiducial volume, lower detection threshold and the absence of dead material in the LAr volume.

An electric field of 2 kV/cm is applied between the extraction grid, composed by two perpendicular set of evenly-spaced stainless steel wires of 0.1 mm in diameter with 3.125-mm pitch, and the charge amplification devices, called large electron multipliers

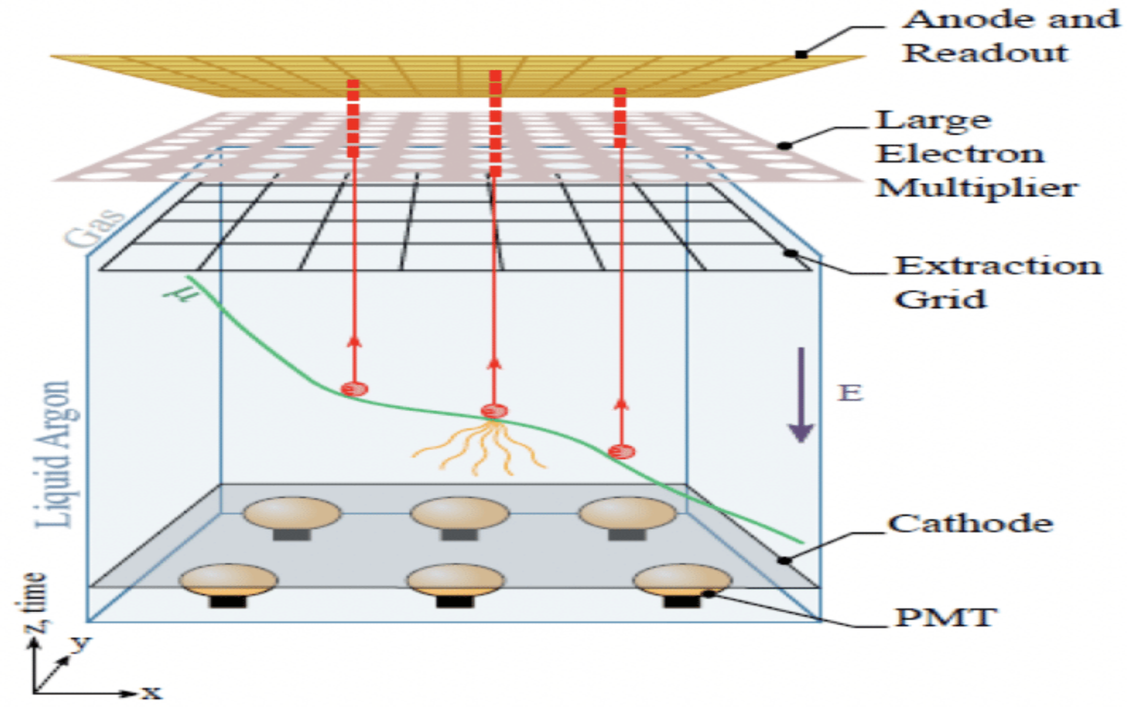

Figure 2.9: Operating principle of the DP read-out

(LEMs), in order to ensure a 100% extraction efficiency. The LEMs are 1-mm-thick printed circuit boards with electrodes on the top and bottom surfaces. A voltage of 3 kV is applied between the electrodes inducing electron avalanches; the charge is then collected in a finely 2D segmented readout anode plane on the top of the gas volume. The extraction grid, the LEMs and the anode elements are combined in arrays of independent modules called Charge Readout Planes (CRPs) that are embedded in a frame of FR4 and stainless steal. Each CRP is suspended to the tank top deck. Combined with the LAr scintillation readout by PMTs arrays that ensures timing information, CPR provides 3D tracking imaging. The electric signal formed by the collected charges is passed outside the tank via a set of feedthrough elements called "Chimneys".

The drift field ($E_{drift} \simeq 0.5$ kV/m) is produced applying an high voltage to the cathode plane that is located on the bottom of the tank and it is kept uniform by the field cage, consisting of 60 equally spaced electrodes with an applied voltage that decreases from the bottom to the top of the TPC. The design is then completed by an external cryostat.

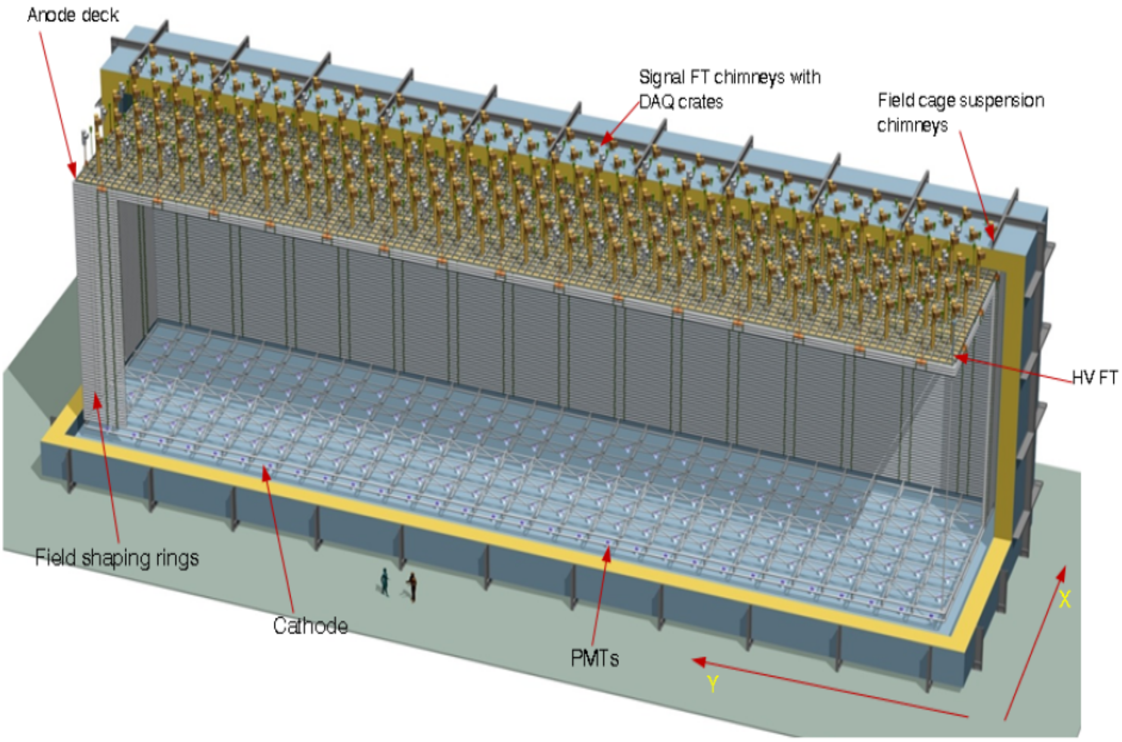

Figure 2.10: A representation of the alternative dual-phase LArTPC design module of the Far Detector

2.2.3 Near Detector

The Near Detector will be located at the Fermilab and will consists of three elements: two movable subdetectors, a LArTPC and the Multi Purpose Detector (MPD) which aim to measure neutrino flux and energy spectrum at off-axis positions, and a fixed one, System for on-Axis Neutrino Detection (SAND). The two movable detectors will use the Ar as target material to reduce the systematics uncertainties on the neutrino cross-section.

The LArTPC, also referred to as ArgonCube [44] [43], will consist of several identical modules in a common tank of liquid Argon; each of them includes two different TPCs with a 0.33 m drift length, two independent pixel charge readout planes and light detection systems. Such a configuration ensure a relatively large active volume with short drift length requiring less stringent requirements on LAr purity. The dimensions of the ArgonCube will be 7m-wide × 3m-high × 5m-deep. A representation of the ArgonCube and of a single module is shown in Fig. 2.11.

The MPD is placed downstream of the ArgonCube detector; it consists of an high pressure gaseous time projection chamber (HPgTPC) surrounded by an electromagnetic

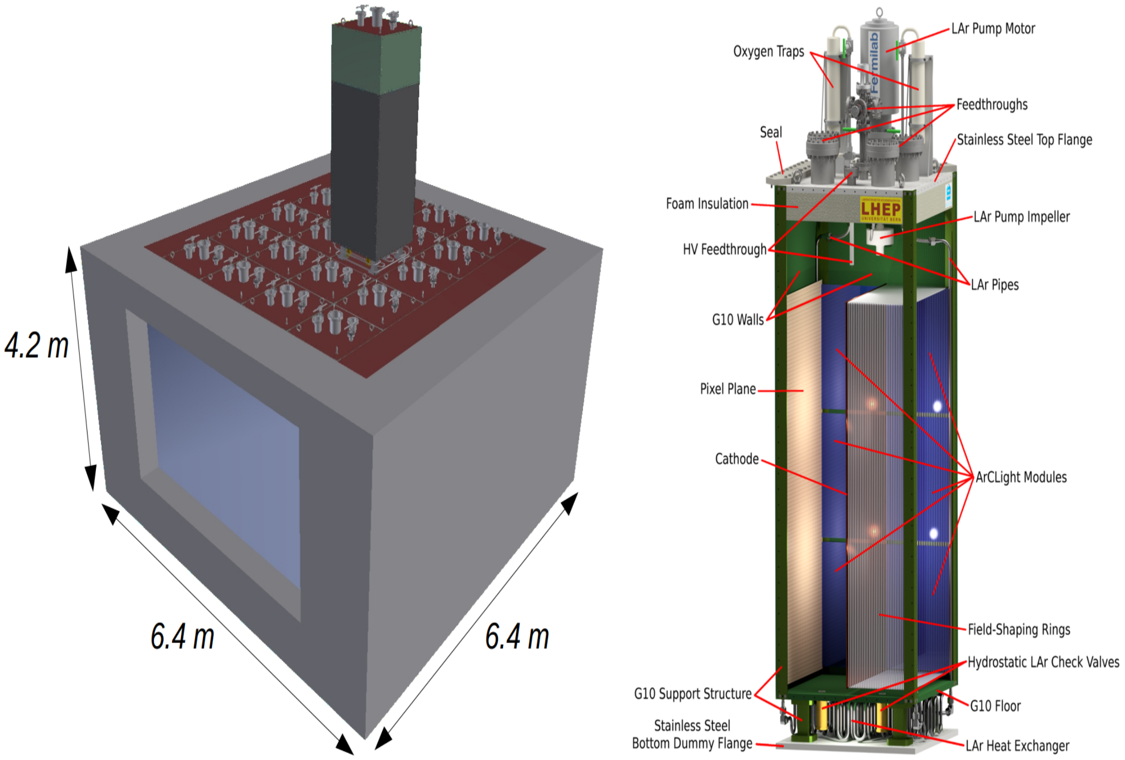

Figure 2.11: Representation of the design of ArgonCube (left) and of one of its module (right)

calorimeter (ECAL) in a 0.5 T magnetic field, provided by a superconductive magnet. The MPD has two main tasks: first to determine the momentum of high energy muons exiting the ArgonCube detector through the measurement of its deflection in the magnetic field. The curvature will also allow to distinguish neutrino from antineutrino interactions and so to measure the wrong-sign component of the beams. This task is fundamental since the Far Detector is not equipped with a magnetic field. The second important role of the MPD is to provide an independent sample of neutrino interactions on Ar; the low momentum threshold allows to constrain one of the least-well understood uncertainties impacting the oscillation analysis, that are the nuclear effects in neutrino-Argon interactions.

The SAND detector will be described in detail in Chapter 3.

2.3 DUNE's scientific programme

The DUNE scientific goals are grouped into a **primary scientific program** and an **ancillary scientific program** [38].

The primary scientific program aims to answer to some open questions in neutrino and astroparticle physics:

- Discovery of the possible CP symmetry violation in the leptonic sector which could provide a possible explanation of matter-antimatter asymmetry in the Universe;
- Determination of the neutrino mass ordering;
- Precision tests of the three-flavour neutrino oscillation model;
- Search for proton decay in several important decay modes. The discovery of such a decay will represent a confirmation of the GUT theories;
- Detection and measurement of the ν_e flux of a core-collapse supernova, should any occur during the lifetime of the DUNE experiment, that could shed light on the nature of this astrophysical event, as well as on the nature of neutrino themselves.

The ancillary scientific program consists of a series of physic goals that DUNE can reach for the stringent characteristics that the neutrino beam, the Far Detector and the Near Detector will have even if there aren't the main objective for which this experiment has been designed. In this category we can find:

- accelerator-based neutrino flavour transition measurements related to Beyond Standard Model physics;
- measurements of neutrino oscillation phenomenon using atmospheric neutrinos;

- a rich program related to neutrino interaction physics such as measurements of neutrino cross-sections, studies of nuclear effects and measurements of the structure of nucleons.

2.3.1 Sensitivities and systematics

The ν_μ energy spectrum measured at Near Detector is extrapolated to the Far Detector and used to predict both the ν_μ and ν_e expected spectrum $N_{FD}^{\text{expected}}(\nu_\mu)$ and $N_{FD}^{\text{expected}}(\nu_e)$ [45]. The observed spectrum of neutrino events is the product of beam flux (Φ), detector efficiency (ε) and neutrino interaction cross section (σ).

$$N_{ND}^{\text{data}}\left(\nu_\mu\right) = \Phi_{ND}\left(\nu_\mu\right) \otimes \varepsilon_{ND}\left(\nu_\mu\right) \otimes \sigma_{ND}\left(\nu_\mu\right) \tag{2.1}$$

Some corrections have to been done in order to extrapolate the spectra observed in the Near Detector to the Far Detector:

- Differences in the beam flux in the Near and Far Detectors, Φ_{FD}/Φ_{ND}. The Near Detector is much closer to the neutrino beamline and so, differently from the Far Detector, it sees an extended neutrino source. A simulated Monte Carlo simulation is used in order to correct these differences. Uncertainties arise from inaccuracies in the simulation of the hadron production from the proton-target interactions, the focusing of the horns, the material in the beamline and the decay channel geometry.

- Differences in the Near and Far Detector efficiencies, $\varepsilon_{FD}/\varepsilon_{ND}$. The uncertainties arise from the different event selection efficiencies and the imperfect modeling of the energy scales of the Near and Far Detectors. Having identical detectors allow for ν_μ signal prediction to cancel the uncertainties in the extrapolation. For the ν_e signal prediction there are residual uncertainties arising from the different criteria used to select ν_e and ν_μ candidate events and different detector response functions.

- Differences in the interactions of neutrinos in the Near and Far Detector, σ_{FD}/σ_{ND}. For the extrapolation of the ν_μ expected signal these differences are canceled if the Far and Near Detectors have the same target nucleus. When the ν_μ signal in the Near Detector is used to predict the ν_e (ν_τ) signals in the Far Detector, the uncertainties arising from differences in ν_e (ν_τ) interactions dominate $\sigma_{FD}(\nu_e)/\sigma_{ND}(\nu_\mu)$.

The expected signals in the Far Detector can be summarized:

$$N_{FD}^{\text{data}}(\nu_\mu) = N_{ND}^{\text{data}}(\nu_\mu) \otimes \frac{\Phi_{FD}(\nu_\mu)}{\Phi_{ND}(\nu_\mu)} \otimes P(\nu_\mu \to \nu_\mu) \otimes \frac{\varepsilon_{FD}(\nu_\mu)}{\varepsilon_{ND}(\nu_\mu)} \otimes \frac{\sigma_{FD}(\nu_\mu)}{\sigma_{ND}(\nu_\mu)} \tag{2.2}$$

$$\begin{aligned}
N_{FD}^{\text{data}}(\nu_e) = & \underbrace{N_{ND}^{\text{data}}(\nu_\mu) \otimes \frac{\Phi_{FD}(\nu_\mu)}{\Phi_{ND}(\nu_\mu)} \otimes P(\nu_\mu \to \nu_e) \otimes \frac{\varepsilon_{FD}(\nu_e)}{\varepsilon_{ND}(\nu_\mu)} \otimes \frac{\sigma_{FD}(\nu_e)}{\sigma_{ND}(\nu_\mu)}}_{\text{expected signal events}} \\
& + \underbrace{N_{ND}^{\text{data}}(\nu_e) \otimes \frac{\Phi_{FD}(\nu_e)}{\Phi_{ND}(\nu_e)} \otimes P(\nu_e \to \nu_e) \otimes \frac{\varepsilon_{FD}(\nu_e)}{\varepsilon_{ND}(\nu_e)} \otimes \frac{\sigma_{FD}(\nu_e)}{\sigma_{ND}(\nu_e)}}_{\text{beam } \nu_e \text{ events}} \qquad (2.3) \\
& + \text{NC background extrapolated from } N_{ND}^{\text{data}}(\nu_e) \\
& + \nu_\tau \text{ background extrapolated from } N_{ND}^{\text{data}}(\nu_\mu)
\end{aligned}$$

The main sources of uncertainties are estimated from the current performance of similar experiments, i.e. MINOS and T2K, and they are:

- Beam flux uncertainties: these are related to the precision with which the Near Detector will measure the absolute normalization and shape of the different components of the neutrino beam. The DUNE Near Detector is being designed to significantly improve performance relative to the current generation of high-intensity flux neutrino detectors.

- ν_μ energy-scale uncertainty: the ν_μ event spectrum in the Near Detector is used to predict the ν_e appearance signal at the Far Detector so the ν_μ energy-scale uncertainty is propagated as an uncertainty on the ν_e appearance signal.

- Absolute ν_e energy-scale uncertainties: an accurate measurement of the ν_e appearance signal shape is necessary to obtain the desired MO and CP-violation sensitivity. The measurement of the absolute ν_e energy-scale depends on the detector response and it is expected to be an important systematic uncertainty in the DUNE oscillation analysis.

- Simulation uncertainties: these type of uncertainties refer primarily to uncertainties in neutrino interaction with the target nucleus in the Near and Far Detectors.

In the Fig. 2.12 a flow diagram of the analysis chain is shown while in Fig. 2.13 a summary table of the main source of uncertainties of the DUNE experiment compared to that of other experiments is represented.

2.3.2 Neutrino mass ordering and CP violation

The DUNE experiment will determine the neutrino mass ordering and CP violation measuring $\nu_\mu \to \nu_e$ and $\overline{\nu}_\mu \to \overline{\nu}_e$ oscillation probability [38] [45]. At the first order, the

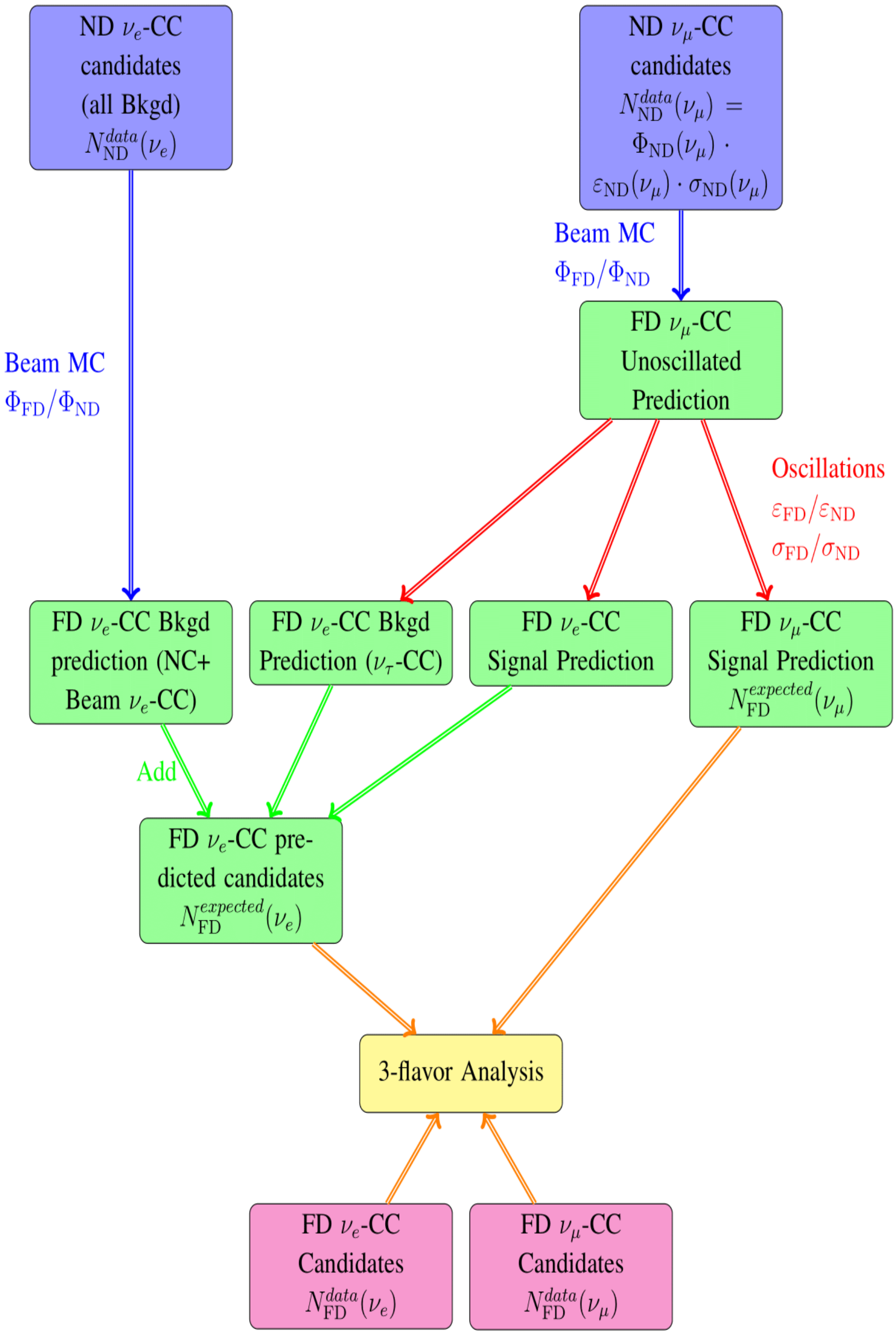

Figure 2.12: Flow diagram of the ν_e appearance analysis method in a two-detector Long-Baseline experiment.

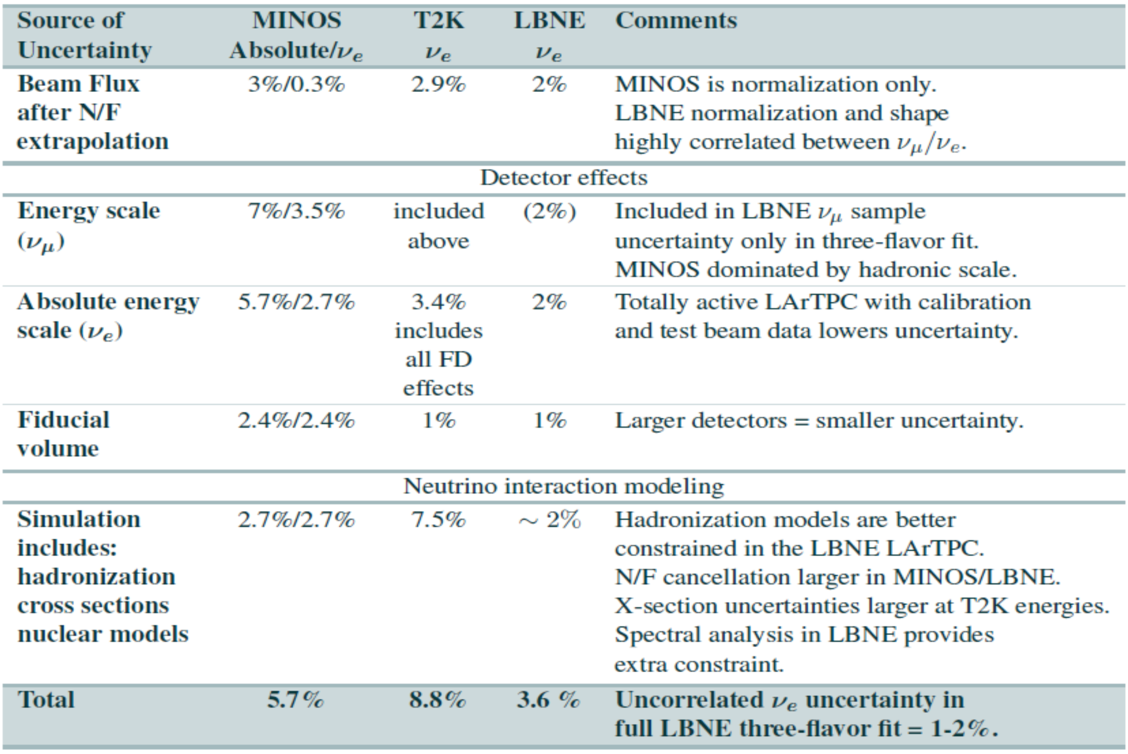

Source of Uncertainty	**MINOS Absolute/ν_e**	**T2K ν_e**	**LBNE ν_e**	**Comments**
Beam Flux after N/F extrapolation	3%/0.3%	2.9%	2%	MINOS is normalization only. LBNE normalization and shape highly correlated between ν_μ/ν_e.
Detector effects				
Energy scale (ν_μ)	7%/3.5%	included above	(2%)	Included in LBNE ν_μ sample uncertainty only in three-flavor fit. MINOS dominated by hadronic scale.
Absolute energy scale (ν_e)	5.7%/2.7%	3.4% includes all FD effects	2%	Totally active LArTPC with calibration and test beam data lowers uncertainty.
Fiducial volume	2.4%/2.4%	1%	1%	Larger detectors = smaller uncertainty.
Neutrino interaction modeling				
Simulation includes: hadronization cross sections nuclear models	2.7%/2.7%	7.5%	$\sim$ 2%	Hadronization models are better constrained in the LBNE LArTPC. N/F cancellation larger in MINOS/LBNE. X-section uncertainties larger at T2K energies. Spectral analysis in LBNE provides extra constraint.
Total	**5.7%**	**8.8%**	**3.6 %**	**Uncorrelated ν_e uncertainty in full LBNE three-flavor fit = 1-2%.**

Figure 2.13: Main systematics in the ν_e appearance channel for T2K and MINOS experiments and the ones expected in the LBNE experiment, the pprevious name used for DUNE.

$\nu_\mu \to \nu_e$ oscillation probability, assuming a constant matter density, is

$$\begin{aligned} P(\nu_\mu \to \nu_e) \simeq & \sin^2\theta_{23}\sin^2 2\theta_{13}\frac{\sin^2(\Delta_{31}-AL)}{(\Delta_{31}-AL)^2}\Delta_{31}^2 \\ & + \sin 2\theta_{23}\sin 2\theta_{13}\sin 2\theta_{12}\frac{\sin^2(\Delta_{31}-AL)}{(\Delta_{31}-AL)}\Delta_{31}\frac{\sin(AL)}{AL}\Delta_{21}\cos(\Delta_{31}+\delta_{CP}) \\ & + \cos^2\theta_{23}\sin^2 2\theta_{12}\frac{\sin^2(AL)}{(AL)^2}\Delta_{21}^2 \end{aligned} \tag{2.4}$$

where $\Delta_{ij} = \Delta m_{ij}^2 L/4E_\nu$, $A = G_F N_e/\sqrt{2}$, G_F is the Fermi constant, N_e is the electron density in the medium, L is the baseline length and E_ν the neutrino energy. Since δ_{CP} and A change sign for antineutrino oscillations both the CP violation and the matter effect introduce an asymmetry. In the DUNE experiment the measured value of this asymmetry

$$\mathcal{A} = \frac{P(\nu_\alpha \to \nu_\beta) - P(\overline{\nu}_\alpha \to \overline{\nu}_\beta)}{P(\nu_\alpha \to \nu_\beta) + P(\overline{\nu}_\alpha \to \overline{\nu}_\beta)} \tag{2.5}$$

will be used to determine both CP violation and MO. The value A have the contribution of both a CP violation induced asymmetry term ($\mathcal{A}_{\text{CP}}$) and of a matter induced asymmetry term ($\mathcal{A}_{\text{matter}}$) so that

$$\mathcal{A} = \mathcal{A}_{\text{CP}} + \mathcal{A}_{\text{matter}}. \tag{2.6}$$

We also know that when neutrinos travel through matter there are opposite effects on the oscillation probabilities depending on what is the order of neutrino mass eigenstates: in the NO (IO) the $P(\nu_\mu \to \nu_e)$ is enhanced (suppressed) and the $P(\overline{\nu}_\mu \to \overline{\nu}_e)$ is suppressed (enhanced). So $\mathcal{A}_{\text{matter}}$ is affected by MO. The DUNE experiment must be capable to disentangle the two $\mathcal{A}_{\text{CP}}$ and $\mathcal{A}_{\text{matter}}$ terms, since it aims to determine the presence of both CP violation in the leptonic sector and the MO measuring the value of $\mathcal{A}$. In Fig. 2.14 the asymmetries due to matter effects (matter asymmetry) and to a maximal CP violation ($\delta_{CP} \pm \pi/2$) as a function of the energy and of the baseline length are shown. In order to understand how the two types of asymmetries can be distinguished, it is useful to approximate their dependencies from the baseline length and neutrinos energy near the peaks of oscillation probability as:

$$\mathcal{A}_\delta \propto L/E \tag{2.7}$$

$$\mathcal{A}_{\text{matter}} \propto L \times E \tag{2.8}$$

So, given the same oscillation probability peak (i.e. the same L/E ratio), for increasing baseline the CP-induced asymmetry remains the same while the matter induced one enhances. In Fig. 2.15 the total neutrino-antineutrino asymmetry $\mathcal{A}$ at the first (black) and second (red) oscillation peak, as a function of δ_{CP} for four different values of L are shown. Depending on the neutrino mass ordering the relative size of the asymmetries varies. With a baseline longer than 1300 Km the matter asymmetry $\mathcal{A}_{\text{matter}}$,at the first oscillation peak, will be 40% much larger respect to the CP asymmetry $\mathcal{A}_{\text{CP}}$ making possible to unambiguously disentangle the two contributions.

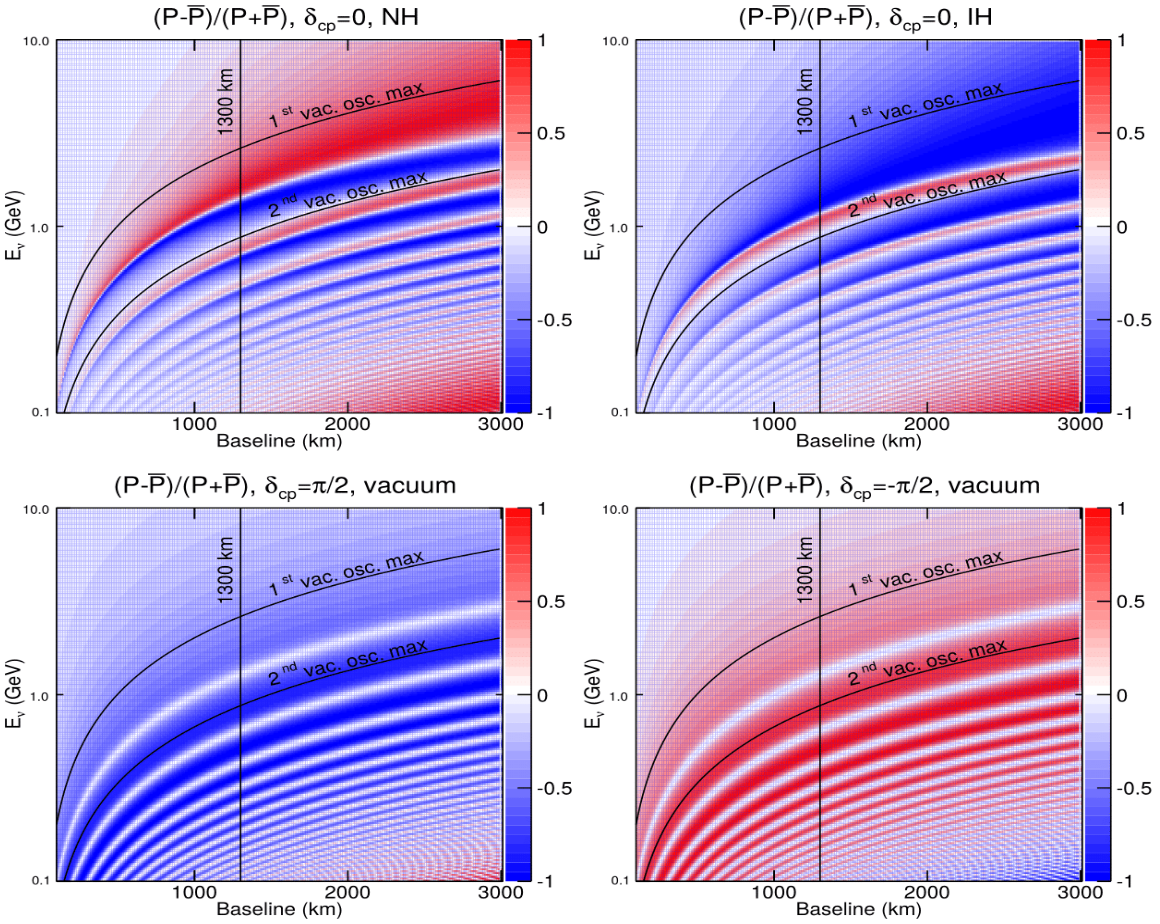

Figure 2.14: The asymmetries in the oscillation probability as a function of the baseline length and of the neutrino energy. The upper plots show only the asymmetry due to the matter effects for normal (left) and inverted (right) mass ordering. The two lower plots show the asymmetry due to δ_{CP} in the vacuum for $\delta_{CP} = +\pi/2$ (left) and $\delta_{CP} = -\pi/2$ (right).

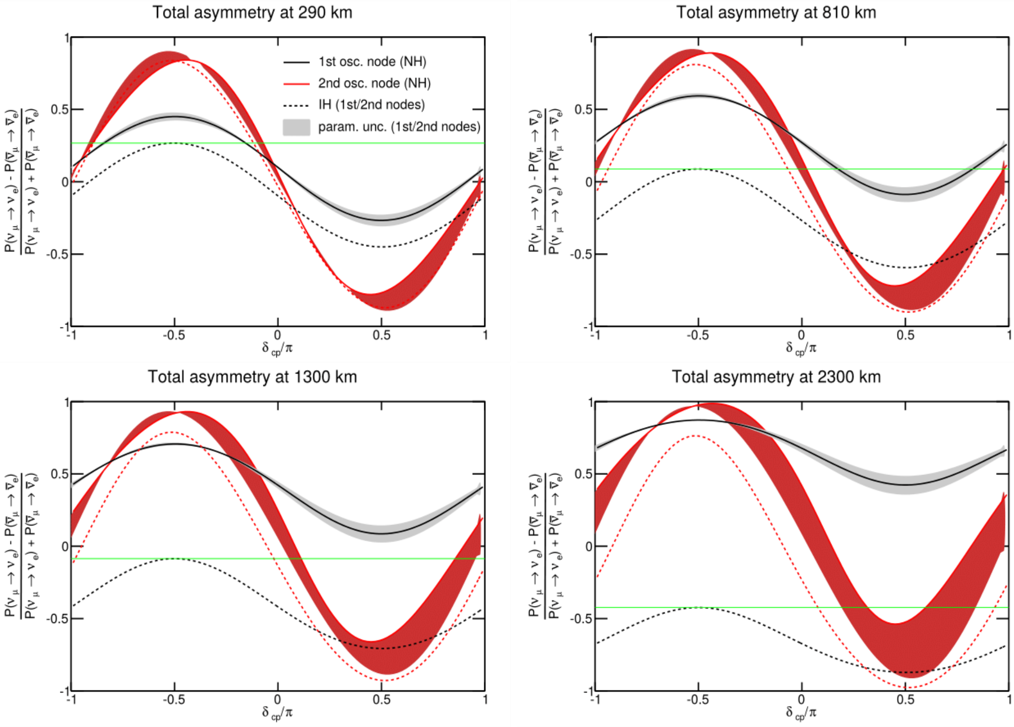

Figure 2.15: $\nu/\overline{\nu}$ asymmetries for the first two probability oscillation nodes as a function of δ_{CP} for different values of the baseline length (290, 810, 1300 and 2300 km). The dashed (full) black line is the total asymmetry at first node for normal (inverted) ordering. The red lines indicate the asymmetries at the second node.

Expected significance of the neutrino MO determination and sensitivity on δ_{cp}

In order to evaluate the sensitivity of the DUNE experiment, the compatibility of a particular oscillation hypothesis with the data is evaluated using the likelihood for Poisson-distributed data:

$$\chi^2 = -2\ln\mathcal{L} = \sum_{i}^{N_{\text{bins}}} \left[M_i - D_i + D_i \ln \frac{D_i}{M_i} \right] \tag{2.9}$$

where M_i is the MC expectation in bin i and D_i is the observed value. Most often the bins represent reconstructed neutrino energy but other observables may be used [41]. The impact of systematic uncertainties is included by adding additional nuisance parameters into the fit.

The sensitivity in the neutrino MO and CP violation measurements, in terms of $\Delta\chi^2$, is obtained comparing the expected spectra obtained using the GLoBES software package [46] with the expectation in case of null hypothesis

$$\Delta\chi^2_{\text{ordering}} = \chi^2_{\text{opposite}} - \chi^2_{\text{true}} \tag{2.10}$$

$$\Delta\chi^2_{CPV} = \text{Min}\left[\Delta\chi^2_{CP}\left(\delta_{CP} = 0\right), \left(\delta_{CP} = \pi\right)\right]. \tag{2.11}$$

Since for the case of MO there is no null-hypothesis, the sensitivities are valuated separately for NO and IO. In addition, since the true value of δ_{CP} is unknown, a scan is performed over all possible values. The value of $\Delta\chi^2$ is a measure of how well the alternate hypothesis can be excluded given the expected data and systematic uncertainties.

The DUNE experiment aims determining the neutrino MO with a significance corresponding to $\sqrt{\Delta\chi^2} > 5$ for all possible δ_{CP} values. In Fig. 2.16, the expected significance as a function of the exposure, expressed in kt · MW · yr is shown while in Fig. 2.17 the variation of the significance as a function of δ_{CP} is illustrated. An exposure of 200-400 kt · MW · yr, corresponding to 7 years of data collection taking, will be necessary in order to reach a significance of $\sqrt{\Delta\chi^2} = 5$. In Fig. 2.18 the significance for observing CP violation for 25%, 50% and 75% of the possible values of δ_{CP} as a function of the exposure is shown.

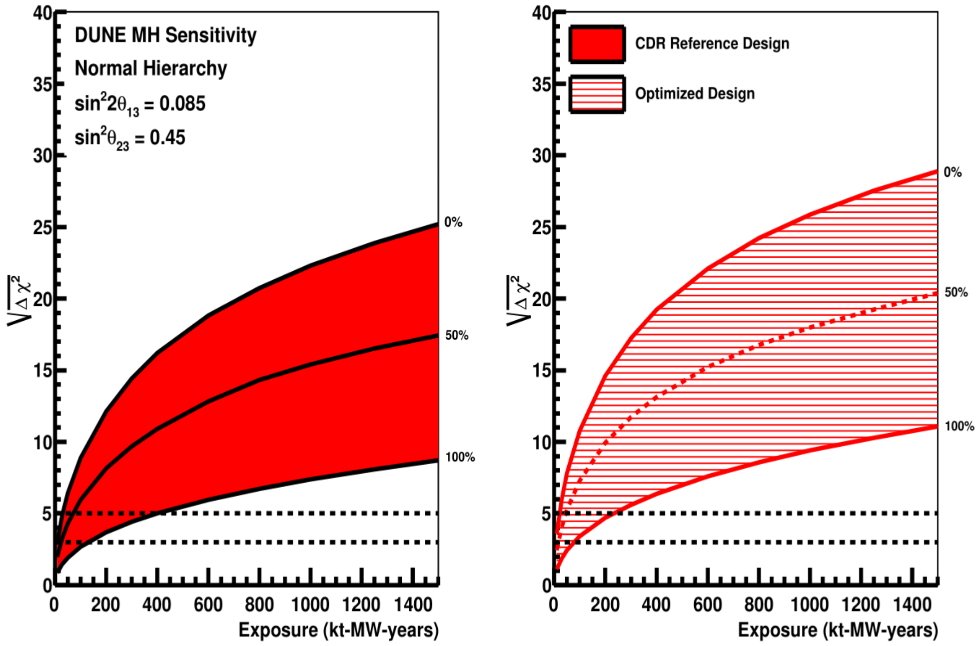

Figure 2.16: The minimum significance for the determination of mass ordering for the 100%, 50%, 0% of the δ_{CP} as a function of exposure. The NO is assumed to be true

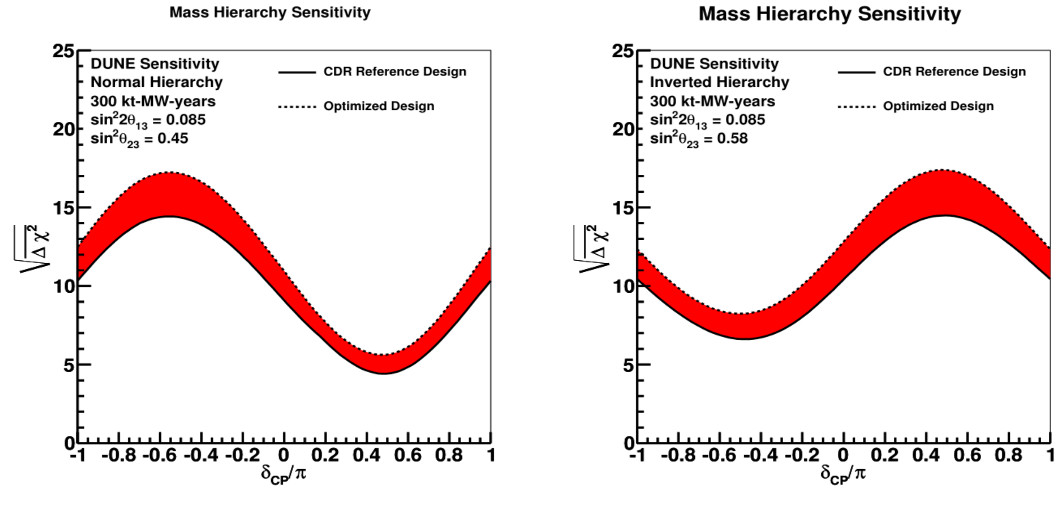

Figure 2.17: MO significance as a function of δ_{CP} for a 300 $Kt \cdot MW \cdot yr$ exposure. The red band is due to different beam designs.

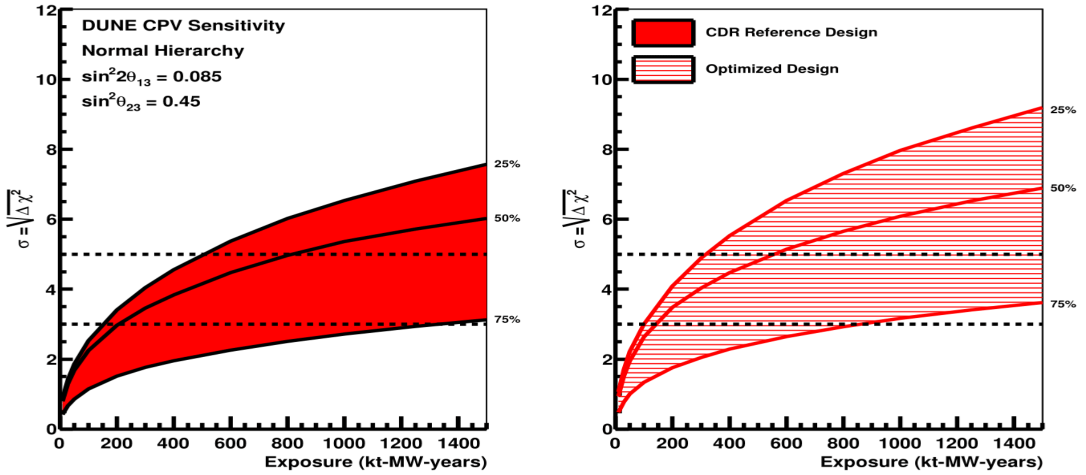

Figure 2.18: The minimum significance to determine the hierarchy mass for the 25%, 50%, 75% of the δ_{CP} values as a function of exposure. The NO is assumed true.

2.3.3 Precision measurements of oscillation parameters

The DUNE experiment will improve the precision on:

- $\sin^2\theta_{23}$ and the octant of θ_{23}
- δ_{CP}
- $\sin^2\theta_{13}$
- Δm^2_{31}.

The precision that the DUNE experiment will reach in the measurements of these parameters as a function of the exposure is shown in Fig. 2.19.

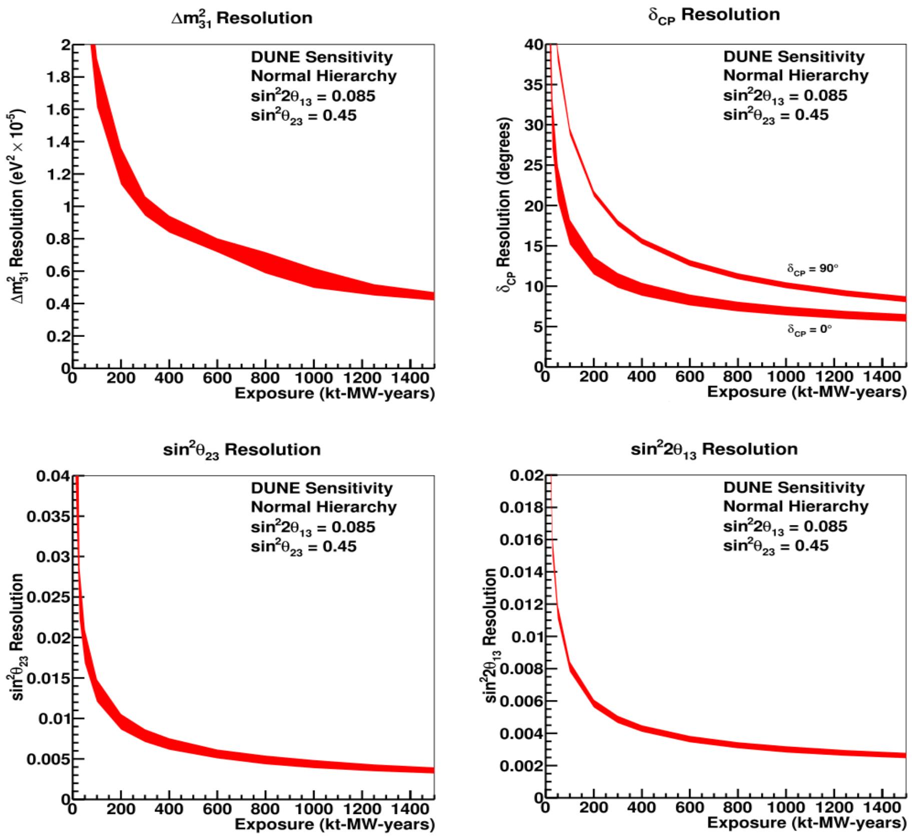

Figure 2.19: Resolution of the Δm^2_{31} (upper left), δ_{CP} (upper right), $\sin^2\theta_{23}$ (lower left) and $\sin^2 2\theta_{13}$ (lower right) measurements as a function of the exposure. The red area is due to sensitivity dependence on different beam designs.

The measurement of $\sin^2\theta_{23}$ will be particularly interesting because DUNE could finally resolve the so-called octant ambiguity. According to the measurements performed in past experiments, θ_{23} could be either $> 45°$ and $< 45°$. A value of this mixing angle of 45° indicates that the ν_μ and the ν_τ have the same contribute from the ν_3 mass eigenstate and could be a hint of a new symmetry. The octant of θ_{23} will be determined combining the oscillation measurements of $\nu_\mu \to \nu_e$ that depends on $\sin^2 2\theta_{23}$ and of $\nu_\mu \to \nu_\mu$ that is sensitive to $\sin^2\theta_{23}$. $\Delta\chi^2$ for the determination of the right octant is defined as

$$\Delta\chi^2_{\text{octant}} = |\chi^2_{\theta_{23}^{test}>45°} - \chi^2_{\theta_{23}^{test}<45°}|. \tag{2.12}$$

The significance in the determination of the octant as a function of the true value of θ_{23} is showed in Fig. 2.20.

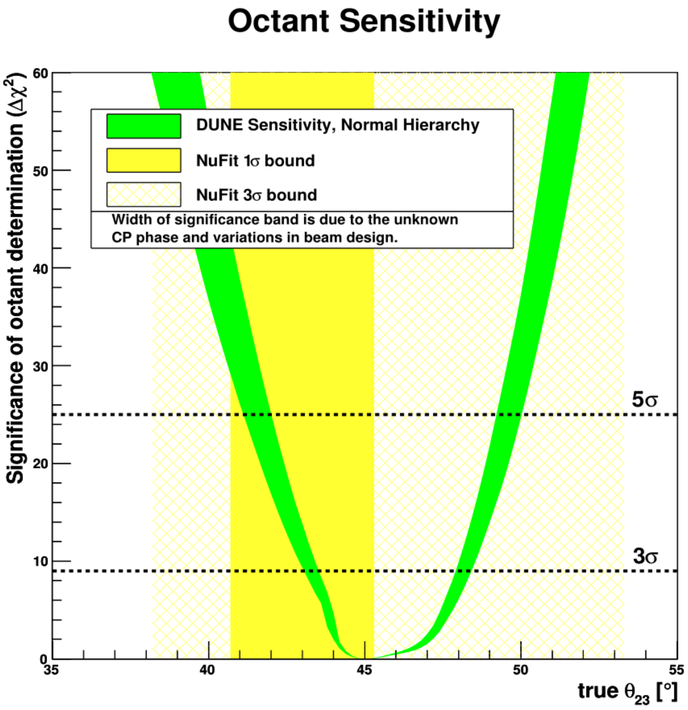

Figure 2.20: The significance at which DUNE will determine the θ_{23} octant. The green area represents the sensitivity range due to beam variations and to the true value of δ_{CP}. The yellow areas are the 1σ and 2σ allowed regions obtained from a global fit.

2.3.4 Proton decay measurements

Grand Unified Theories (GUTs) predicts proton decay. To observe such a rare event a kt-scale detector placed deep underground to limit backgrounds is needed. The strength

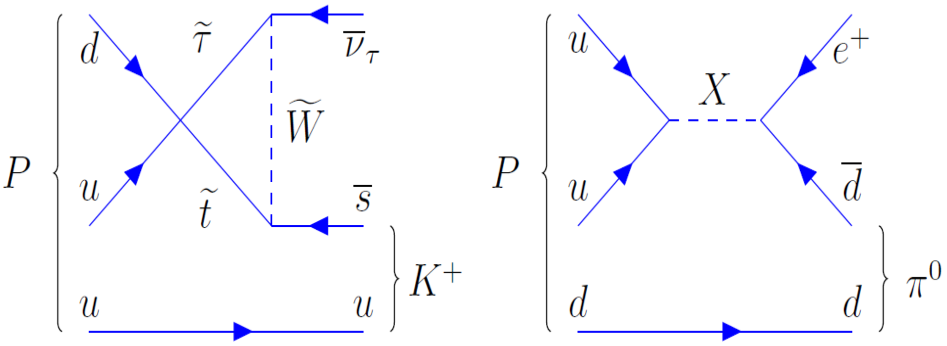

Figure 2.21: Feynman diagrams for proton decay modes from supersymmetric GUT , $p^+ \to K^+\overline{\nu}$ (left) and gauge-mediation GUT models, $p^+ \to e^+\pi^0$

of DUNE will consist on the capability to detect two dominant proton decay modes that are shown in Fig. 2.21.

The decay $p^+ \to e^+\pi^0$ is predicted to have an higher branching fraction. Nevertheless this channel is better detectable by water Cherenkov experiments because the mass of the proton is converted into the electromagnetic shower energy of the positron and the photons from the π^0 decay.

The other mode $p^+ \to K^+\overline{\nu}$ is extremely interesting for DUNE, since stopping kaons have a high ionization density and a LArTPC could identify the K^+ track with high efficiency.

2.3.5 Supernova neutrino measurements

The DUNE experiment will be sensitive to neutrino with energy above few MeV and so it will be very suitable in the detection of burst of neutrinos coming from a core-collapse supernova. The studies of supernovae neutrinos will permit a better comprehension of this astrophysical phenomenon but also additional constraints on physics beyond the Standard Model as well as independent measurements on neutrino flavour oscillation. In particular the physics of the oscillations in supernova environment promises to be much richer than in any case studied to date in solar neutrinos and terrestrial sources for a variety of reasons. For example:

- The oscillation patterns are very different for the two mass orderings.
- Additional informations on oscillation parameters, free of supernova model-dependence, will be available if matter effects can be observed by other detectors around the world.

- The neutrino and antineutrino oscillations from a core-collapse supernova manifest very differently; in neutrino channel the oscillation features are in general more pronounced and so it could be very interesting to detect both neutrino and antineutrino channels with high statistics.

Currently, the other experiments that would detect the neutrinos from a core-collapse supernova are sensitive primarily to $\bar{\nu}_\mu$s. On the other hand, the DUNE detector will be very sensitive to the ν_e component of the flux, via the absorption interaction

$$\nu_e +^{40} Ar \rightarrow e^- +^{40} K^*. \tag{2.13}$$

This interaction can be tagged via the coincidence of the electrons with the gamma product by the de-excitation of the ${}^{40}K^*$. The number of signal events scales with mass and the inverse square of distance, as shown in Fig. 2.22.

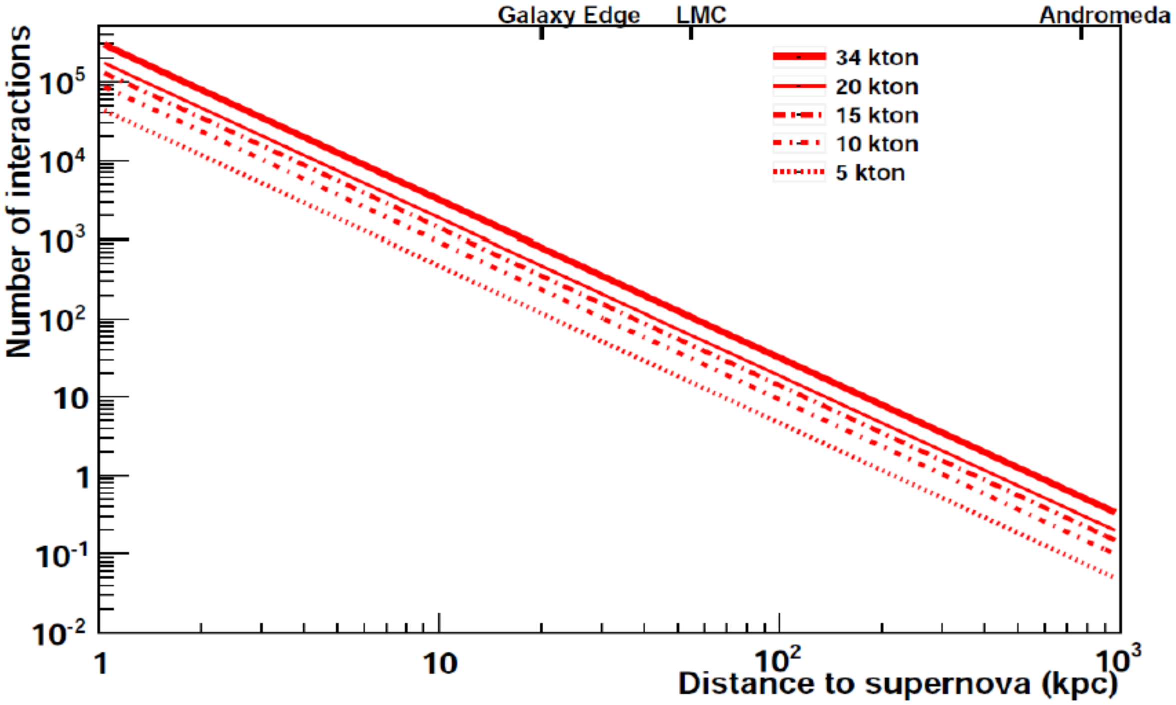

Figure 2.22: Number of core-collapse neutrino events in LAr detetector as a function of distance to the supernova for different detector masses.

2.3.6 Oscillation physics with atmospheric neutrinos

Thanks to its large target mass and to its underground location, DUNE will be able to make oscillation studies using atmospheric neutrinos. This measurements will be complementary to the ones performed with neutrino beams; all mixing parameters can be measured thanks to the wide range of L/E for atmospheric neutrinos. In Fig. 2.23 (right) the MO sensitivity as a function of the exposure time is shown; it is practically independent from δ_{CP} making possible to resolve some ambiguities in the mass ordering measurements made with beam neutrinos.

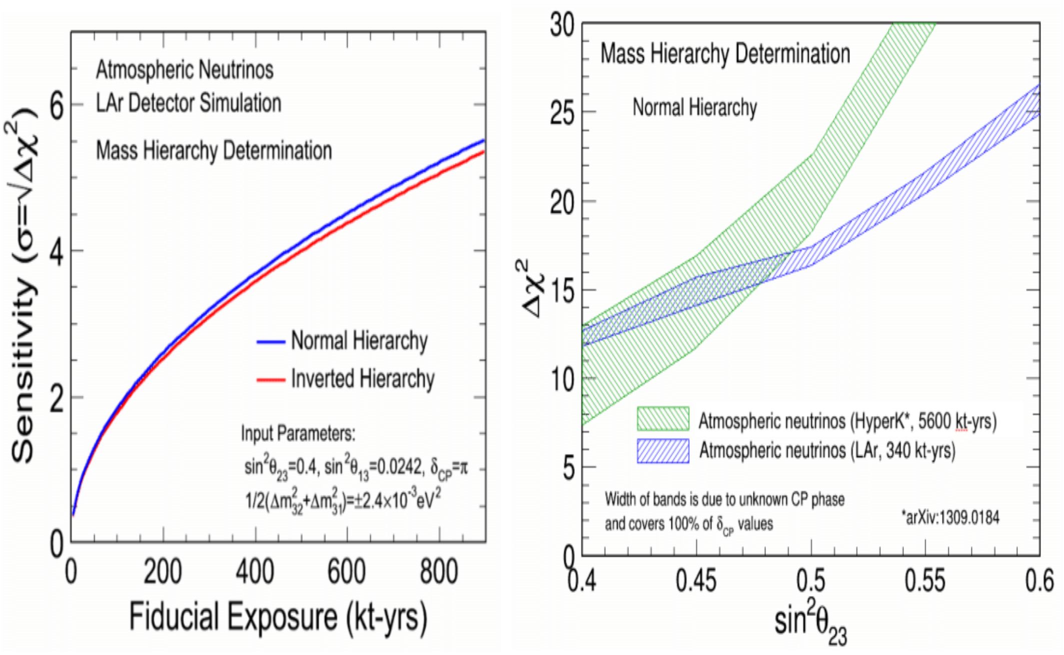

Figure 2.23: MO sensitivity as a function of exposure (left) and of the true value of θ_{23} (right) using atmospheric neutrinos. The sensitivities of the Hyper-Kamiokande experiment sensitivities are also shown for comparison.

2.3.7 Near Detector Physics

The main physics goal of the DUNE Near Detector consists in the constraint of the systematic uncertainties which could lead to degradation of the sensitivity of both CP-violation and mass ordering measurements. It is necessary to characterize the expected unoscillated neutrino beam with high precision by measuring neutrino fluxes, energy spectrum together with cross section in LAr. Exploiting the Near Detector capabilities a possible searches for new physics could be performed, for example it could look for a large Δm^2 oscillations hint of the existence of a light sterile neutrino. Moreover, it will be possible to search for DM particle induced events. The signature of DM is quite similar to the one produced by the neutrino beam, so a possible way to discriminate among them is to use time information since the fact that the DM particles have an higher mass and they travel much slower than neutrinos. In addition, since the electrons struck by DM will be much more forward in direction, the angles of these electrons may be used to reduce backgrounds, taking advantage of the fine angular resolution of the DUNE Near Detector.

Chapter 3

System for on-Axis Neutrino Detection

3.1 Requirements

The expected number of observed events for the process X with reconstructed energy E_{rec} can be written as:

$$N_x(E_{\text{rec}}) = \int_{E_\nu} dE_\nu \Phi(E_\nu) P_{\text{osc}}(E_\nu) \sigma_X(E_\nu) R_{\text{phys}}(E_\nu, E_{\text{vis}}) R_{\text{det}}(E_{\text{rec}}, E_{\text{vis}}) \tag{3.1}$$

where Φ is the incoming neutrino flux, σ_X is the cross-section for the process X, R_{phys} is the physics response introduced by the nuclear smearing that affects the visible final state particles and R_{det} is the detector response function for the visible final state particles [47]. E_ν is the neutrino energy while E_{vis} is the total energy of the visible final state particles. The main terms of the Eq. 3.1 are folded together into the observed event distributions making the decoupling impossible using only one detector or a single nuclear target. For this reason a capable Near Detector complex is mandatory. In particular, since the knowledge of the LBNF neutrino flux is of utmost importance, a precise beam monitor detector is needed. The System for on-Axis for Neutrino Detection (SAND), which composes the DUNE Near Detector system, has as major task the continuous beam monitoring and the precise determination of its energy spectrum.

3.2 The SAND detector

The proposed design of the SAND detector aims to realize a multipurpose detector capable of precision tracking and calorimetry together with the ability to detect neutrino interactions on different target materials, including Hydrogen and Argon. The existing magnet and electromagnetic calorimeter of the K_L^0 LOng Experiment (KLOE) will be reused and complemented with an internal high precision tracker based on the straw

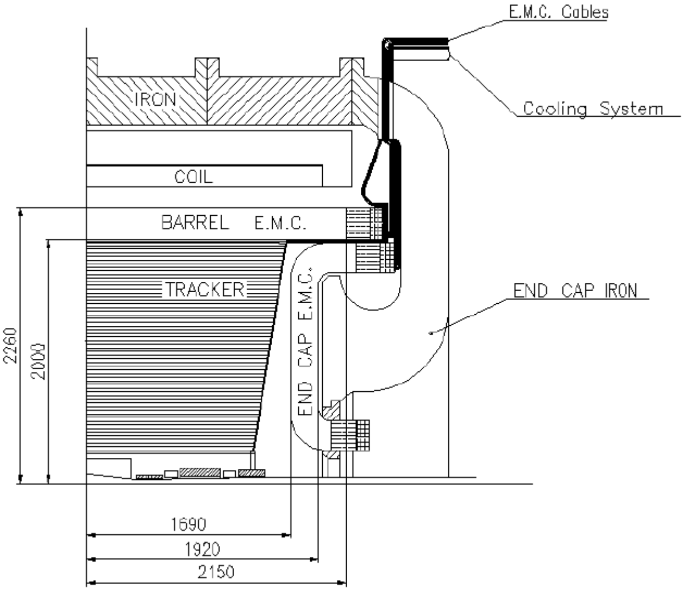

Figure 3.1: Vertical cross section of the KLOE detector. The dimensions are shown in mm.

tube technology. A LAr target could be added for inter-calibration within Near Detector system.

3.2.1 The superconducting magnet

The SAND detector will employ the existing superconducting magnet operated in the KLOE experiment. The magnet is designed together with the iron yoke to produce a magnetic field of 0.6 T over a 4.3 m long and 4.8 m diameter cylindrical volume. The coil is operated at a nominal current of 2902 A and consists of a single conductor layer made of a Nb-Ti composite of Rutherford cable co-extruded with high purity aluminum. The coil support is an aluminum cylinder with cooling channels welded outside. The coil is located in a cryostat whose dimensions are 5.76 m outer diameter, 4.86 m inner diameter and 4.4 m overall length for a total cold mass of ∼8.5 t. The cryostat is inserted inside an iron return yoke whose mass is 475 t. A schematic representation of the KLOE detector is shown in Fig. 3.1.

The cooling of the coil is performed by thermo-siphoning cycles: gas Helium at 5.2 K is injected at 3 bar from the cryogenic plant and melted through Joule-Thomson valves into a liquid Argon tank in thermal contact with the coil. The current leads are directly cooled by liquid Helium and the radiation shields are cooled by gas Helium at 70K.

3.2.2 The electromagnetic calorimeter

The electromagnetic calorimeter (ECAL) is a lead-scintillating fiber sampling calorimeter. The scintillating fibers are chosen because they grant high light transmission over several meters and sub-ns timing accuracy. The overall ECAL is composed by a barrel and two endcaps (see Fig. 3.1).

The nearly-cylindrical barrel consists of 24 modules that are 4.3 m long, 23 cm thick with a trapezoidal cross-section of bases of 52 and 59 cm. Each end-cap consists of 32 vertical modules 23 cm thick with a length that goes from 0.7 m to 3.9 m. Their cross-section is rectangular of variable width. All modules are stacks of about 200 grooved 0.5 mm thick lead alternating with 200 layers of cladded 1 mm diameter scintillating fibers. In order to have a 4π coverage and to place the phototube axis parallel to the magnetic field, the end-cap modules are bent at the upper and lower ends to allow insertion into the barrel calorimeter.

Each module is read on both ends by phototubes through a light guide in order to match the circular photo-cathodes. The read-out divides the calorimeter module in five layers: the first four are 4.4 cm thick while the last one is 5.2 cm thick. Each layer is further subdivided into 4.4 cm wide elements in the transverse direction, except at the edges of the trapezoidal modules. The calorimeter weight is about 100 tons and the read-out system includes 4880 phototubes. The spatial, energy and timing resolution was evaluated in the commissioning and running phases of the KLOE experiment and they amount to:

- $r - \phi$ or $x - z$ resolution of 1.3 cm $\left(\frac{4.4}{\sqrt{12}}\text{ cm}\right)$;
- energy resolution $\frac{\sigma}{E} = \frac{5\%}{\sqrt{E(GeV)}}$;
- time resolution $\frac{54}{\sqrt{E(GeV)}}$ ps.

The layout of the calorimeter inside the KLOE magnet is represented in Fig 3.2

3.2.3 Inner tracker

The primary goals of the inner tracker are two: offer a target for neutrino interactions and provide a tracking system capable to reconstruct the momenta of the charged particles produced in the interactions. The inner tracker is designed in order to fulfill the Near Detector physics requirements:

- low density and high track sampling to guarantee high momentum, angular and space resolution;
- total thickness comparable with the radiation length to minimize the probability an electron produces a shower before its momentum was measured;

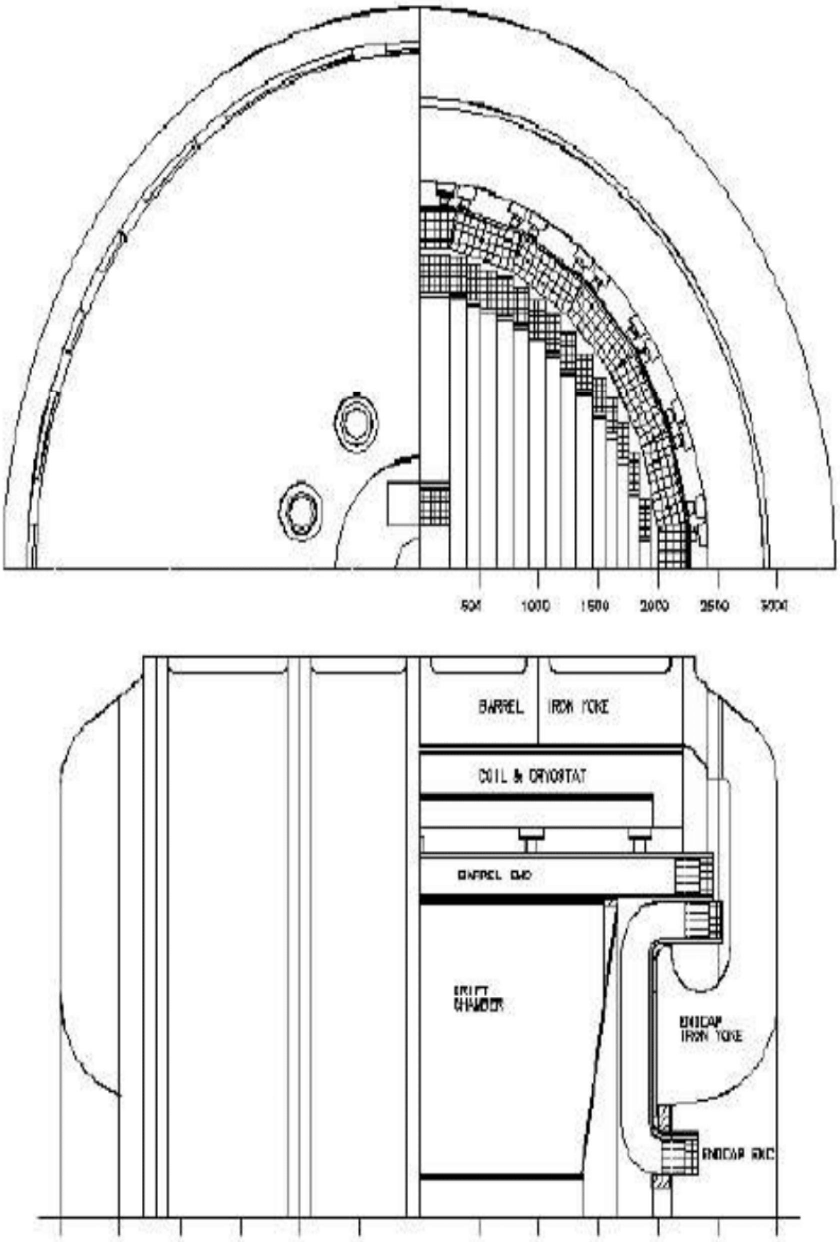

Figure 3.2: Front (top) and side (bottom) view of the calorimeters. Units are in mm.

- different target material;
- particle identification capability for $e^{\pm}$, $\pi^{\pm}$, $K^{\pm}$, p and $\mu^{\pm}$;
- total target of $\simeq 5$ tons.

The neutrino target are thought to be separate from the tracking system in order to reach these requirements. The target mass is spread out uniformly over the entire tracking volume keeping the overall average density low enough to have a detector transparent to the final state particles produced in neutrino interactions.

Straw Tube Tracker

One option for the inner tracker is the Straw Tube Tracker (STT). The STT will be inserted in the magnetic volume and its tracking technology is based on low mass straw tubes. The tracker will be composed by a sequence of compact modules: CH_2- and C-modules. The main elements of a CH_2-module, 44.09 mm thick, are:

- A solid polypropylene (CH_2) target slab 5.3 mm thick.
- A radiator of 150 CH_2 polypropylene foils, 15 μm thick, interposed by 120 μm air gaps. The configuration of the radiator is optimized in order to guarantee a correct electron identification.
- 4 straw tube layers, XXYY, glued together with a straw diameter of 5 mm, mylar walls with total thickness of 20 μm and 70 nm Aluminium coating, Tungsten wire with 20 μm diameter and 20 nm Gold coating.

The tubes will be filled with a gas mixture of Xe/CO_2 70/30 with an internal pressure of 1.9 atm. A representation of a standard module is shown in Fig. 3.3.

One of the most important feature of the STT modules is the possibility to remove the radiator and to substitute the CH_2 slab with a different nuclear target; in particular the pure graphite (C-module). The usage of this nuclear target is essential because it will provide measurements relevant to achieve a model-independent subtraction of the C background in the selection of pure ν-H interactions. The graphite target is provided by a 4 mm slab mounted upstream of the 4 XXYY straw tube layers. A representation of this kind of module is shown in Fig. 3.4. The thickness is chosen in order to match the same thickness in term of X_0 as the CH_2 radiator. The default gas mixture used for these modules is Ar/CO_2 70/30 with an internal pressure of 1.9 atm. The C-modules will be interleaved throughout the CH_2 ones to guarantee the same acceptance for the two different nuclear targets.

The baseline STT configuration is still under studies. The one considered in this work of thesis consists of:

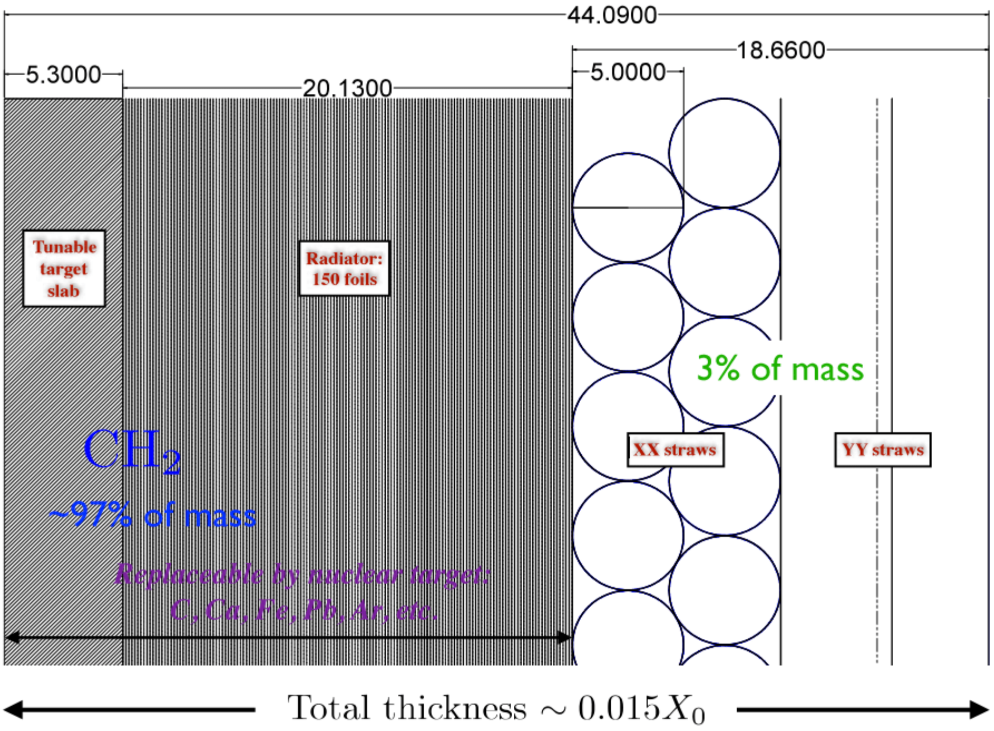

Figure 3.3: Representation of a default compact STT module including three main elements (from left to right): (a) a tunable polypropylene target; (b) a radiator with 150 polypropylene foils for $e^{\pm}$ ID; (c) four straw layers XXYY. The radiator and plastic target are removed for modules to be equipped with nuclear targets. Units are in mm.

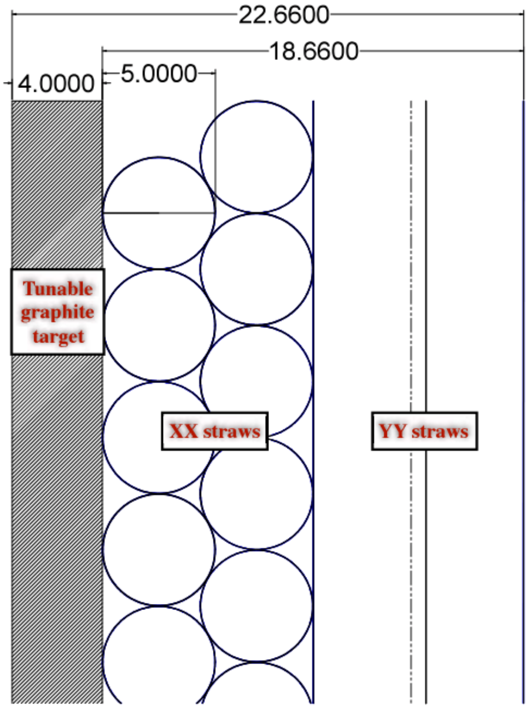

Figure 3.4: Representation of one STT module equipped with graphite target. Units are in mm.

- 1 tracking module with 8 straw layers XXYY+XXYY following the internal LAr meniscus target (see Section 3.2.3);
- 3 standard CH_2-modules seen before;
- 6 blocks each composed of one C-module followed by 12 standard CH_2 ones;
- 1 C-module;
- 3 standard CH_2-modules;
- 5 CH_2-modules but with only the radiators and without the slab.

This detector configuration, shown in Fig. 4.7, is suitable to fulfill the requirement needed to reach detector the physics goals set for SAND. The total number of straws in the entire STT is 231834. The fiducial volume is defined as the region at distance of 20 cm from the edges of the inner walls of the calorimeter and includes a total of 78 STT modules with radiators and CH_2 targets interleaved with 7 STT modules with graphite targets. This geometry corresponds to a fiducial mass of about 4.7 tons, out of which about 680 kg of H and 504 kg of graphite. The STT has an overall average density $\rho \simeq 0.18$ g$/cm^3$, a total radiation length of $\simeq 2.8\ X_0$ and tracking sampling of 0.15(0.36) % $X_0 \parallel (\perp)$. It provides very good space ($< 200\ \mu$m), momentum ($\simeq 3.5\%$), angular ($\simeq 2$ mrad) and timing ($\simeq 1$ ns) resolutions. In addition it is capable to perform an excellent particle identification by exploiting both the energy loss rate dE/dx and the transition radiation for the electron identification.

Another interesting nuclear target material that can possibly used is Ca. The Ca target has the same atomic weight as Ar but is isoscalar, allowing a complete characterization of the A = 40 nucleus, as well as various measurements related to isospin physics. Many other materials such as Pb and Fe could be implemented, according to the studies to be performed.

Liquid Argon target

In order to understand the nuclear effects affecting the neutrino interactions, a LAr target in SAND is mandatory. A LAr target should be small enough to reduce energy loss, showering and multiple scattering. The size and the exact position of this meniscus are still under study. In the configuration being tested the Argon target is approximated by a meniscus with a thickness of 20 cm placed in the upstream part of the tracking region. The LAr meniscus and its position is shown in Fig. 4.3.

3.3 Physics program

3.3.1 Reducing the systematic uncertainties for the neutrino oscillation studies

In order to constrain the systematic uncertainties relevant for the neutrino oscillation analysis all the quantities in the Eq. 3.1 have to be unfolded and measured independently.

- $\Phi(E_\nu)$: the flux is the only factor that can be easily factored out. The flux measurements benefit from detectors with low density trackers, to achieve high resolution and precise scales of the neutrino energy measurement, and from light targets, to minimize the impact of nuclear effects. The STT has these characteristics thanks to the low mass of the STT planes and to the availability of a Hydrogen target. For these reasons SAND will be capable to measure the fluxes for all (anti)neutrino flavours with high accuracy.

- $R_{phys}(E_{vis}, E_{rec})$: in order to disentangle the physics response function from R_{det} it is necessary to have both Ar and lighter targets in the same detector. SAND can constraint the physics response function thanks to the presence of Hydrogen target in the STT, for which $R_{phys} = 1$, and of the LAr target.

- $\sigma_X(E_\nu)$: the cross-section measurements require to have in the Near Detector the same target of the Far Detector, the LAr. Once the fluxes are measured by SAND, it is possible to use the large statistics from the LArTPC and the HPgTPC in the Near Detector (Section 2.2.3) to measure the cross-section on Argon. The cross-section measurements need the knowledge of R_{phys} and R_{det}.

- $R_{det}(E_{vis}, E_{rec})$: since they share the same technology, the response function for the Far Detector LArTPCs can be provided by the Near Detector LArTPC. Anyway the convolution $\sigma_X R_{phys}$ that could be determined by SAND from a comparison of Ar and Hydrogen allows an alternative way to find out R_{det} in LAr.

A precise determination of the fluxes is very important not only for the Far Detector oscillation analysis but also for the Near Detector measurements, because they are crucial in the unfolding of the terms in the Eq. 3.1. SAND will provide a complete determination of absolute ν_μ, $\overline{\nu}_\mu$ and relative $\overline{\nu}_\mu$, ν_μ, ν_e, $\overline{\nu}_e$ fluxes using different processes on different targets. The most important fluxes measurements are the one made on interactions on Hydrogen.

Once the fluxes are measured by SAND the remaining three convoluted terms σ_X R_{phys} R_{det} must be unfolded. The unfolding of the $\sigma_X R_{phys}$ term requires the presence of both Ar target and lighter ones integrated in the same detector because R_{det} is the same. An important role in the unfolding of these two quantities is represented by the Hydrogen target in the SAND STT because it has R_{phys}=1. Once that the cross-sections

σ_X on Hydrogen is measured thanks to the large statistics, the unfolding of neutrino energy E_ν depends only on the R_{det}, which is defined by $\delta p/p$. Comparing that to Ar interactions in the STT it is possible to find out the quantity $\sigma_X R_{phys}$.

To constrain R_{phys} separately from σ_X in STT it is possible to define a set of kinematic variables sensitive to nuclear smearing effects. In fact using CC interaction samples one can compare the distributions of these kinematic variables from events in Ar and H targets. This strategy allows to determine the nuclear smearing for the Near Detector beam spectrum. The use of a complete set of kinematic variables is essential so in order to resolve potential degeneracies.

The determination of $\sigma_X R_{phys}$ for Ar in the STT and the constraints of R_{phys} made by SAND can be compared with the the large number of neutrino interactions collected in the Near Detector LArTPC. This comparison permits to unfold the detector response R_{det} in LAr and to validate the predictions for the Far Detector.

3.3.2 Precise measurements and searches for new physics

Electroweak precise measurements

Exploiting the SAND capabilities, it will be possible to determine precisely the weak mixing angle $\sin^2\theta_W$ in (anti)neutrino deep inelastic scattering (DIS). It will be particularly interesting since it is a direct measurement of neutrino couplings to the Z bosons. Nowadays the most precise measurement of $\sin^2\theta_W$ in DIS was made by the NuTeV experiment with a measured value compatible to the one expected in the SM at a level of 3σ [48]. A strategy to measure the $\sin^2\theta_W$ measurement will exploit the ratio of neutrino NC and CC DIS interactions

$$R^\nu \equiv \frac{\sigma^\nu_{NC}}{\sigma^\nu_{CC}}. \tag{3.2}$$

Thanks to the STT tracking capability, it will be possible to efficiently identify the ν_e CC interactions and separate the NC interactions from the CC ones, making possible to significantly reduce the systematic uncertainties with respect to former experiments. A precision of 0.35% on $\sin^2\theta_W$ seems be achievable exploiting the ν-N DIS interactions.

Another independent way to measure $\sin^2\theta_W$ is through NC ν_e-e elastic scattering. This channel is not affected by hadronic uncertainties but it is limited by the low statistics due to its small cross section. Using this channel the value of $\sin^2\theta_W$ can be find out from the ratio:

$$R_{\nu e} \equiv \frac{\sigma(\overline{\nu}_\mu e \to \overline{\nu}_\mu e)}{\sigma(\nu_\mu e \to \nu_\mu e)}, \tag{3.3}$$

in which the systematic uncertainties that arise from the electrons selection and identification cancel out [49]. The ν_μ and the $\overline{\nu}_\mu$ fluxes needed for the determination of $R_{\nu e}$ are measured using the $\nu(\overline{\nu})$-H. SAND can measure ν_μ-e elastic events with small background which can be calibrated in situ with data. One possible way to increase the statistics consists in a combined analysis of the events collected in SAND and in the ND LArTPC detector. In this way the STT reduces the systematic uncertainties while the LArTPC increases the statistics. It seems possible to achieve an overall relative precision of $\sin^2\theta_W$ from ν-e of 1% or better. The DIS and the ν-e channels are characterized by different scale of momentum transferred; this fact represents an excellent tool to test the running of the value of $\sin^2\theta_W$ in a single experiment.

Isospin Physics, Nucleon Structure and QCD Studies

A very interesting physics topic that could be investigated using the SAND detector is the study of isospin physics using neutrino and antineutrino interactions. The availability of the large samples of $\nu(\bar{\nu})$-H interactions allows to deduce the isospin, the number of valence u and d quarks of the target through the test of both the Adler sum rule [50] and of the Gross-Llewellyn-Smith sum rule [51].

SAND will also offer both a precise calibration of the uncertainties on the energy scale and an excellent precision in the determination of both neutrino and antineutrino fluxes. These peculiar feature will permit to this detector to measure the structure functions and cross-sections with an accuracy comparable to the one achievable in electron-scattering experiments. The different structure functions F_2, xF_3, F_L, F_T that can be determined from (anti)neutrino DIS will permit to shed light on the flavour structure of the nucleon [52].

Thanks to the statistics and the energy reachable in DUNE, the antineutrino and neutrino data collected using SAND could be used to perform global QCD analyses to study the parton distribution functions, perturbative and non-perturbative corrections in a wide range of the momentum transfered Q^2 and Bjorken x variable. The presence of H and other various nuclear targets (Ar, C) makes possible to separate valence and sea quark distributions, d and u quark distributions, the strange quark s and $\bar{s}$ distributions.

Studies of (Anti)Neutrino-Nucleus Interactions

As we already seen in the Section 3.2.3, the presence of various nuclear targets within the SAND detector permits to perform studies on the nucleon structure and the related nuclear effects on the structure functions, form factors and cross-sections. Moreover, it will be possible to study how the nucleon structure is modified when the nucleon is in the medium of an heavy nucleus. It will be also possible to make studies on the final state interaction (FSI); these are important because they introduce substantial smearing of the kinematic variables reconstructed from the observed final-state particles.

Searches for New Physics

Using the detector described in this chapter it will be also possible to study possible Beyond Standard Model (BSM) physics effects. The excellent electron identification capability and resolution of the STT make SAND very suitable to test the low energy anomaly found by the MiniBooNE experiment, with a different detector and different energies but with similar L/E. There are various possible explanation that could be tested in order to understand the origin of this anomaly including both SM and BSM physics. One of them is the oscillation with sterile neutrino that can be detected using both the CC ratios $R_{e\mu}(L/E) \equiv (\nu_e N \to e^- X)/(\nu_\mu N \to \mu^- X)$ and $\bar{R}_{e\mu}(L/E) \equiv (\bar{\nu}_e N \to e^- X)/(\bar{\nu}_\mu N \to \mu^+ X)$ and NC/CC ratios $R_{\nu p}$ and $R_{\bar{\nu} p}$ as a function of L/E.

In addition the SAND has an excellent sensitivity to ν_τ appearance. The τ neutrino could be the result of either oscillations with sterile neutrinos or non-standard interactions (NSI) [53]

The detector can also improve the sensitivity of the ND complex to searches for Dark Sector physics including for example heavy sterile neutrinos, light (sub-Gev) matter, dark photons.

Chapter 4

Simulation tools

The simulations performed for the scope of this thesis requests the usage of different software tools. I choose the ones recommended by the Near Detector Design Group (NDDG) [54]. The geometry of SAND is generated by dunendggd [55], a software based on General Geometry Description [56](Section 4.1). The neutrino interactions are generated using Genie (Section 4.2) while the propagation of the charged particles produced in the interactions and the detector response is simulated using edep-sim [59](Section 4.3), a toolkit based on Geant4. Finally it is developed a C++ code to perform the signal digitization of the ECAL and the STT (Section 4.4) and track reconstruction (Section 4.5).

4.1 General Geometry Description

The General Geometry Description (GGD) is a Phython based software that allows to generate a Geometry Description Markup Language (GDML) file for the representation of a constructive solid geometry [56]. The GDML are files that can be used as input for various simulation software such as GENIE and Geant4. For this reason a GGD based tool, dunendggd, with the purpose to study different geometry configurations for DUNE Near Detector has been developed [55]. In Fig. 4.1 a representation of the ND hall with the LArTPC, the MPD and the SAND detectors generated with dunendggd is shown. The SAND layout is represented in Fig. 4.2 and in Fig. 4.3 and its main components, the ECAL and the STT, will be better described in the following subsections.

4.1.1 The ECAL geometry

For the generation of the geometry of the ECAL described in Section 3.2.2 some approximations are applied based on previous simulations made by the KLOE collaboration. The first approximation is in the composition of the calorimeter module, either the barrel

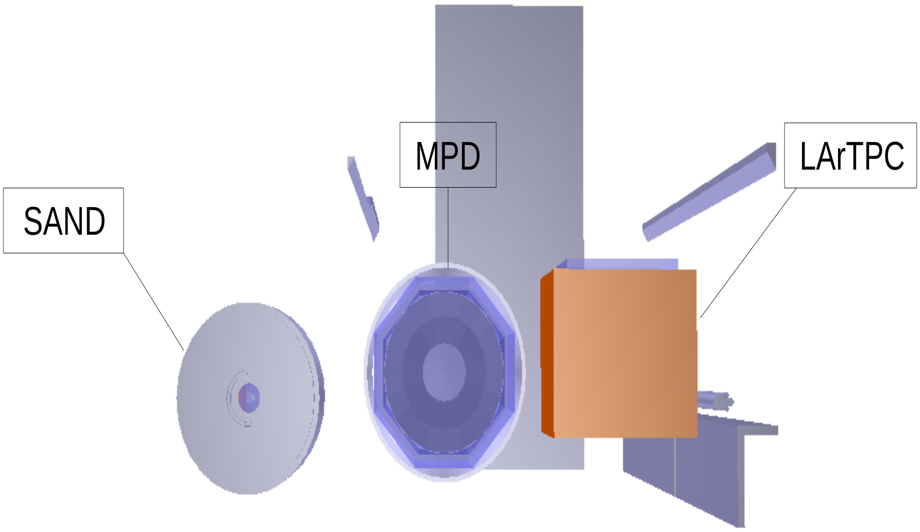

Figure 4.1: Geometry of the ND hall with the LArTPC, MPD and SAND detectors generated with dunedggd. This representation is drawn using the ROOT OGL tool. The neutrino direction is from the right to the left.

or the end-cap ones; it is composed alternating 209 slabs of plastic scintillator with layers of lead. The scintillator slabs are 0.07 cm thick and the lead ones are 0.04 cm thick. The second approximation applies to the end-caps modules that are approximated into two hollow cylinders of inner diameter 41.6 cm and outer diameter of 400 cm. The end-cap and the barrel segmentation is performed in the digitization step as it will be explained in Section 4.4.1. In Fig. 4.4 the generated ECAL geometry is represented, while in Fig. 4.5 and 4.6 a barrel and an end-cap module are shown respectively.

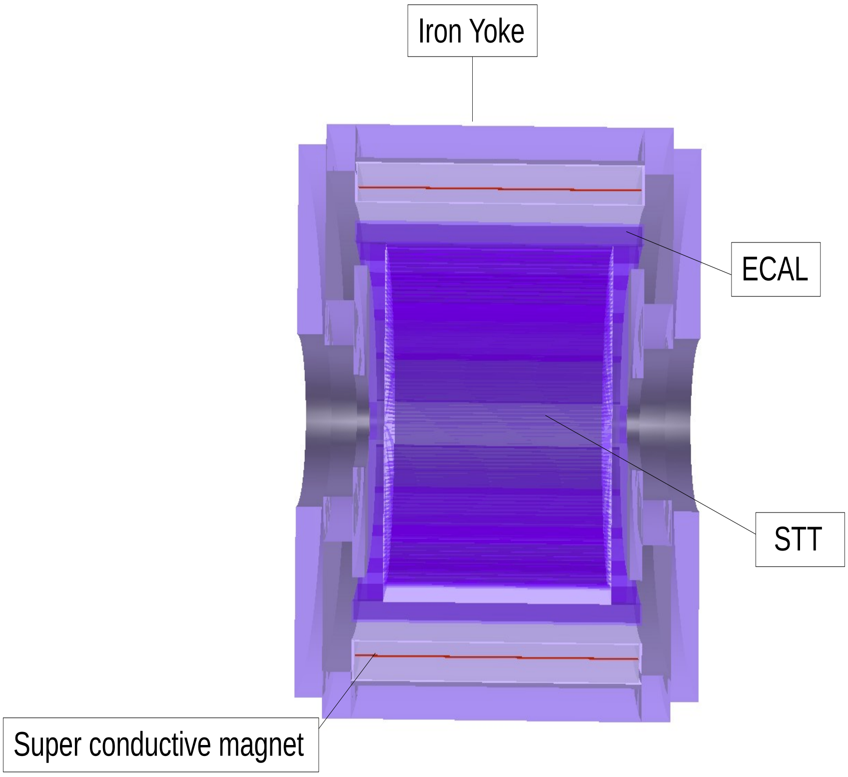

Figure 4.2: The front view of the SAND detector geometry generated with dunendggd and drawn with the ROOT OGL tool. The main components of this detector are highlighted in the figure. The neutrino beam direction is toward the page.

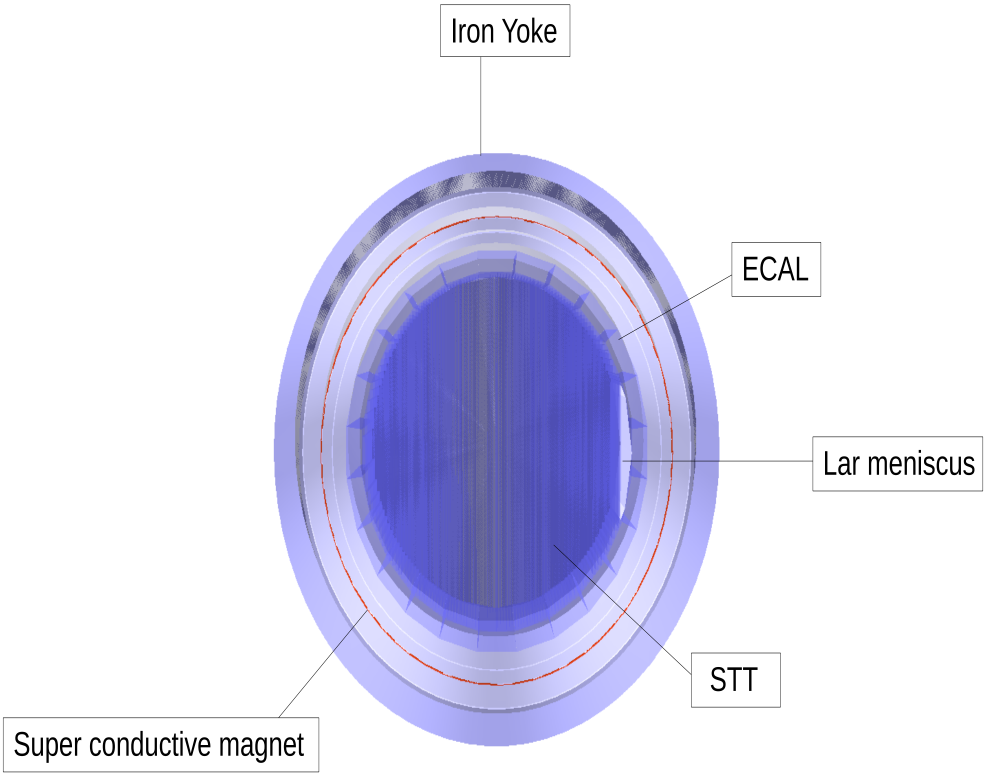

Figure 4.3: The lateral view of the SAND detector geometry generated with dunendggd and drawn with the ROOT OGL tool. The main components of this detector are highlighted in the figure. The neutrino direction is from the right to the left.

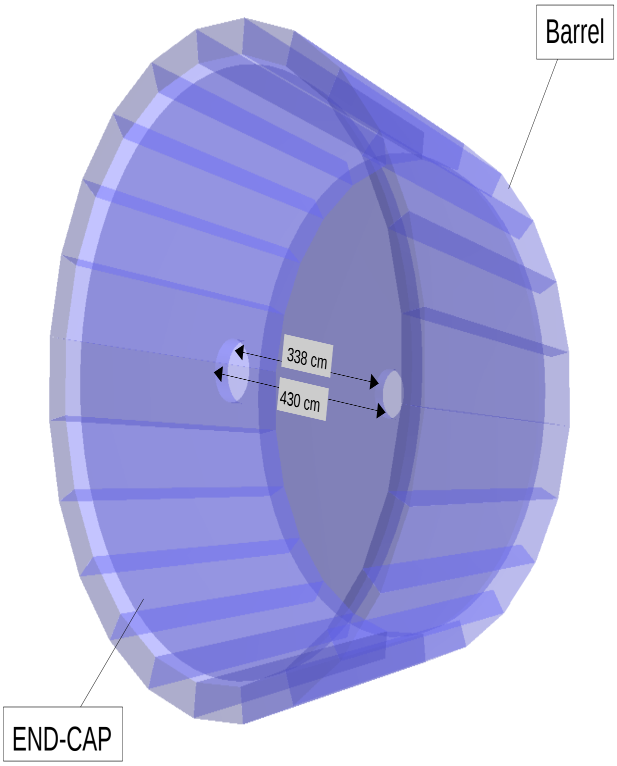

Figure 4.4: The ECAL geometry generated with dunendggd. The distances between the two inner faces of the end-caps is 338 cm and the length of the barrel section is 430 cm.

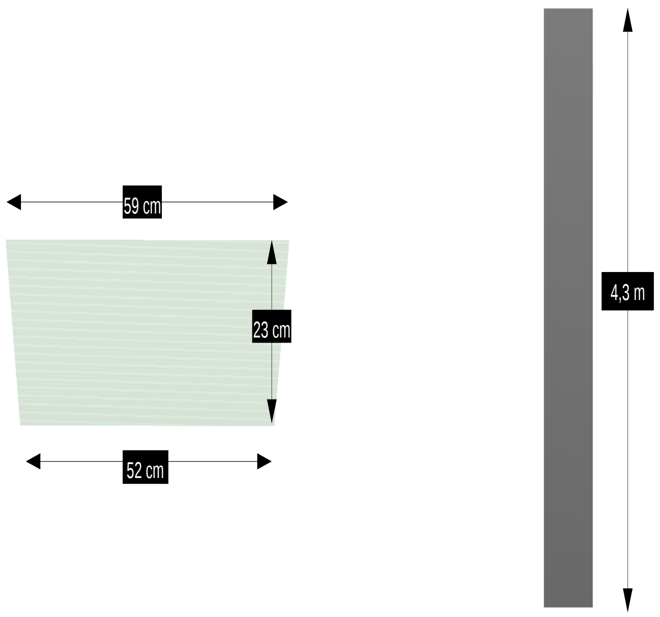

Figure 4.5: A barrel ECAL module generated with dunedggd. On the left the cross-section of the module is shown, on the right is the lateral view is displayed.

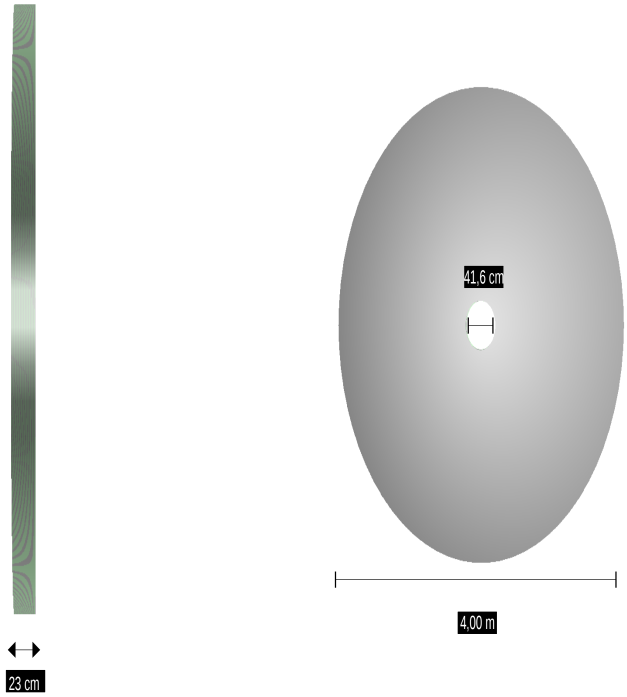

Figure 4.6: An end-cap ECAL module generated with dunegged. On the left the lateral view of the module is shown, on the right a front view is represented

4.1.2 The STT geometry

The inner tracker design used in the simulation is the same as the one described in Section 3.2.3. Summarizing, it is composed by:

- A module composed by only two straw tube XXYY planes.
- The standard polypropylene modules, composed of 150 foils TR radiator, a CH_2 target slab and XXYY straw tube tracking planes.
- The graphite modules composed of a pure C target slab and XXYY straw tube tracking planes.
- The slab-less modules, which only include the TR radiator and the XXYY straw tube tracking planes.

The dimensions and the composition of the element of the STT modules are coherent with the ones described in the previous chapter as well as the positioning of the modules. While the thickness of the module is constant for the various kind of the modules, their xy planes area varies so that the corners fit the internal side of the calorimeter modules. A representation of the STT tracker is shown in Fig. 4.7.

4.2 Neutrino MC events generator: GENIE

Until quite recently, most of the neutrino experiments developed their own neutrino event generator, each optimized for the energies, nuclear targets, detectors and physics topics relevant for the experiment. Such a situation makes a global independent evaluation of the state-of-art in neutrino interaction generators virtually impossible. In addition to this, these legacy physics generator were not keeping up with the latest theoretical ideas and experimental measurements due to the limited manpower and the fragility of the overextended software architecture. Nowadays particular importance is given to the neutrino energy region of few GeV, since these energies are relevant for some of the current and future Long-Baseline accelerator experiments such as DUNE. This broad energy range connects the perturbative and the non-perturbative pictures of the nucleon and a lot of different scattering mechanism. Often cross section, hadronization and nuclear models have different ranges of validity and need to be pieced together in order to cover all of the available phase space. This introduce challenges in merging and tuning models avoiding double counting and discontinuities. There are also kinematic regimes which are outside the range of validity of all the available models; in this case the appropriate models have to be developed from scratch.

GENIE is a ROOT-based neutrino MC event generator specifically developed to overcome these limitations. It is designed using object-oriented methodologies and developed

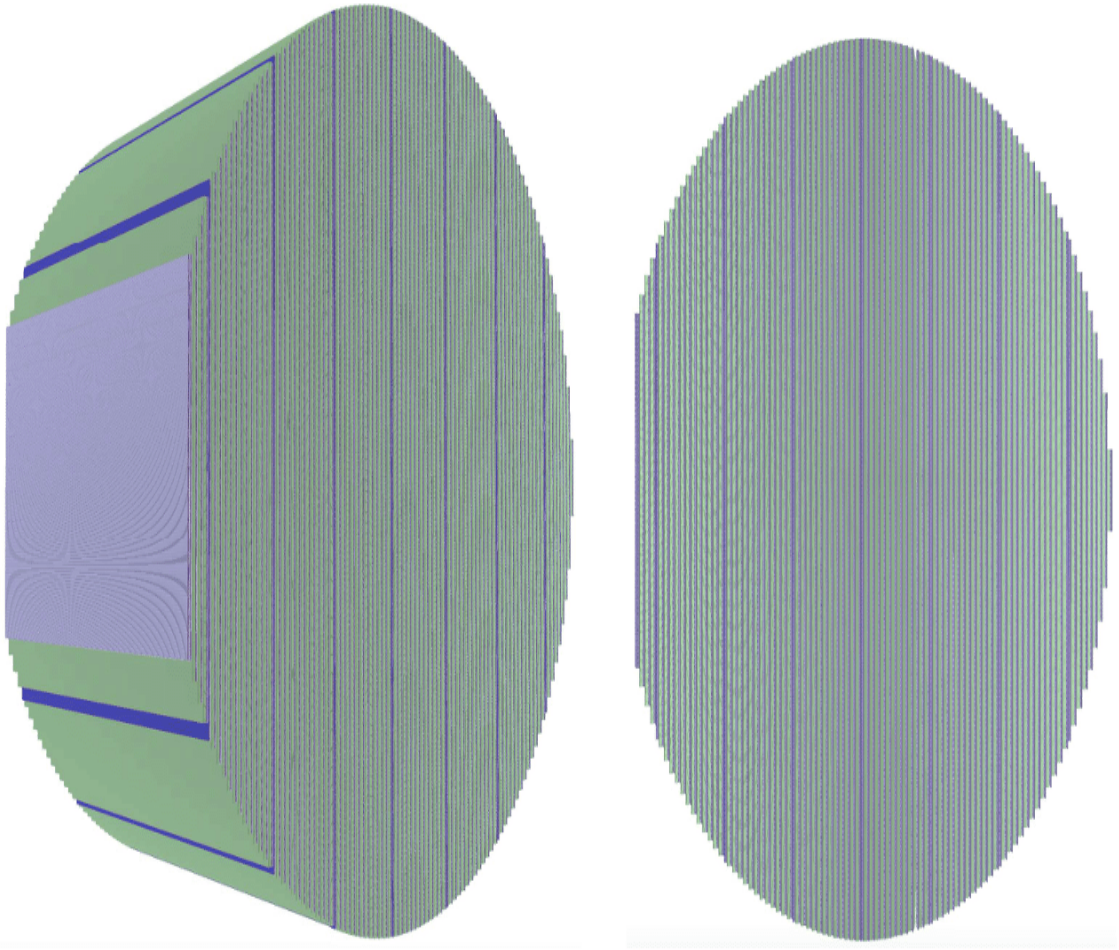

Figure 4.7: Views of the STT generated with dunegged. The CH2 module are colored in green while the graphite modules are colored in blue.

entirely in C++. It is adopted by the majority of the neutrino experiments [58]. The long-therm goal of GENIE is to be a canonical neutrino-interaction generator whose validity is extended to all nuclear targets and neutrino flavours over a wide spectrum of energies, from few MeV to some PeV.

4.2.1 The neutrino events generation

The generation of neutrino event is performed with gevgen_fnal program [54]. It is a GENIE-based event generator for the Fermilab experiments: it integrates GENIE with the Fermilab neutrino beamline simulations and with geometry descriptions of several detectors such as MINOS, NOνA, SBND and DUNE. GENIE takes as input a neutrino flux and a geometry representation and gives as output a file that records event informations regarding the simulated process. In particular, for each event, there is a list of particles that exit the struck nucleus after the scattering interactions, hadronizations and final state interactions. The output file is then processed by edep-sim (see Section 4.3) for the simulation of the particle propagation through the detector.

The geometry representation utilized as input for GENIE can be in a GDML or ROOT format. For the scope of this thesis it is utilized a GDML geometry produced with dunedggd, as we have seen in Section 4.1.

The fluxes files are produced by the LBNF beam group. These files can be in a variety of formats:

- dk2nu holds informations of the decays of the neutrino's parent particles.
- a ntuple containing flux information with a minimal format flux class within GENIE for storing flux info.
- 1-D histograms in a ROOT file (TH1D) representing the fluxes as a function of the neutrino energy for the ND and for the FD. The files contain fluxes for both neutrino (FHC) and antineutrino mode (RHC).

For the simulation that has been performed in this thesis the histogram file format has been used. The fluxes refer to the optimized 3-Horn Design presented in the Beam Optimization Review of October 2017 [57].

The cross-sections for individual sub-processes are pre-calculated as a function of neutrino energy and stored in XML formatted splines. The ones used for the scope of this thesis are partially the pre-generated ones recommended by the NDDG partially new ones generated using GENIE's internal spline generator.

4.3 EDEP-SIM: particle propagation

The energy deposition simulation (edep-sim) is a wrapper of GEANT4 software intended to simulate all of the particle propagation and geometry related issues [59]. The simulation implements a fairly detailed model of the energy deposited as ionization and scintillation. This is implemented using the NEST model [60].

Edep-sim takes as input a particle kinematic file and a geometry file. Edep-sim supports a lot of kinematic particle file format including the ones produced by GENIE. The geometry file given as input to edep-sim can be in a ROOT format or in a GDML one.

The output is a standard ROOT file containing: a TGeoManager object with the detector geometry, and a TG4Event tree with the event data. The TG4Event encloses all the most relevant informations of each event such as the event ID, the primary particles, the particle trajectories and the energy deposition on the detectors. All of the values in the output file are given in CLHEP units. The output file uses the global coordinate system defined by the input geometry.

In Fig. 4.8, a representation of a particle propagation simulated by edep-sim is shown using its graphic tool: edep-disp. The event is a ν_μ CC interaction within the SAND detector.

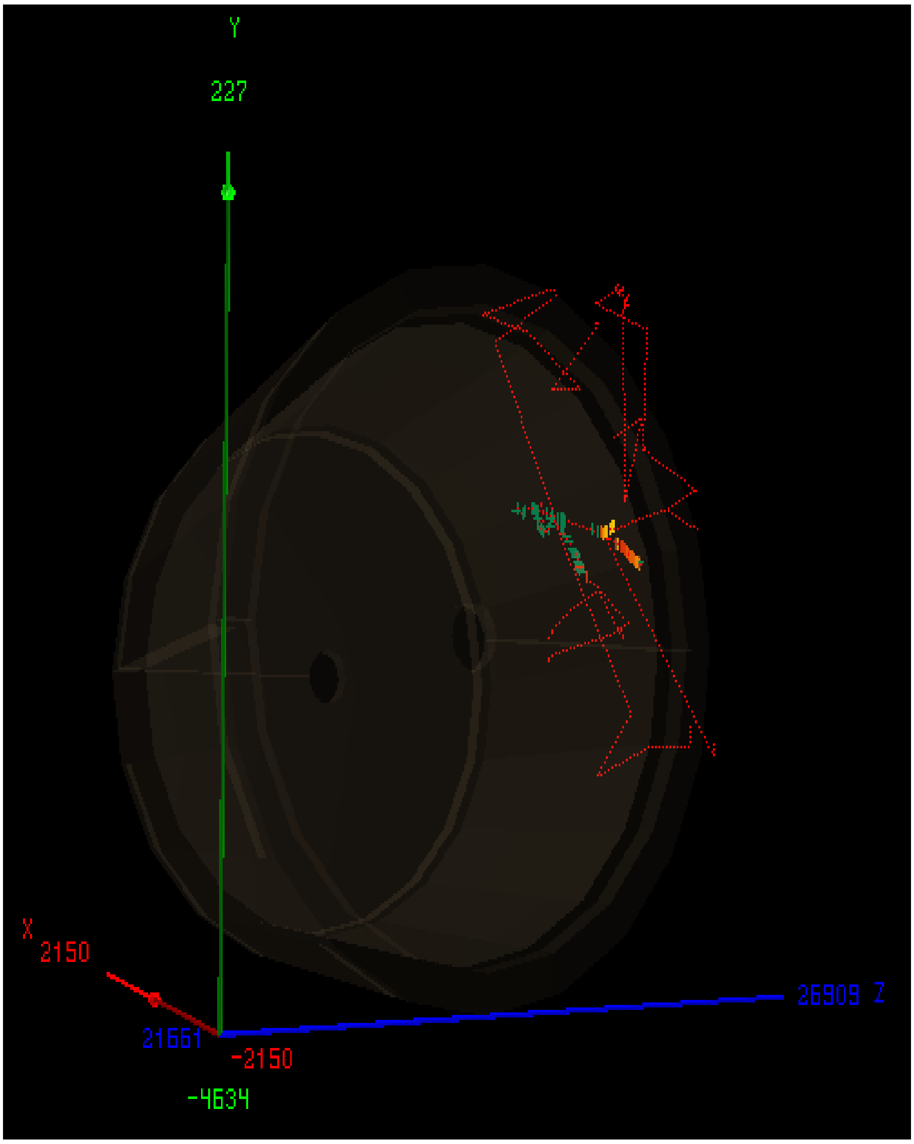

Figure 4.8: Simulation of a ν_μ CC interaction with the STT performed using edep-sim. The trajectories of the particles produced in the interaction (red lines), and the deposited energy hits (various colour dots) can be noticed.

4.4 Signal digitization

The signal digitization is the simulation of the signal production in the read-out systems of the detector, according to the energy deposition of the particles. For the ECAL this implies the segmentation of the calorimeter modules into cells and the simulation of the photo-electron production in the phototubes. For the STT the digitization consists into grouping the deposited energy hits in order to obtain digits and to assign them to the correct straw tube. A representation of the final result of the digitization step can be seen in the Fig. 4.9, that is the same event shown in Fig . 4.8.

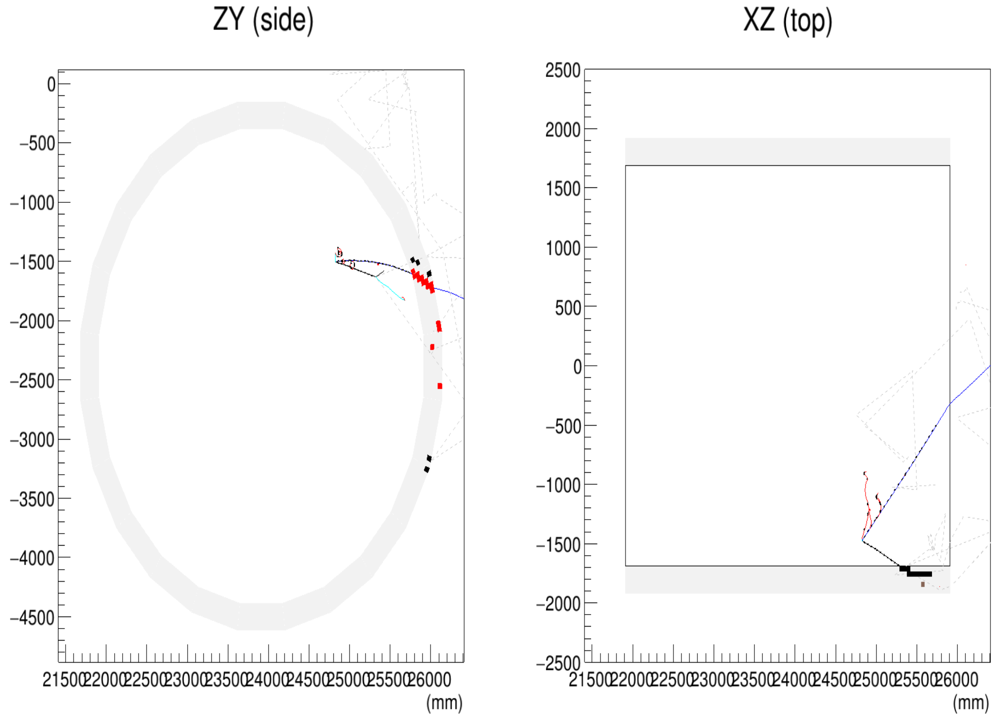

Figure 4.9: Representation of the digitized signal produced by the particles generated in a ν_μ CC interaction with the STT. The cells hit by the particles are colored in red and black while the hit on the STT are black dots. The particle trajectories are also highlighted, with the muon being colored in blue, the neutrons in grey, the electrons in red and the pion in cyan. The left panel presents a projection on the zy plane and the right one on the xy plane (z being the horizontal projection of the neutrino beam direction and y being the vertical axis).

4.4.1 The ECAL digitization

The ECAL digitization consists on the implementation of the segmentation of the calorimeter and on the signal production due to the crossing of a charged particle. This is done by a C++ program based on previous simulation of the KLOE experiment and adapted to the present work. First of all the calorimeter is composed by barrel and end-cap modules. Each barrel module is identified by an ID, from 0 to 23 starting from the top and going on following the clockwise rotation. The two end-cap modules are assigned an ID of 30 and 40. As we already seen in Section 3.2.2, each calorimeter module is read by phototubes placed at both ends. Concerning the barrel modules, the phototubes induce a segmentation into 5 layers. Starting from the inner part, four of these layers are 4.4 cm thick (each approximated by 40 scintillator and 40 Pb slabs) while the fifth is 5.4 cm thick (approximated by 49 scintillator and 49 Pb slabs). An ID that starting from the inner goes from 0 to 4 is assigned to the layers. Each layer is further subdivided into cells, 12 for each layer as shown in Fig.4.10. The phototubes induce also a segmentation of the end-caps module: 4 layers × 40 rectangular cross-section cells.

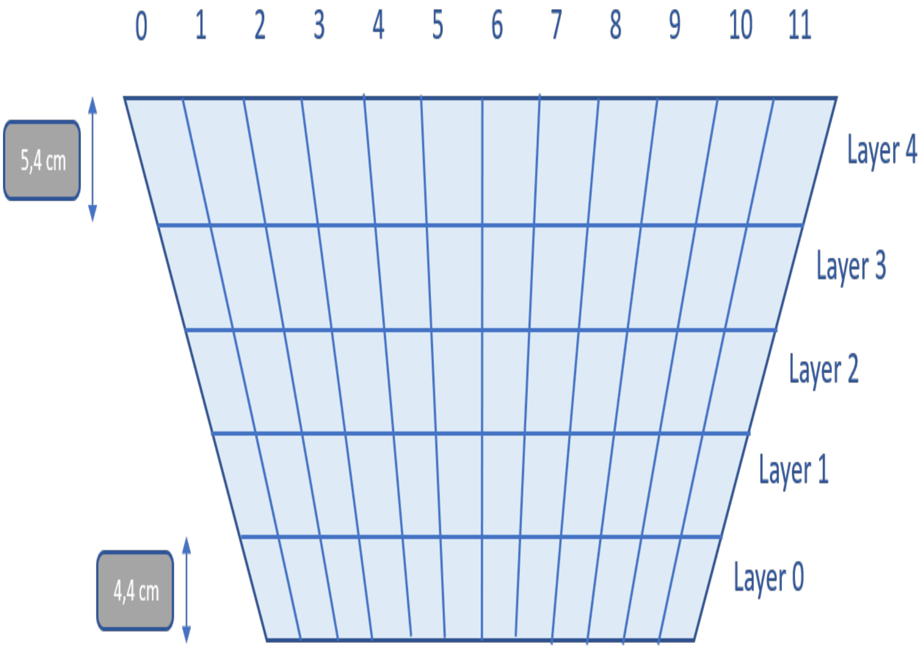

Figure 4.10: Graphical representation of the segmentation of one of the barrel calorimeter modules. The module is divided into five layers: the first four from the bottom are 4.4 cm thick and the last is 5.4 cm thick. Each layer is also divided into 12 horizontal cells.

Once the segmentation is performed, the signal of each cell of the ECAL is produced. From the edep-sim output tree we take the information regarding the hits that are in the plastic scintillator slabs of the modules. Each hit is assigned to the module were the slab is located automatically by edep-sim. Given the hit position, then we assign it to the correct cell. In addition to every hit is associated a time and an energy deposit. To the energy deposit is applied an attenuation factor in order to take into account the attenuation due to the propagation through fibers:

$$E_a = p_1 \times exp(-\frac{d}{alt_1}) + (1 - p_1) \times (-\frac{d}{alt_2}), \tag{4.1}$$

where d is the distance between the hit and the photo-cathode, p_1 is equal to 0.35, alt_1 is equal to 0.50 cm, alt_2 is equal to 430 cm for the planes 0 and 1, 380 cm for the plane 2 and 330 cm for the planes 3 and 4. Once the attenuation factor E_a is applied, the energy is converted into a number of photo-electrons using a conversion factor. The conversion factor is determined requiring that a 1 MeV energy deposit at half length of the barrel module results on average in 25 photo-electrons. The number of p.e. is so obtained from Poisson distribution having as its mean (μ):

$$\mu = 25 \times E_a \times dE, \tag{4.2}$$

where dE is the hit energy deposit. For each event the ADC (analog to digital converter) signal assigned to the phototubes is proportional to the total number of photo-electrons.

The arrival time at the phototube of the photo-electron is obtained as:

$$t_{p.e.} = t_{part} + t_{decay} + du_{ph} + \textbf{Gauss}(1\text{ns}), \tag{4.3}$$

where t_{part} is the time associated to the passage of the particle, t_{decay} is the scintillation decay time, d is the distance between the hit and the phototube, u_{ph} is the inverse of the velocity of the photons in the scintillating fibers and Gauss(1 ns) is the phototubes time resolution. The t_{decay} is obtained from the equation:

$$t_{decay} = t_{scint} \left(\frac{1}{r_{ph}(1)} - 1 \right)^{t_{scex}} \tag{4.4}$$

where t_{scint} is equal to 3.08 ns and t_{scex} to 0.588. The TDC (time-to-digital converter) time associated to each phototube is obtained as 15 % constant fraction discriminator. Two TDC times are assigned to each cells, t_{TDC1} and t_{TDC2}.

At the end of the digitization process of the ECAL, in the output file for each event and for every cell there are:

- the position of the center of the cell;
- the module, layer and cell ID and the module length;
- the two ADC values (ADC$_1$ and ADC$_2$);

- the two TDC times (t_{TDC1} and t_{TDC2});
- two arrays containing the photo-electron times in increasing order ($t_{p.e.1}$ $[N_{p.e.1}]$ and $t_{p.e.2}$ $[N_{p.e.2}]$);
- two index array linking the photo-electrons to the hits that produced them.

4.4.2 The STT digitization

The active components of each STT module are two double layers of straw tubes: the upstream one with straws placed horizontally (XX) and the downstream one with the straws placed vertically (YY). The digitization of the STT consists on grouping the hits produced into digits and to assign them a position, a time and an energy deposit.

First of all every hit is automatically associated by edep-sim to the straw, where it has been generated. In addition, each hit is characterized by an energy deposit, a starting and an ending point. To both these points is also associated a time. The hits that are in the same straw layer are then grouped and ordered temporally to have an array of hits with an increasing time associated. The hits are combined in the same digit only if the ending point of an hit coincides with the starting point of the following one. Either the y and the z coordinate if the layer is horizontal or the x and the z coordinate if the layer is vertical are assigned to the digit together with a time and an energy deposit. The temporal and the spatial coordinate of the digit are calculated as an average between the starting point of the first hit and the final point of the last his that compose the digit. The energy of the digit is the sum of the energy deposit associated to its hits.

In summary, each digit has the following information:

- the x/y, z coordinates and the time associated to each digit;
- the energy deposition of the digit;
- a flag that indicates if the straw tube where the digit occurs is horizontal or vertical;
- an index array mapping the digits to the hits that produced them.

4.5 Recontruction

The reconstruction is a C++ based code that exploits the informations from the digitization step. It is divided into two parts: one uses the informations from the STT digitization to perform the track reconstruction and a second part that reconstructs the cluster position in the ECAL. Firstly, a fit of the digits along the helicoidal trajectory described by a charged particle in the STT magnetized volume is applied. Later, the reconstruction on the initial momentum of the particles is performed. Finally the reconstruction of the energy deposition and of the position of the clusters of the ECAL cells is performed.

4.5.1 SAND ECAL: reconstruction

The informations from the ECAL digitization step are used to group the digitized signal of the the cells into the so-called cluster, each associated to a specific particle track. First of all every digit is associated to the particle track that produced the most photoelectrons in the cell. For each track we have a collection of digit, the cluster. Then for every digit in the cluster we evaluate the position and its time. The coordinate of the digit z_{dig} is always taken as the center of the cell. For the barrel modules, since they are placed horizontally along the x axis, the y coordinate y_{dig} is defined as the center of the cell while the x coordinate x_{dig} is calculated in the following way:

$$x_{dig} = \frac{t_{TDC1} - t_{TDC2}}{2u_{p.e.}} + x_{cell}, \tag{4.5}$$

where t_{TDC1}, t_{TDC2}, $u_{p.e.}$ are the parameters described in the Section 4.4.1 and x_{cell} is the x coordinate of the center of the cell. Concerning the digits of the cells in the end-cap modules the x_{dig} is calculated as the center of the cell while the y_{dig} is evaluated in the same way of the Eq. 4.5:

$$y_{dig} = \frac{t_{TDC1} - t_{TDC2}}{2u_{p.e.}} + y_{cell}, \tag{4.6}$$

where y_{cell} is y coordinate of the center of the cell. The time of each digit is calculated as

$$t = \frac{1}{2}(t_{TDC1} + t_{TDC2} - u_{p.e.} \times L) \tag{4.7}$$

where L is the length of the cell. The energy associated to the digit is the sum of $E_{dig} = \mathrm{ADC}_1 + \mathrm{ADC}_2$.

The cluster coordinates (x_{cl}, y_{cl}, z_{cl}, t_{cl}) are calculated by a weighted average of the digits position using the total energy for each digit E_{dig} as weights. The x_{cl}, for example, is given by

$$x_{cl} = \frac{\sum_i E^i_{dig}\ x^i_{dig}}{\sum_i E^i_{dig}}, \tag{4.8}$$

where the sum is extended to all the digits of the cluster taken into account. These values are stored in the output file together with the total energy deposition $E_{cl} = \sum_i E^i_{dig}$ and the variance. A similar weighted average is further performed in order to deduce the mean position and the time of the cluster calorimeter in each layer (x_{lay}, y_{lay}, z_{lay}, t_{lay}). These values are used to perform linear fits on the zx and zy planes to estimate the components of the direction versors of the particle trajectory in the calorimeter.

4.5.2 The track reconstruction

The trajectory of the particles are effected by the magnetic field $\vec{B} = 0.6$ T which is directed along the x axis. A charged particle in a magnetic field moves along an helicoidal trajectory, a composition of a linear motion along the direction x, parallel to the $\vec{B}$ and of a circular motion on the zy plane. The equations of motion of a charged particle moving in a magnetic field can be parametrized respect to the spatial progression along the trajectory s:

$$\begin{cases} z(s) = z_0 + R(\cos(\Phi_0 + \frac{hs\cos\lambda}{R}) - \cos\Phi_0) \\ y(s) = y_0 + R(\sin(\Phi_0 + \frac{hs\cos\lambda}{R}) - \sin\Phi_0) \\ x(s) = x_0 + s\sin\lambda \end{cases} \tag{4.9}$$

where $(x_0,\ y_0,\ z_0)$ could be an arbitrary point of the track, R is the radius of the circumference, Φ_0 is the angle between the z axis and the segment connecting the center of the circumference $(z_c,\ y_c)$ and $(z_0,\ y_0)$ in the zy plane (see Fig. 4.11), $h = \pm 1$ is the sense of rotation of the helix and λ is the angle between the initial velocity vector $\vec{v}$ and the plane perpendicular to the $\vec{B}$ direction, the plane zy [61]. Projecting the particle trajectory to the zy plane we obtain a circle, as shown in Fig. 4.11, whose equation can be written as:

$$(z - z_0 + R\cos\Phi_0)^2 + (y - y_0 + R\sin\Phi_0)^2 = (z - z_c)^2 + (y - y_c)^2 = R^2. \tag{4.10}$$

It is possible so to deduce the values of R and the position of the center $(z_c,\ y_c)$ performing a circular fit of the hits recorded in the horizontal planes. In order to make a complete track reconstruction we want also to find out the value of the dip angle λ. To this aim we perform an approximation of the circular motion on the zy plane to a parabolic motion applying a first order Taylor expansion in s/R. This approximation is valid if $s/R \ll 1$, i.e. if the portion of the circular trajectory described by the particle is small compared to the radius R. Then we also apply a change of variable from the angle Φ_0 to the angular direction of the track in the point $(x_0,\ y_0,\ z_0)$, $\varphi = \Phi_0 - \frac{\pi}{2}$. So we write $(y_0,\ z_0)$ as $y_0 = d_0\cos\varphi_0$ and $z_0 = d_0 - \sin\varphi_0$ where d_0 is the distance between the point $(y_0,\ z_0)$ and the origin in the zy plane. So the equations of motion become

$$\begin{cases} z(s) = -d_0\sin\varphi_0 + s\cos\lambda\cos\varphi_0 + \frac{h}{2R}s^2\cos\lambda^2\sin\varphi_0 \\ y(s) = d_0\cos\varphi_0 + s\cos\lambda\sin\varphi_0 + \frac{h}{2R}s^2\cos\lambda^2\cos\varphi_0 \\ x(s) = x_0 + s\sin\lambda \end{cases} \tag{4.11}$$

Moreover, we perform a coordinate rotation in the plane zy of an angle φ_0 in order to have the new coordinate ρ, that is directed along the track trajectory in in $(x_0,\ y_0,\ z_0)$:

$$\rho = z\cos\varphi_0 + y\sin\varphi_0, \tag{4.12}$$

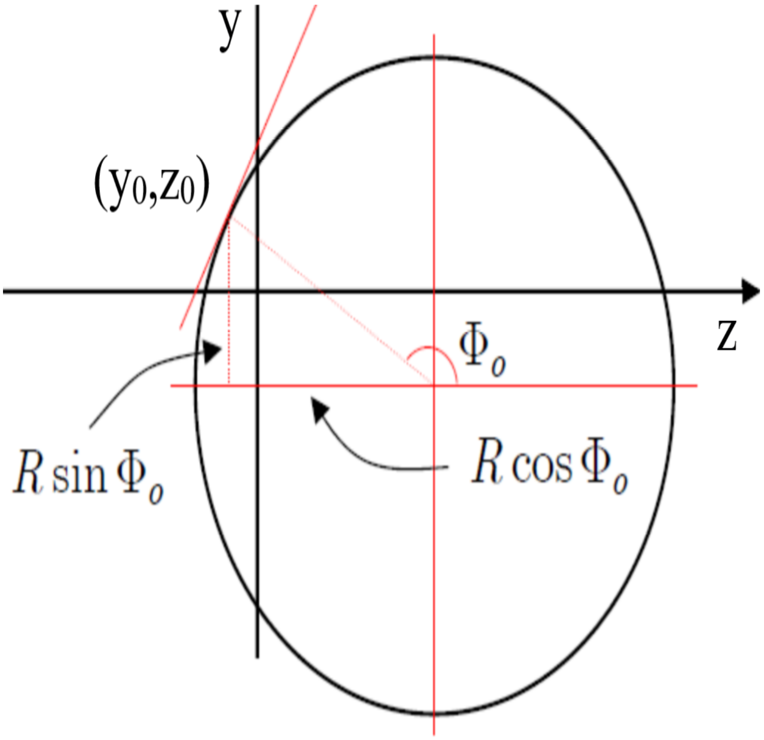

Figure 4.11: Projection of the helicodal motion on the zy plane.

$$y' = -z\sin\varphi_0 + y\cos\varphi_0. \tag{4.13}$$

After performing this change of coordinates the equation of motion can be rewritten as:

$$\begin{cases} x = x_0 + \rho\tan\lambda \\ y' = d_0 - \frac{h}{2R}\rho^2. \end{cases} \tag{4.14}$$

We can notice from the first equation that the parameter of a linear fit on the $x\rho$ plane results in the values of x_0 and of $\tan\lambda$. For this purpose we need the vertical coordinate (y) of the digits in the horizontal straw tubes;

$$y = y_c + h\sqrt{R^2 - (z - z_c)^2} \tag{4.15}$$

where the value of h (that can be equal to +1 for clockwise rotation and to -1 for counter-clockwise rotation) is obtained by the sum of the cross product between the segment in the zy plane that connects the position of a horizontal digit, let call it for more simplicity (y_i, z_i) , with the center of the circumference (y_c, z_c) and and the segment that connects the following horizontal digit (y_{i+1}, z_{i+1}) to the (y_i, z_i) one. In order to calculate ρ we need the values of $\sin\varphi$ and of $\cos\varphi$ that are evaluated as:

$$\cos\varphi = h\frac{(y_0 - y_c)}{R}; \tag{4.16}$$

$$\sin\varphi = -h\frac{(z_0 - z_c)}{R}. \tag{4.17}$$

Once the values of the radius R, of the coordinates of the center $(y_c,\, z_c)$, and of the dip angle λ have been find out, it is also possible to perform the reconstruction of the initial momentum of the particle. The initial transverse momentum p_t is

$$p_t = 0.3 \times R[m] \times B[T]. \tag{4.18}$$

From this value we can get the three components of the initial momentum of a particle,

$$\begin{cases} p_x = p_t \cos\varphi_0 \\ p_y = p_t \sin\varphi_0 \\ p_y = p_t \tan\lambda \end{cases} \tag{4.19}$$

.

Chapter 5

Selection of neutrino interaction event

As explained in Chapter 3 the major task of the SAND detector is to precisely measure and monitor the neutrino beam energy spectrum. For this purpose it is essential to identify neutrino interactions occurring in the SAND detector internal volume and reject external background whose main contribution is from neutrino interactions in the SAND magnet and in particular in the iron yoke.

In this work of thesis I define, develop and optimize an automatic selection of the internal neutrino interactions exploiting the topology of the event and its timing information. To this aim I generate 10000 ν_μ interactions in the SAND internal volume (internal events) and other 10000 in the whole SAND detector excluding the internal volume (external events). The interactions are both CC and NC and all the processes are simulated by GENIE according to their cross-sections. The neutrino energy spectrum refers to the optimized 3-Horn Design presented in the Beam Optimization Review of October 2017. The detector response is simulated using edep-sim and the digitization are performed as described in Chapter 4. For each event, either internal or external, the tracks are used to reconstruct a vertex. The position of the reconstructed vertex is used to classify the event. If a vertex is not reconstructed, the vertex position is defined as the position of the upstream STT digit among the tracks. Since the electromagnetic calorimeter lays almost in direct contact with the STT, a first improvement can be achieved excluding interaction vertexes reconstructed near the boarders of the internal volume. To this aim, a reasonable fiducial volume (FV) is defined as the volume that is 20 cm far from the inner surface of the ECAL.

The neutrino vertex reconstruction is performed by a vertexing algorithm described in Section 5.1.2. If the vertex position lays inside the FV, the event is classified as signal, background otherwise. A further improvement is then achieved exploiting the time information of the event. In Section 5.1.1 and 5.1.3 I validate the track reconstruction and optimize the vertexing algorithm. The results are reported in Section 5.2. In Section 5.3 I perform a background classification in order to elaborate strategies to reduce it. Section 5.4 and 5.5 are devoted to the implementation of selection based on the time information of the event.

5.1 Reconstruction of neutrino interactions

5.1.1 Validation of the track reconstruction

As a first step I evaluate the performance of the track reconstruction. For the internal events sample the transverse momentum p_t and the dip angle λ resolution for muons and pions is evaluated. In Fig. 5.1 and 5.2 the reconstructed p_t as a function of the true p_t for muons and pions are shown respectively while in Fig. 5.3 and 5.4 the reconstructed dip angle λ as a function of the true λ for muons and pions respectively are represented.

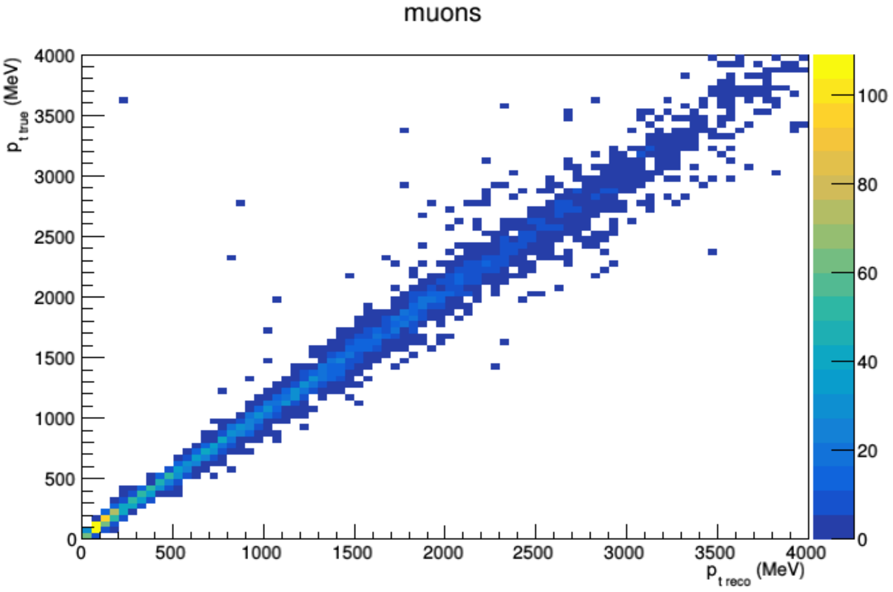

Figure 5.1: Reconstructed muons p_t as a function of true p_t.

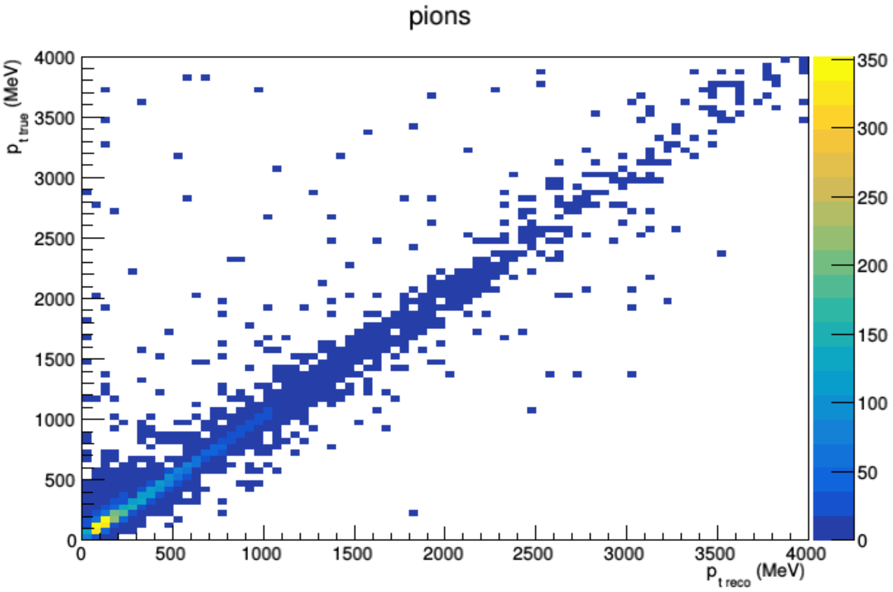

Figure 5.2: Reconstructed pions p_t as a function of true p_t for the internal events.

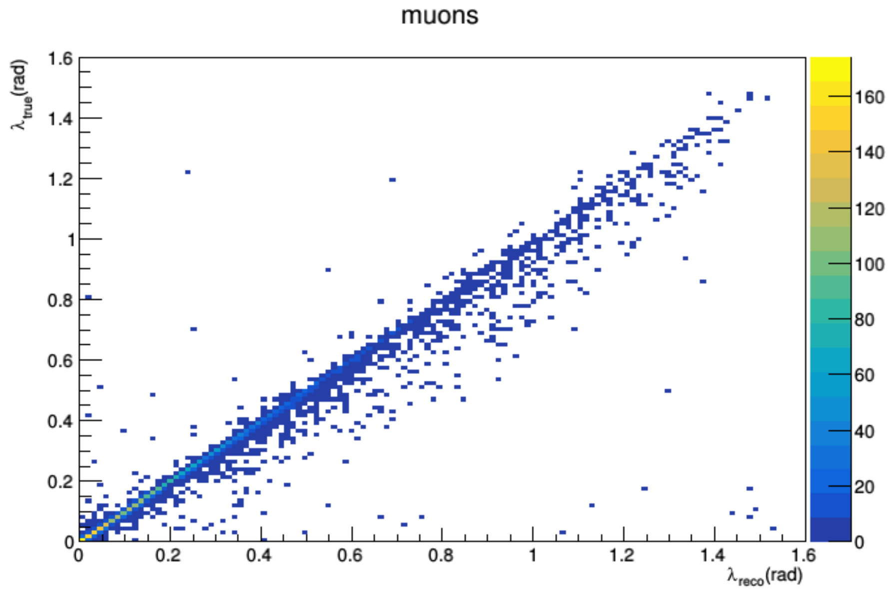

Figure 5.3: Reconstructed muons λ as a function of true λ.

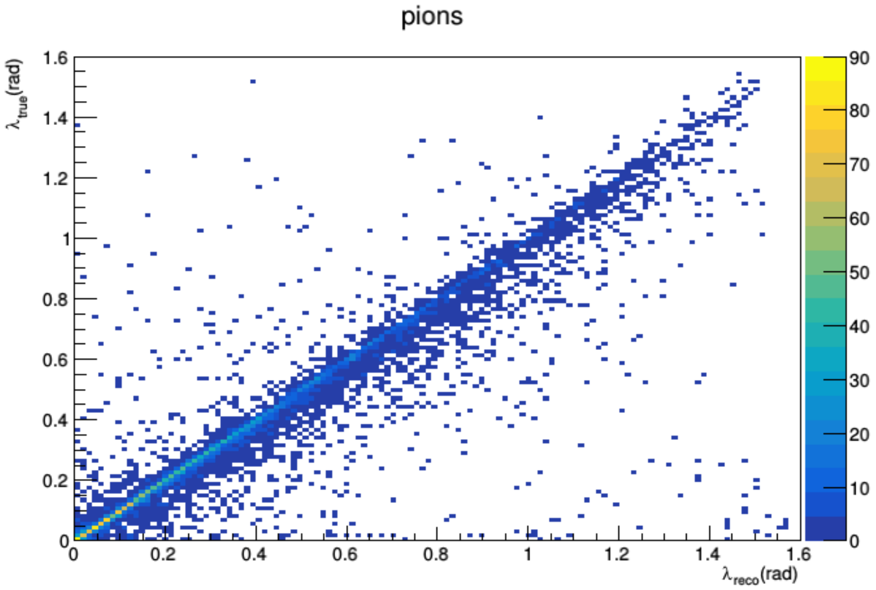

Figure 5.4: Reconstructed pions λ as a function of true λ.

The p_t and λ resolution is then found as the standard deviation of the distribution of $1-\frac{p_t^{\mathrm{true}}}{p_t^{\mathrm{reco}}}$ and of $\lambda^{\mathrm{reco}}-\lambda^{\mathrm{true}}$ respectively. The distribution of $1-\frac{p_t^{\mathrm{true}}}{p_t^{\mathrm{reco}}}$ is shown in Fig. 5.5 and 5.6 while the distribution of $\lambda^{\mathrm{reco}}-\lambda^{\mathrm{true}}$ is shown in Fig. 5.7 and 5.8 for muons and pions respectively. The obtained p_t and λ resolution found are summarized in Table 5.1.

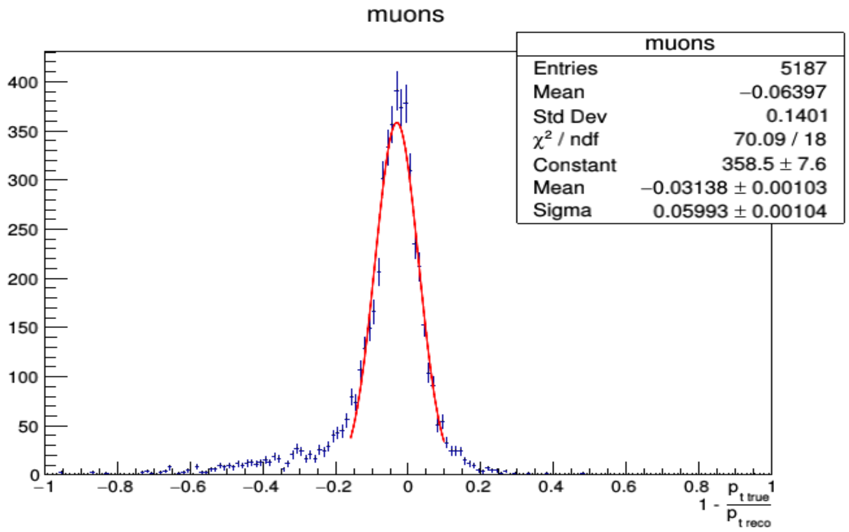

Figure 5.5: $1-\frac{p_t^{\mathrm{true}}}{p_t^{\mathrm{reco}}}$ distribution for muons. The obtained resolution is about 6%.

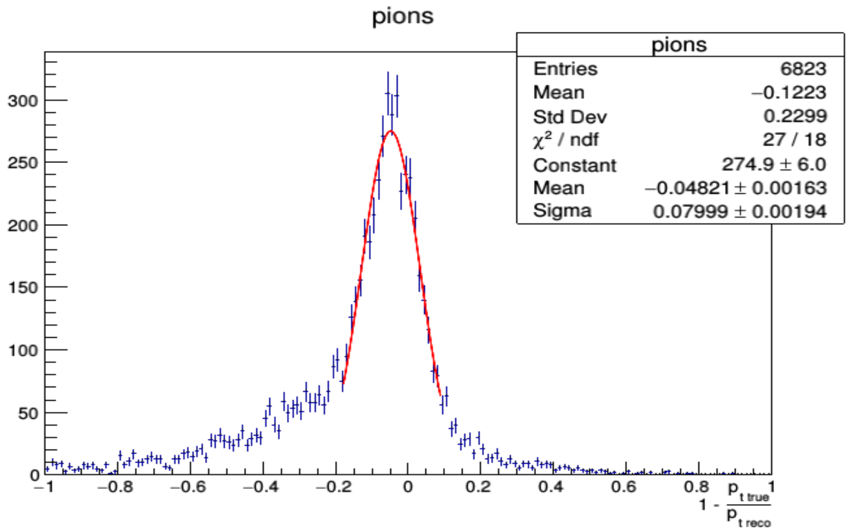

Figure 5.6: $1 - \frac{p_t^{\text{true}}}{p_t^{\text{reco}}}$ distribution for pions. The obtained resolution is about 8%.

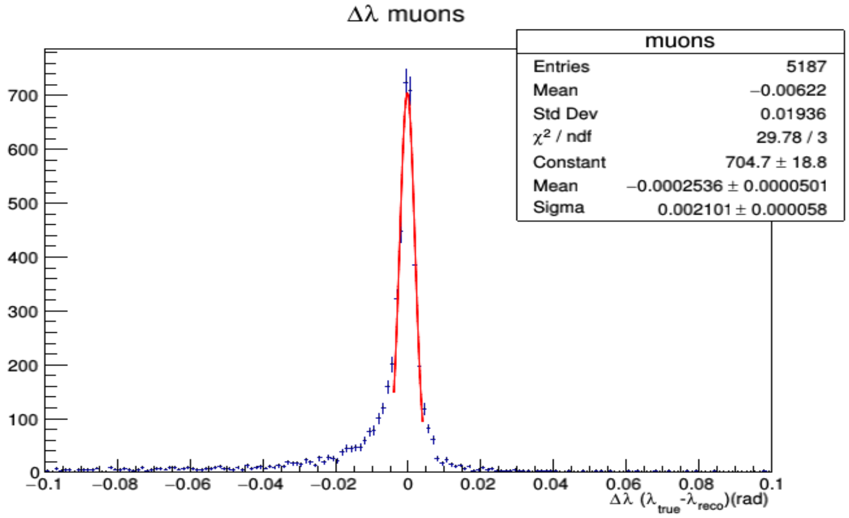

Figure 5.7: $\lambda^{\text{reco}} - \lambda^{\text{true}}$ distribution for muons. The obtained resolution is about 2 mrad.

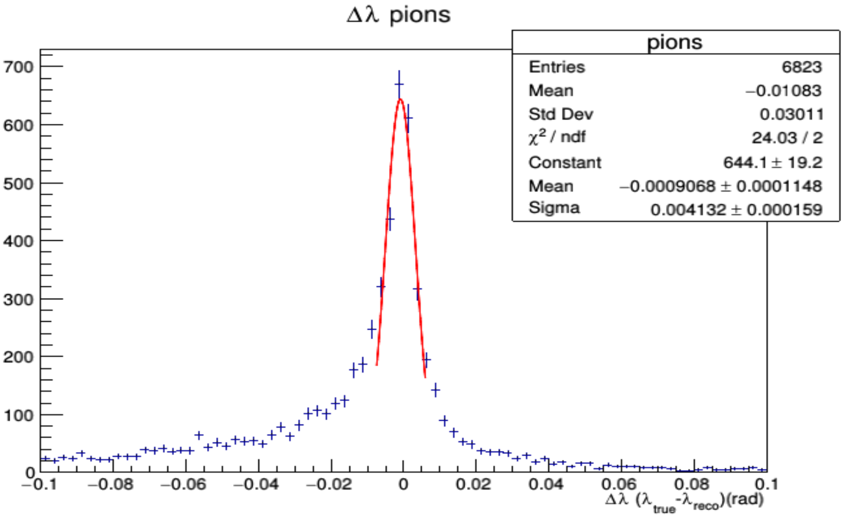

Figure 5.8: $\lambda^{\text{reco}} - \lambda^{\text{true}}$ distribution for pions. The obtained resolution is about 4mrad.

Particle	σ_{p_t}	σ_λ
μ	6%	2 (mrad)
π	8%	4 (mrad)

Table 5.1: p_t percentage and λ resolution of muon and pion reconstructed tracks of the internal event sample.

5.1.2 The vertexing algorithm

In order to reconstruct the neutrino interaction point it has been developed a vertexing algorithm. For each couple of reconstructed tracks, let call them i and j, the algorithm calculates the vertex V_{ij} (also referred to as 2-Prong vertex) as the midpoint of the 3D minimum distance segment that connects the two tracks. The V_{ij} vertex is then discarded if:

- the 3D minimum distance between V_{ij} and the tracks, that is also commonly called *impact parameter* (IP), is bigger than the input parameter *max IP*;
- the distance on the z axis between V_{ij} and the initial point of the track (that we also called for simplicity dz) is bigger than the input parameter *max dz*.

The 2-Prong vertexes that satisfy these conditions are then recursively merged if their 3D distance is less than the input parameter *merging radius*. The final vertex position is evaluated as the one minimizing the sum of the IPs of the connected tracks. If an event has more than one vertex the most upstream one is chosen as the neutrino vertex.

5.1.3 Choice of *max dz*, *max IP* and *merging radius*

To find the values of the three input parameters *max dz*, *max IP* and *merging radius* I determine the IP and the two dz values for each 2-Prong vertex associated to primary particle tracks. The fraction of tracks with dz less then dz_{cut} as function of dz_{cut} for internal events are shown in Fig. 5.9. Fig. 5.10 shows the fraction of 2-Prong vertexes with IP less then IP_{cut} as function of IP_{cut}. Then for each event I also calculate the distances between the 2-Prong vertexes. The value of *max dz* is chosen as the value for which the fraction of the tracks is equal to the 90% while the values of the *max IP* and *merging radius* are selected as the one for which the fraction of the 2-Prong vertexes are equal to the 90%. As seen from the Fig. 5.9, 5.10 and 5.11, the optimal values of *max dz*, *max IP*, *merging radius* are equal to 30 mm, 11 mm and 50 mm respectively.

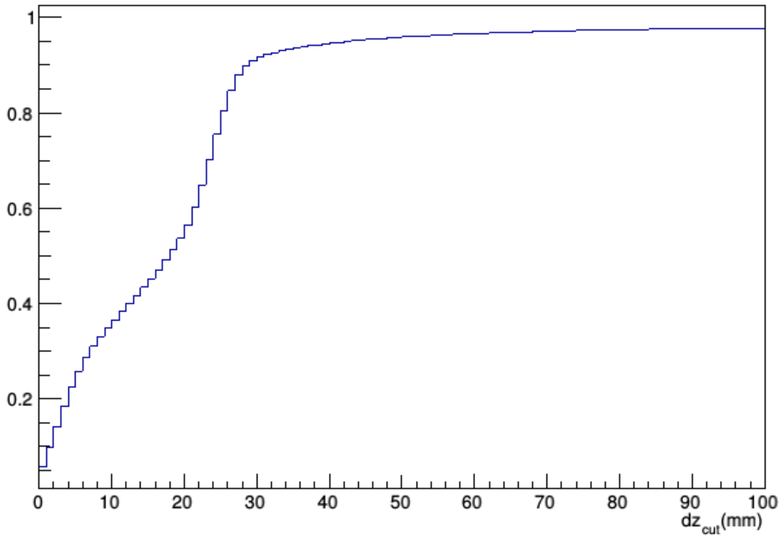

Figure 5.9: Fraction of tracks with dz less then dz_{cut} as function of dz_{cut} for internal events.

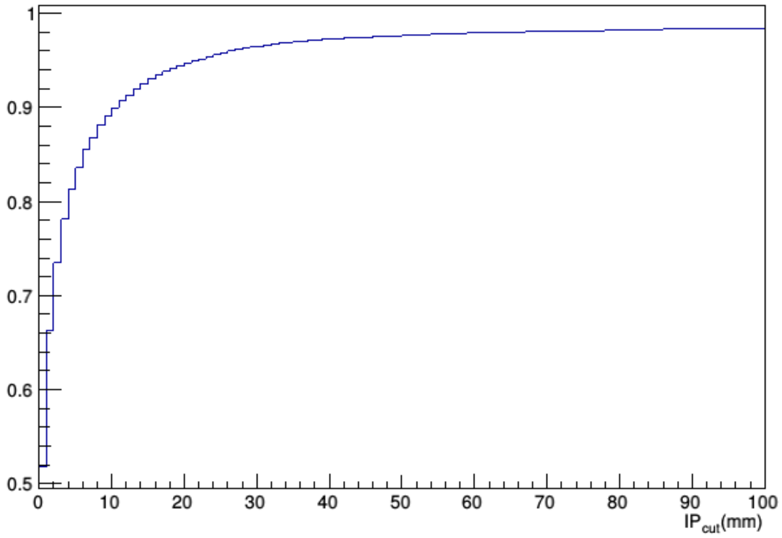

Figure 5.10: Fraction of 2-Prong vertexes with IP less then IP_{cut} as function of IP_{cut}.

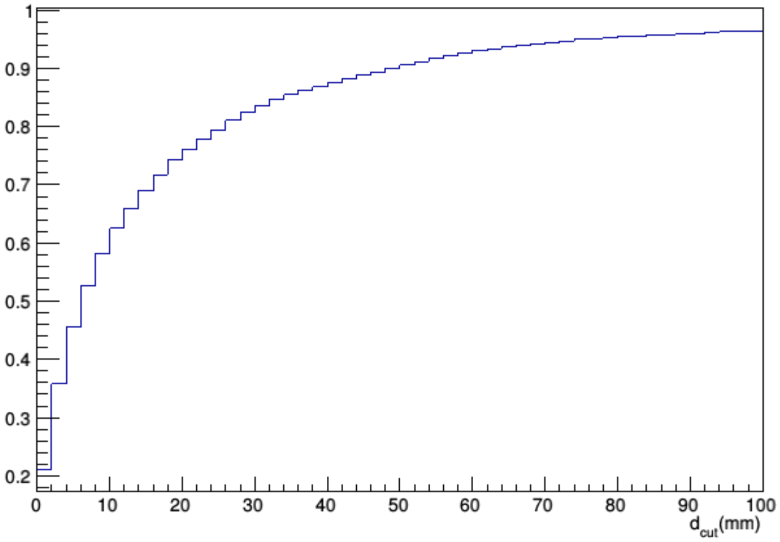

Figure 5.11: Fraction of 2-Prong vertexes with distance less then d_{cut} as a function of d_{cut}.

5.2 Preliminary results

Once I have optimized the three parameters, I apply the vertexing algorithm both to internal and external event samples. If an event has more than one vertex the most upstream one is chosen. If an event has no reconstructed vertex, the position of the most upstream digit of the reconstructed tracks is taken as the vertex position. Once the vertex has been previously defined, the efficiencies for the internal and external events are estimated as

$$\varepsilon_{int} = \frac{N_{reco\ in\ FV}}{N_{in\ FV}}, \tag{5.1}$$

$$\varepsilon_{ext} = \frac{N_{reco\ in\ FV}}{N_{out\ FV}}, \tag{5.2}$$

respectively. In the equations above $N_{reco\ in\ FV}$ is the number of events with the neutrino vertex inside the FV, $N_{in\ FV}$ is the number of event with the interaction point inside the FV and $N_{out\ FV}$ is number of event with the neutrino interaction point outside the FV. The results for the internal and the external events are summarized in the Table 5.2 and 5.3 respectively. The vertexes with only one track associated are referred to as single-Prong vertexes while the vertexes with more than one track associated are referred to as multi-Prong vertexes.

Typology of events	N_{ev}	$N_{ev}/N_{in\ FV}$
$N_{in\ FV}$	6630	100%
$N_{in\ FV}$ without reconstructed tracks	251	3.8%
$N_{in\ FV}$ with $N_{reco\ in\ FV}$ with multi-Prong vertex	5118	77.2%
$N_{in\ FV}$ with $N_{reco\ out\ FV}$ with multi-Prong vertex	69	1.0%
$N_{in\ FV}$ with $N_{reco\ in\ FV}$ with single-Prong vertex	1052	15.9%
$N_{in\ FV}$ with $N_{reco\ out\ FV}$ with single-Prong vertex	140	2.1%
$N_{in\ FV}$ with $N_{reco\ in\ FV}$	6170	93.1%
$N_{in\ FV}$ with $N_{reco\ out\ FV}$	209	3.2%

Table 5.2: Results of the vertex reconstruction for internal events. In the first column there is the event classification, in the second column the number of events and in the third column the percentage of events respect to $N_{in\ FV}$.

Typology of events	N_{ev}	$N_{ev}/N_{out\ FV}$
$N_{out\ FV}$	9999	100 %
$N_{out\ FV}$ without reconstructed tracks	8592	85.9 %
$N_{out\ FV}$ with $N_{reco\ out\ FV}$ with multi-Prong vertex	87	0.9%
$N_{out\ FV}$ with $N_{reco\ in\ FV}$ with multi-Prong vertex	57	0.6%
$N_{out\ FV}$ with $N_{reco\ out\ FV}$ with single-Prong vertex	1010	10.1%
$N_{out\ FV}$ with $N_{reco\ in\ FV}$ with single-Prong vertex	253	2.5%
$N_{out\ FV}$ with $N_{reco\ out\ FV}$	1097	11.0%
$N_{out\ FV}$ with $N_{reco\ in\ FV}$	310	3.1%

Table 5.3: Results of the vertex reconstruction for external events. In the first column there is the event classification, in the second column the number of events and in the third column the percentage of events respect to $N_{out\ FV}$

In Fig. 5.12 the distribution of the vertex multiplicity for the signal events is shown.

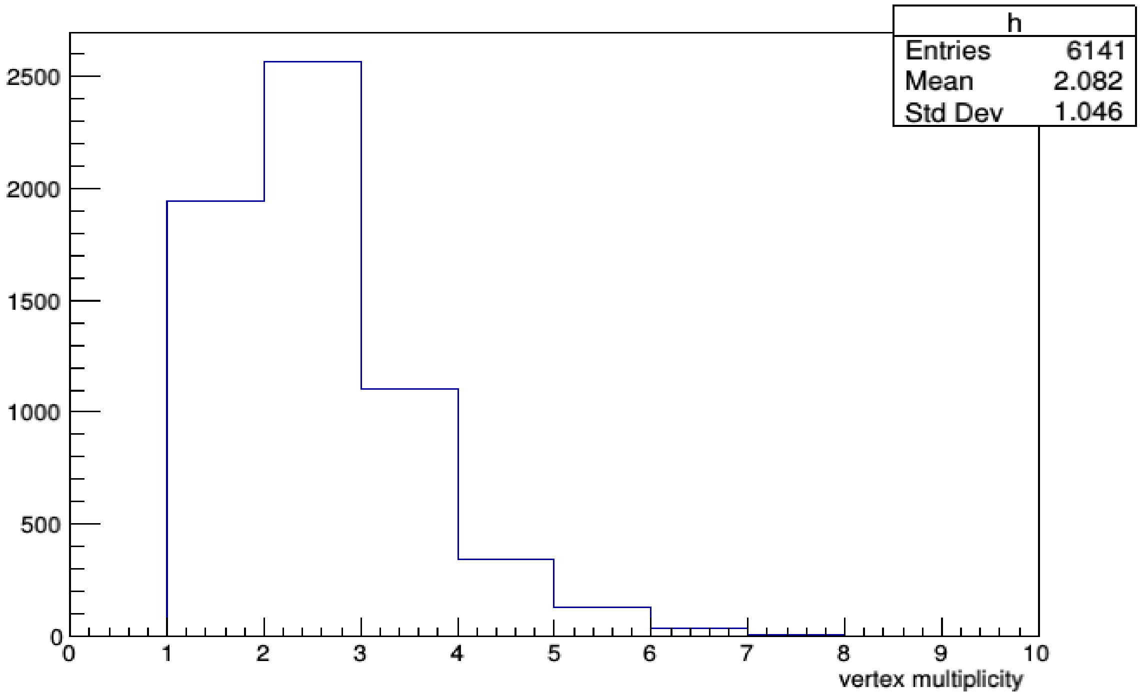

Figure 5.12: Distribution of the vertex multiplicity for the signal events.

In order to characterize the background rejection performance I choose as figure of merit the Signal-to-Background ratio S/B together with the purity P defined as

$$P = \frac{\mathrm{S}}{\mathrm{S} + \mathrm{B}}, \tag{5.3}$$

where the number of expected signal events among internal ones (S) is proportional to

$$S \propto \varepsilon_{int}\ m_{FV}, \tag{5.4}$$

while for the background (B) it is proportional to

$$B \propto \varepsilon_{ext}\ m_{ext} \tag{5.5}$$

The fiducial mass m_{FV}, corresponding to the mass of the STT inside the fiducial volume, is 8237 ± 207 kg while the mass of the remaining parts of the detector, namely the ECAL, the coil, the cryostat and the iron yoke, is 639702 ± 147 kg. The obtained values of ε_{int}, ε_{ext}, S/B and P in the Table 5.4.

ε_{int}	93.06 ± 0.31%
ε_{ext}	3.10 ± 0.02%
S/B	0.26 ± 0.02
P	20.40 ± 1.10%

Table 5.4: ε_{int}, ε_{ext}, S/B and P for the event selection based on the neutrino vertex position.

By looking at the background events, the most common topology consists on single-Prong vertex related to low energy charged particles produced by the interaction of neutral particles entering into the FV from outside. In order to reduce the background component due to this topology, I investigate the number of the crossed module by the primary charged particles of the internal events. The resulting distribution is shown in Fig. 5.13.

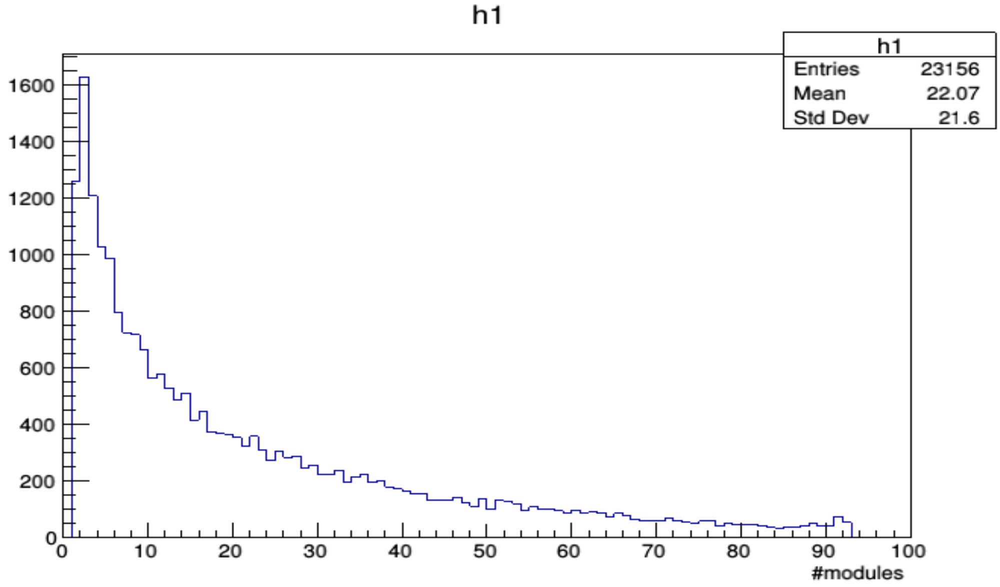

Figure 5.13: Distribution of the number of crossed modules by reconstructed primary tracks in internal events.

Successively I evaluate ε_{int} and S/B for different values of the minimum number of module crossed and the results are shown in Fig. 5.14 - 5.15.

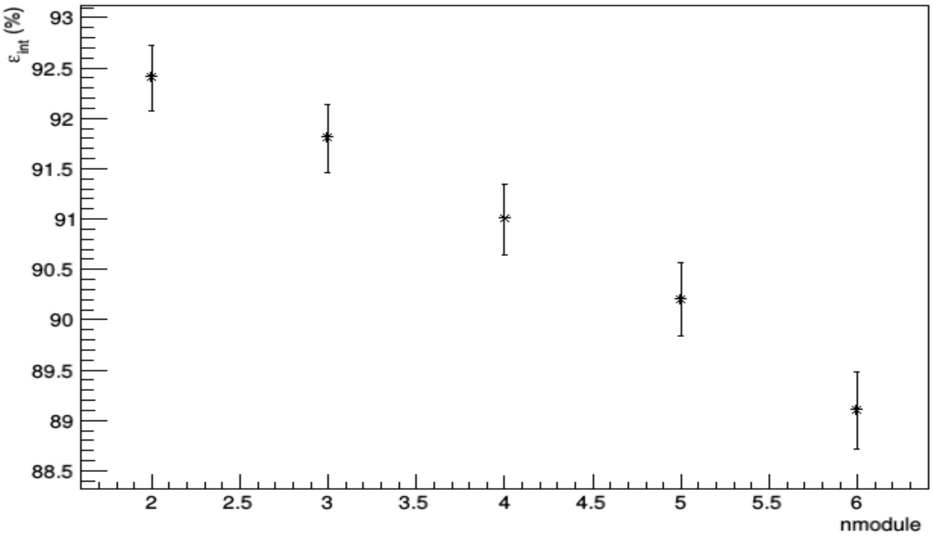

Figure 5.14: ε_{int} as a function of the minimum number of module crossed.

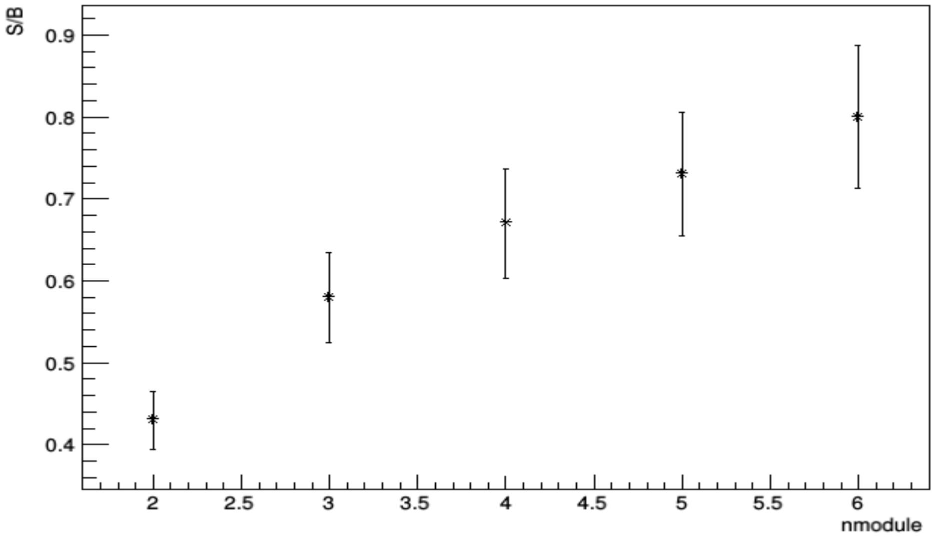

Figure 5.15: S/B as a function of the minimum number of module crossed.

I finally choose a value of the minimum number of crossed modules equal to 5 because it guarantees an $\varepsilon_{int} > 90$ %. The results in term of ε_{int}, ε_{ext} S/B and P applying this selection are shown in Table 5.5.

ε_{int}	$90.19 \pm 0.37\%$
ε_{int}	$1.06 \pm 0.12\%$
S/B	0.73 ± 0.08
P	$42.07 \pm 2.53\%$

Table 5.5: The values ε_{int}, ε_{ext} S/B and P requiring that the tracks used in the vertexing algorithm cross through at least 5 modules.

5.3 Background events

The remaining background events can be grouped into 5 main categories.

- **Single-Prong vertexes from neutral particles**: these events are characterized by a neutral particle that enters into the internal volume of the SAND detector and, interacting with the STT, produces a charged particle (an example is shown in Fig. 5.16). Since there is no reconstructed vertex, the neutrino interaction point is identified as the most upstream digit and, if it is inside the FV, it represents a background event. A possible strategy to reject these events is using the time information of both the STT and the ECAL in order to compare the vertex time to the clusters one; the presence of a cluster with an associated time minor than the vertex one is an indication that the neutrino interaction occurred outside the internal volume of the SAND detector and so the event can be rejected (see Section 5.4).

- **Multi-Prong vertex from a neutral particle interaction**: these events are characterized by a neutral particle entering in the SAND internal region and interacting. The vertexing algorithm reconstructs the position of the interaction of the neutral particles and, if the interaction occurs in the FV, the event is a background one. The thought strategy in order to reject this topology of background is the same described in the previous one.

- **Single-Prong vertexes from entering charged particles**: these events are characterized by a charged particle entering in the SAND detector. Since there is no reconstructed vertex, the algorithm identifies the vertex as the most upstream digit; if this digit is inside the FV the event is background (an example is shown in Fig. 5.17). In order to reject these events, together with the strategy already seen and described in the previous points, an additional one can be applied. In fact, exploiting the time STT digits information it is possible to reconstruct the particle direction along the track; the presence of an incoming track indicates that the charged particle has entered in the SAND internal volume, so the neutrino interaction occurred outside and event can be rejected (see Section 5.5).

- **Multi-Prong vertex from a charged particle interaction**: these event are characterized by a charged particle entering in the SAND internal region and interacting. The vertexing algorithm reconstructs the position of the charged particle interaction and so, if the interaction occurs in the FV, the event is a background one (an example is shown in Fig. 5.18). The thought strategies that can be applied in order to reject these events are the same described in the previous point.

- **Entering-exiting charged particle**: these events are characterized by a charged particle that enters in the SAND internal region from downstream and then, affected by the magnetic field $\vec{B}$, changes its direction and exits forward from the SAND downstream region. Since there is no reconstructed vertex, the neutrino interaction point is identified as the most reconstructed upstream digit and, if it inside the SAND internal volume, the event is a background one (an example is shown in Fig. 5.20). The thought strategies in order to reject these events are the same of the last two point of this list.

In Table 5.6 are summarized the different topologies of background events.

Typology of event	Number of events	Percentage
single-Prong vertex from neutral particle	45	42%
single-Prong vertex form charged particle	35	33%
multi-Prong vertex from charged particles	12	11%
multi-prong vertex from neutral particles	5	4.7%
entering-exiting charged particle	4	3.8%

Table 5.6: The topologies of the background events, the number of each toplogy and their percentage respect to the total number of the background events.

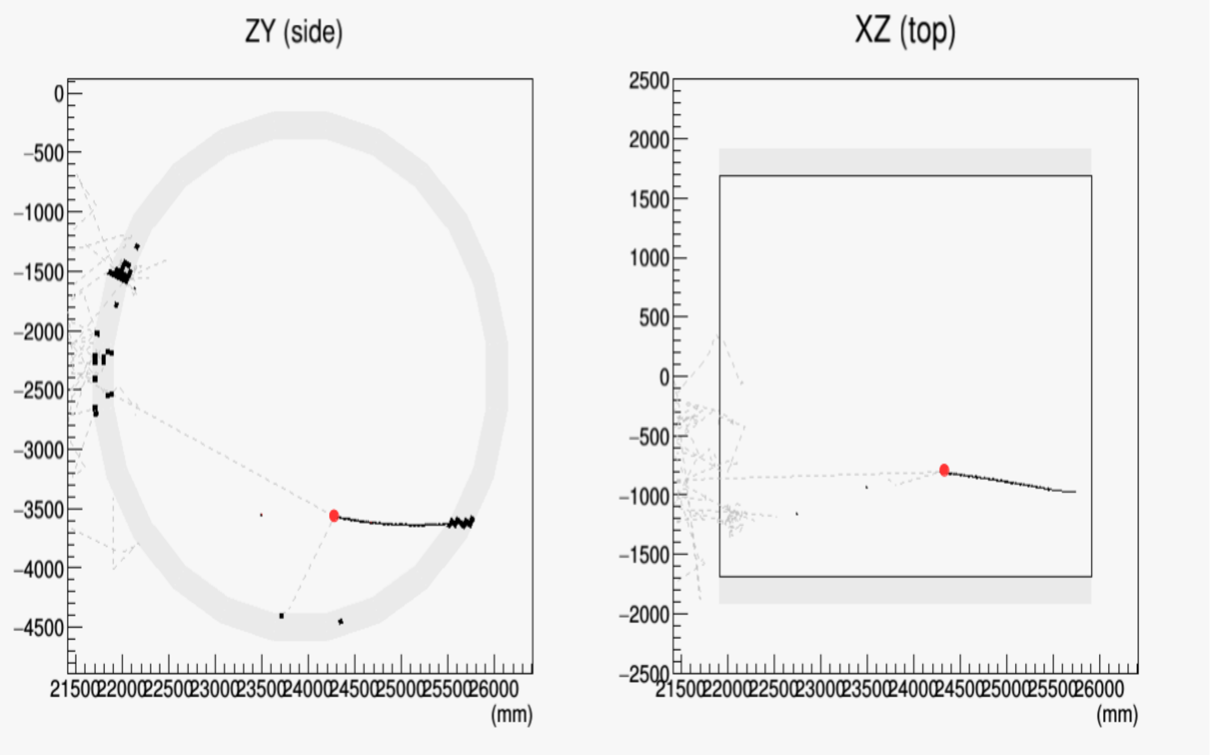

Figure 5.16: The zy and the zx views of an external event with the neutrino vertex reconstructed inside the FV. It can be noticed, specially in the zy view, how the neutron, represented with the dashed gray line, enters inside the SAND volume and interacts producing a proton, the black continue line, whose upstream digit is identified by the algorithm as the neutrino vertex (represented as a red circle).

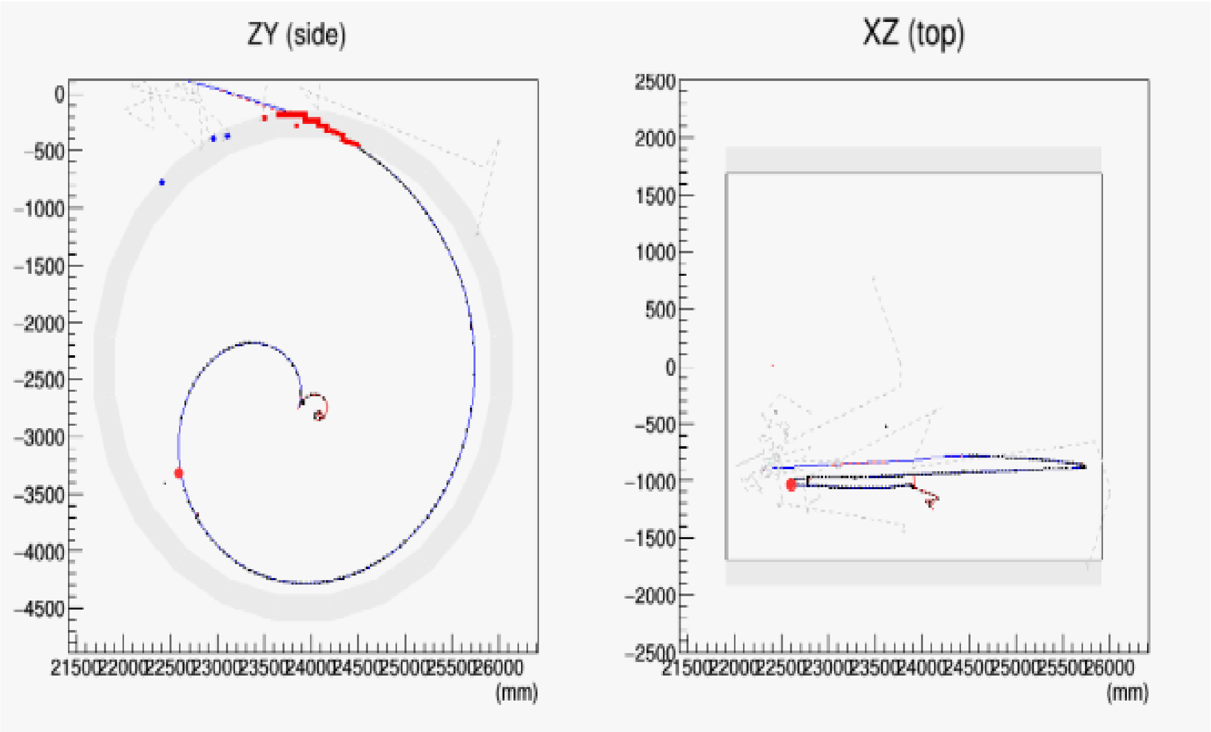

Figure 5.17: The zy and the zx views of an external event with the neutrino vertex reconstructed inside the FV. It can be noticed in the zy view how the muon, represented with the dashed blue continuos line, enters inside the SAND volume and follows a circular path due to the magnetic field $\vec{B}$ directed along the x axis. The upstream digit related to the muon is identified by the algorithm as the neutrino vertex (represented as a red circle).

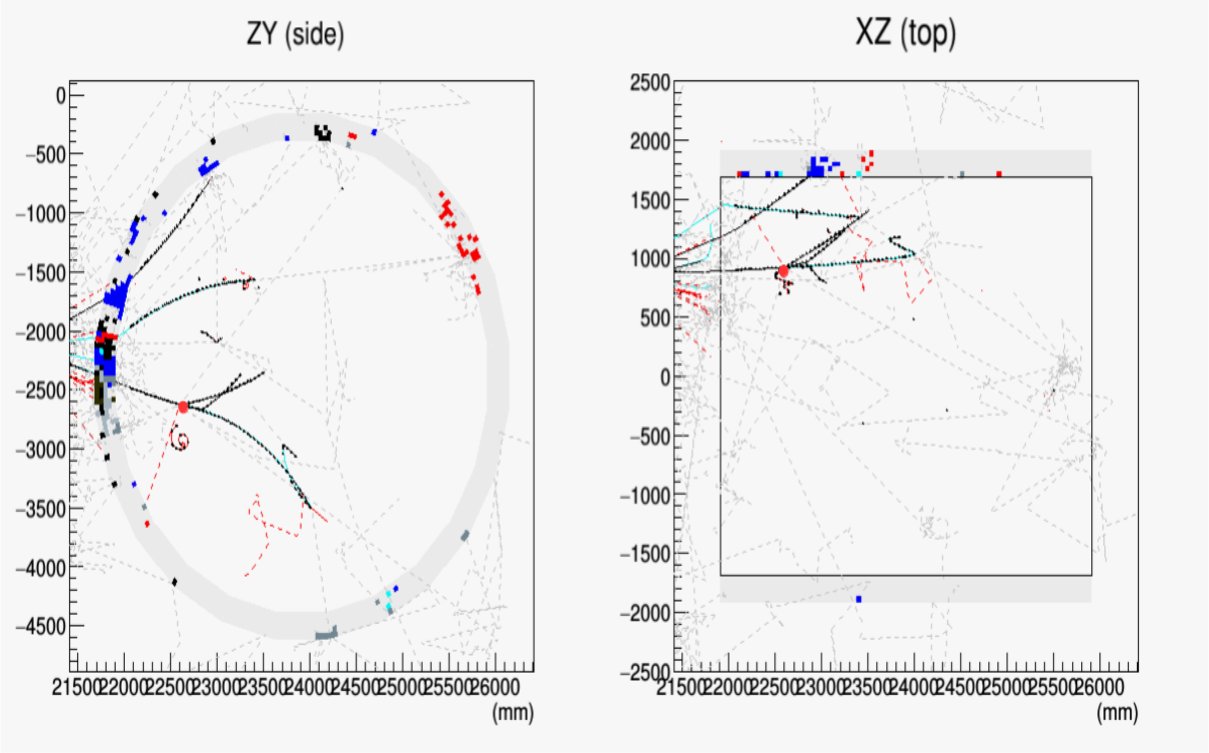

Figure 5.18: The zy and the zx views of an external event with the neutrino vertex reconstructed inside the FV. It can be noticed in the zx view how the proton, represented with the continuous line, enters inside the SAND volume interacts producing several charged particle (a pion, represented as cyan continuous line, an electron, represented as a red continuous line and a proton, represented as a black continuous line). The algorithm misidentifies the proton interaction point (represented as a red circle) as the neutrino vertex.

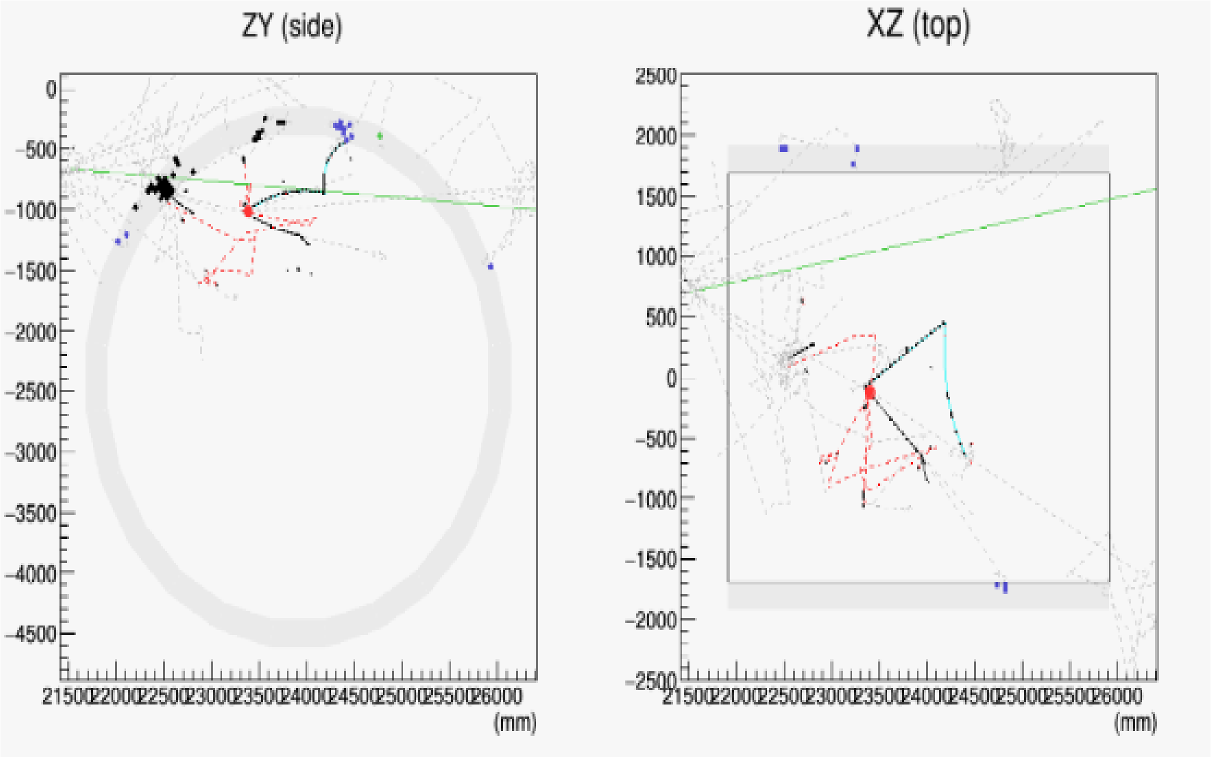

Figure 5.19: The zy and the zx views of an external event with the neutrino vertex reconstructed inside the FV. It can be noticed in the zx view how the neutron, represented with the dashed gray line, enters inside the SAND volume and interacts producing several charged particle (a pion, represented as cyan continuous line and a proton, represented as a black continuous line). The algorithm misidentifies the neutron interaction point (represented as a red circle) as the neutrino vertex.

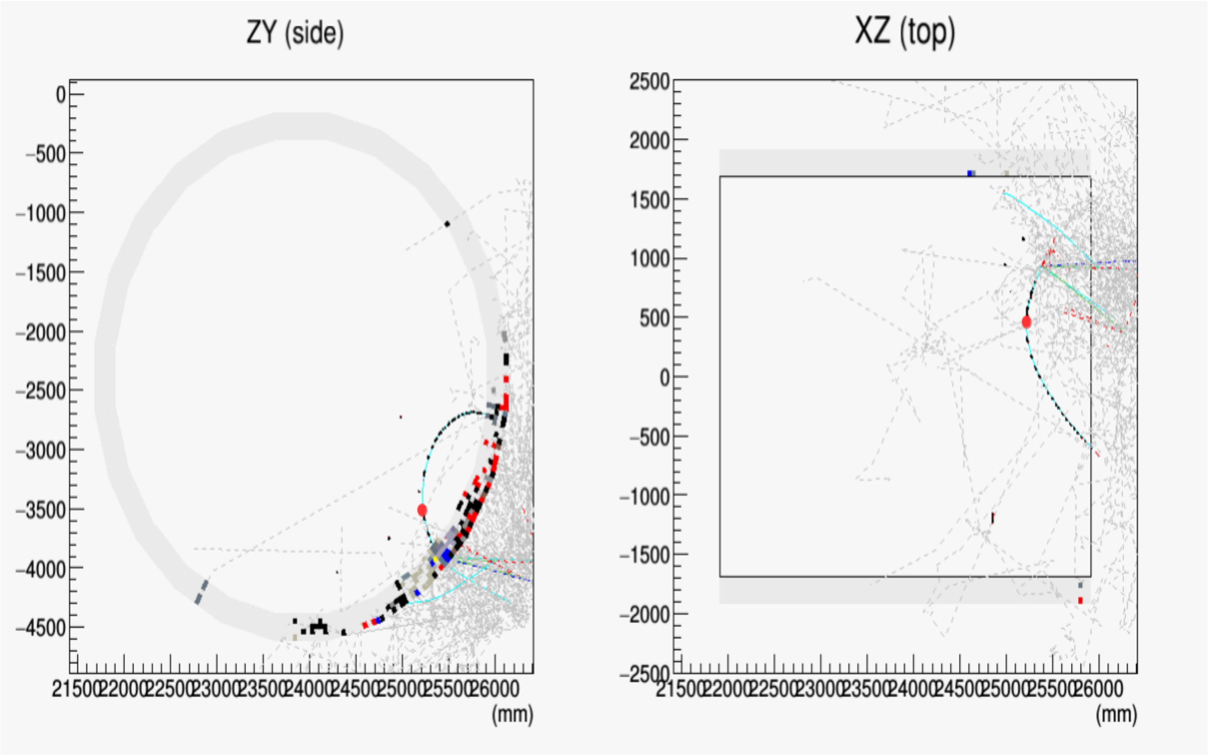

Figure 5.20: The zy and the zx views of an external event with the vertex reconstructed inside the FV. It can be noticed, specially in the zy view, how the pion, represented with the continuous cyan line, enters backward in the SAND volume from downstream, changes it direction and then exits forward from the SAND downstream region. The neutrino vertex reconstructed by the algorithm is represented as a red circle and coincides with the most upstream digit belonging to the track.

5.4 Timing cut

The rejection of the background events can be improved by using timing information. To this aim, firstly I simulate the time resolution of the STT detector applying a Gaussian smearing on the time information of the STT digits ($\sigma_{STT} \sim 1$ ns)

$$t_{dig} = t_{\mathrm{MC}} + \mathbf{Gaus}(1\mathrm{ns}), \tag{5.6}$$

where **Gaus**(1 ns) is a random term that follows a Gaussian distribution with mean equal to 0 and σ to 1 and t_{MC} is the true MC time of the hit associated to the digit. The time of the neutrino vertex t_v is estimated in the following ways:

- for single-Prong vertex t_v is the time of the digit used to define the vertex position;
- for multi-Prong vertex t_v is the mean of the time of the upstream digit of the tracks belonging to the neutrino vertex.

Then for each event, I check if there is a cluster for which

$$t_v - t_{cl} > 3 \text{ ns}, \tag{5.7}$$

where t_{cl} is the time of the ECAL cluster. In this case, the event is classified as background. The value of 3 ns is chosen in order to guarantee that the vertex time is minor than the cluster time at $>$ 99% C.L., taking into account that the single digit STT timing resolution is $\sigma_{\mathrm{STT}} \sim 1$ ns. The results in term of $\varepsilon_{\mathrm{int}}$, $\varepsilon_{\mathrm{ext}}$ S/B and P applying the timing cut, in addition to the already discussed ones, are shown in Table 5.7.

$\varepsilon_{\mathrm{int}}$	87.50 ± 0.41%
$\varepsilon_{\mathrm{ext}}$	0.33 ± 0.06%
S/B	2.26 ± 0.40
P	69.4 ± 3.8%

Table 5.7: The values $\varepsilon_{\mathrm{int}}$, $\varepsilon_{\mathrm{ext}}$ S/B and P applying the timing cut.

5.5 Track direction cut

Finally, I study the possibility to reconstruct the particle direction along the track in order to identify vertex with incoming tracks. To this aim I firstly reconstruct the ends of the tracks in both the zy and zx planes in order to estimate the track length (Section 5.5.1), then I determine the particle direction along trajectory in both vertical and horizontal planes using the time information of the digits. The track length reconstruction is a crucial step in order to find a minimum value of the length for which the reconstructed direction is reliable; for short track this is not possible due to the STT time resolution ($\sigma_{STT} \sim 1$ ns). Finally I apply a cut exploiting these information (Section 5.5.2).

5.5.1 Track length

The track length is determined calculating the length of the arc of circumference dl described by the the charged particle in the zy plane, perpendicular to the magnetic field $\vec{B}$ directed along the x axis, and the corresponding path length along the x axis, dx. The track length L is calculated as

$$L = \sqrt{dl^2 + dx^2} \tag{5.8}$$

To calculate the dl and dx values I find the ends of the track in both the zy and zx planes. To this aim, I firstly calculate, for all the recorded digits by the horizontal STT planes (referred to as horizontal digits), the angle respect to the the center (z_c, y_c) of the circumference found in the circular fit described in the track reconstruction step in Section 4.5.2. Then I define the ends as the digits that have the larger angular distance α: the initial and the end point are the one with the minor and major angle respectively. The other digits are ordered consistently with respect to the choice of the ends. Subsequently I find the ends in the zx plane as the digits recorded by the vertical STT planes (referred to as vertical digits) that had the maximum ($x_{\max}$) and the minimum ($x_{\min}$) value of the x coordinate; the vertical digits are so ordered in order to have an array with an increasing value of the x coordinate associated. So dl and dx are calculated respectively as

$$dl = \alpha R, \tag{5.9}$$

where R is the radius found in the circular fit described in the track reconstruction described in Section 4.5.2, and as

$$dx = |x_{\max} - x_{\min}|. \tag{5.10}$$

5.5.2 Track direction reconstruction

Once the track length has been calculated I proceed in the determination of the track direction using the time information of the STT digits. Starting from the initial end I calculate, for both the horizontal and vertical digits, the following time differences

$$\Delta t_{ij} = t^i_{dig} - t^j_{dig} \text{ with } i, j = 1, .., n \text{ and } i < j, \tag{5.11}$$

where n is the number of the digits. The sign of the mean value

$$\Delta t_{\text{mean}} = \frac{\sum^N \Delta t_{ij}}{N}, \tag{5.12}$$

where $N = \frac{n(n-1)}{2}$ is the number of the time differences Δt_{ij}, indicates the track direction. The distribution of Δt_{mean} for the zy and the x direction versus the track length is shown in Fig. 5.21 and 5.22 respectively. It can be noticed how the difference of Δt_{mean} from zero increases with the track length; for the long tracks the direction is well defined. On the other hand, it is not possible to evaluate direction for short tracks.

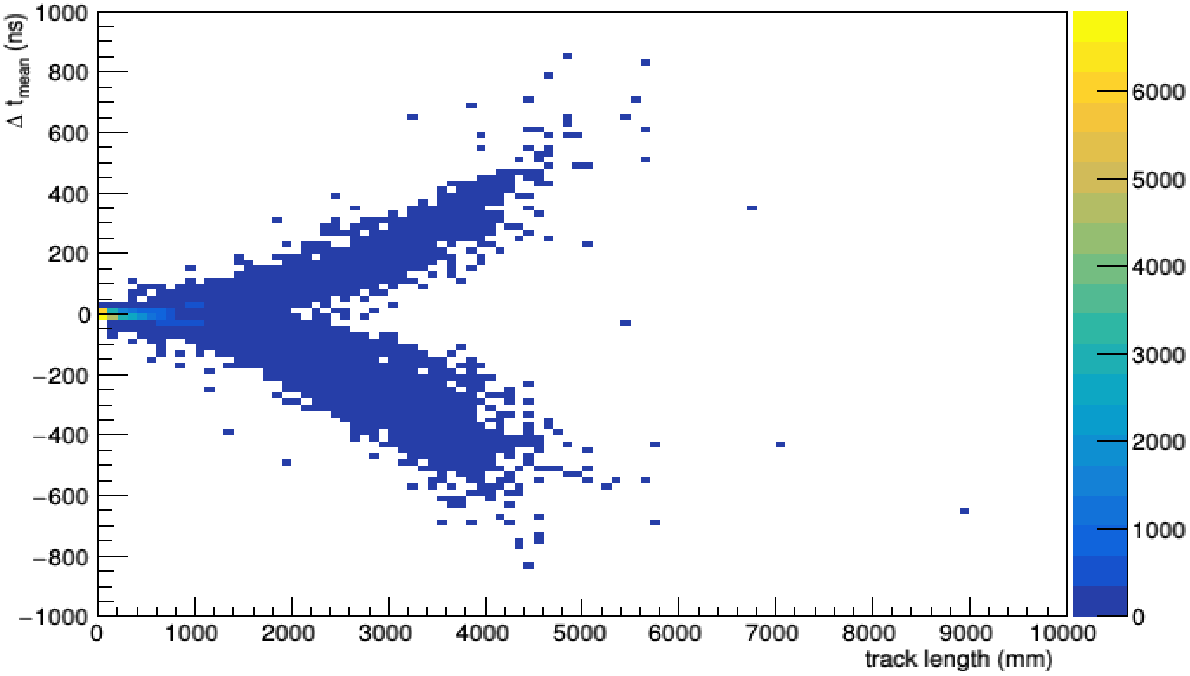

Figure 5.21: Distribution of Δt_{mean} versus the track length for the zy view.

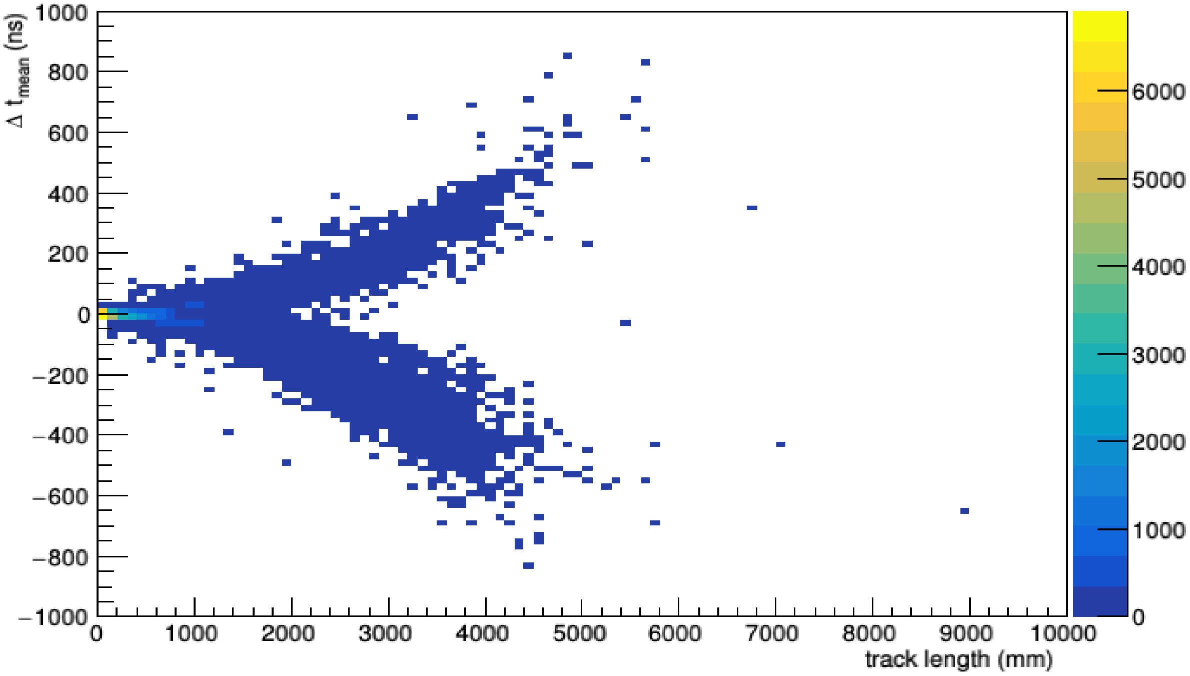

Figure 5.22: Distribution of Δt_{mean} versus the track length for the zx view

In order to identify a reasonable value of the minimum track length for which the reconstructed direction is reliable, I define the following figure of merit:

$$\varepsilon_{\mathrm{dir\ reco}}(L') = \frac{N_{\mathrm{dir\ reco}}(L')}{N(L')} \tag{5.13}$$

where $N_{\mathrm{dir\ reco}}(L')$ is the number of tracks with the direction correctly reconstructed with $L > L'$, and $N(L')$ is the number of tracks with $L > L'$. $N_{\mathrm{dir\ reco}}(L')$ is evaluated comparing the sign of Δt_{mean} with the sign of the time difference between the digit t_{MC} (see Section 5.4, Eq. 5.6) corresponding to the ends of the track: if the two signs coincide the track direction is correctly reconstructed, otherwise no. The values of $\varepsilon_{\mathrm{dir\ reco}}$ for the zy and the x direction are shown in Fig. 5.23 and 5.24 respectively.

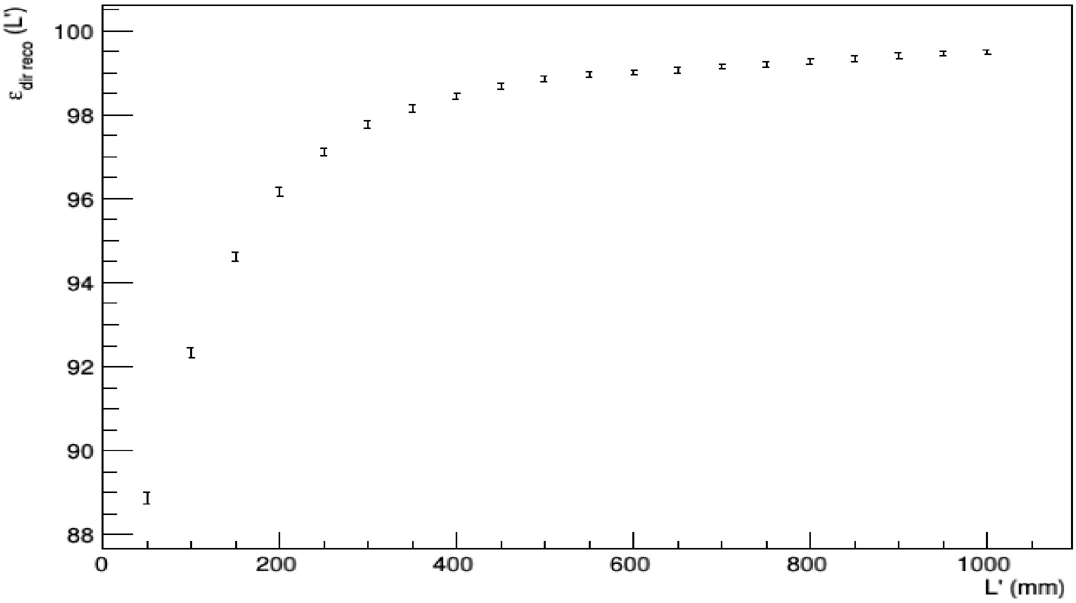

Figure 5.23: $\varepsilon_{\text{dir reco}}$ as a function of L' for the zy view.

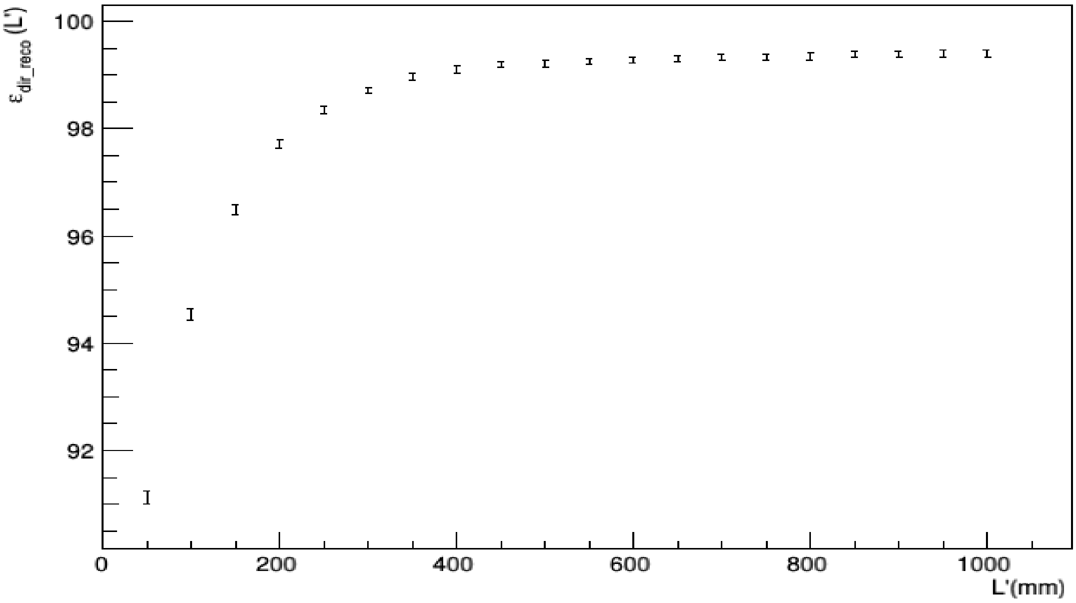

Figure 5.24: $\varepsilon_{\text{dir reco}}$ as a function of L' for the zx view.

Therefore I apply a cut to the event selection exploiting the reconstructed direction; all the events with a vertex to which is associated an incoming track, for both the zy and the x direction, with $L > 600$ mm and with the first end outside the FV are tagged as background events. The 600 mm value is chosen because for all the tracks with $L > 600$ mm, $\varepsilon_{\text{dir reco}} > 99\%$, for both the the zy and x directions. The results in term of ε_{int}, ε_{ext}, S/B and P are listed in Table 5.8.

ε_{int}	87.47 ± 0.41%
ε_{ext}	0.28 ± 0.05%
S/B	2.67 ± 0.51
P	72.73 ± 3.82%

Table 5.8: The values ε_{int}, ε_{ext} S/B and P applying the direction and timing cut.

Conclusions and outlooks

The study of the neutrino physics is of crucial importance in modern particle physics; finding answers to the still open questions about neutrinos will be a fundamental step in making the Standard Model a more complete theory. The DUNE experiment, thanks to its precision in the measurement of the parameters that rule the neutrino oscillations, will be able to shed light to some pending questions about neutrino physics such as the determination of the δ_{CP} and of the mass ordering. It will be composed of a Near Detector system,located a few hundred meters from the neutrino source at the FNAL, and a Far Detector system composed of four multikiloton LArTPCs, located at the Sandford Underground Research Facility site (SouthDakota) 1300 km far from the beam source.

The SAND detector will be one of the three detectors composing the Near Detector system. Its main aim is to characterize and monitor the neutrino beam. For this purpose, it is of crucial importance to distinguish the neutrino interactions that occur in the SAND detector internal region from the external background. In this work of thesis I define and implement strategies for the identification of neutrino interactions occurring in the internal region of the SAND detector. Moreover, I evaluate their performance in terms of purity and signal-to-background ratio. In order to perform this study a sample of 10000 NC and CC ν_μ interaction occurring inside the SAND detector internal region and a sample of 10000 NC and CC ν_μ interactions occurring outside the SAND detector internal region is simulated. The events for which the neutrino interaction occurs in the SAND internal region are signal, while the events for which the neutrino interaction occurs outside the SAND internal region and misidentified as internal are background. The identification of the event is based firstly on their topology; to this aim a vertexing algorithm that exploits the STT signals spatial information is developed. The algorithm reconstruct the neutrino vertex and its position. The results in term of the figure of merit signal-to-background ratio (S/B) and of purity (P) in the selection of the signal events are 0.26 ± 0.02 and $20.4 \pm 1.1\%$. In a second phase, to improve the capability of excluding the background events, a further selection which exploits the time information of both the STT and ECAL is applied. The results considerably improve reaching a value of S/B and P equal to 2.67 ± 0.51 and $72.73 \pm 3.82\%$ respectively.

The results are really promising but further improvements can be achieved; for example, exploiting the association of STT track with ECAL cluster and their time and energy correlation.

Bibliography

[1] S.T.Petcov, "The Nature of Massive Neutrinos", in *Adv. High Energy Phys.*, vol. 2013, p. 852987, 2013.

[2] K.Zuber, "Neutrino Physics", Second Edition, edited by CRC Press, 2011.

[3] M.Goldhaber et L.Grodzins et A.W.Sunyar, "Helicity of Neutrinos", in *Phys.Rev.*, vol. 109, pp. 1015-1017, 1958.

[4] C.Giunti et C.W.Kim, "Fundamentals of Neutrino Physics and Astrophysics", edited by Oxford University Press, 2007.

[5] S.T.Petcov, "The Nature of Massive Neutrinos", in *Adv. High Energy Phys.*, vol. 2013, p. 852987, 2013.

[6] G.B.Franklin, "The KATRIN Neutrino Mass Measurement: Experiment, Status, and Outlook", *in 13th Conference on the Intersections of Particle and Nuclear Physics (CIPANP 2018) Palm Springs, California, USA, May 29-June 3, 2018*. 2018.

[7] C.Kraus et al., "Final results from phase II of the Mainz neutrino mass search in tritium beta decay", in *Eur.Phys.J*, vol.C40, pp.447-468, 2005.

[8] V.N.Aseev et al., "An upper limit on electron antineutrino mass from Troitzk experiment",in *Phys.Rev.*, vol.D84, p. 112003, 2011.

[9] M. Tanabashi et al. "Particle Data Group", in *Phys. Rev.* D 98, 030001 (2018)

[10] Y. Farzan et M. Tortola, "Neutrino oscillations and Non-Standard Interactions" in *Phys.vol.6*, p.10, 2018.

[11] Stefania Ricciardi, "Lecture notes on Neutrino oscillations in matter", 6/10/2013

[12] L. Wolfenstein, "Neutrino oscillations in matter", in *Phys.Rev.* D 17, 2369, 1978.

[13] S.P. Mikheyev, A.Yu. Smirnov, "Resonance Amplification of Oscillations in Matter and Spectroscopy of Solar Neutrinos", in *Sov. J. Nucl. Phys.*, vol. 42, pp. 913-917, 1985.

[14] F. Capozzi, E. Di Valentino, E. Lisi, A. Marrone, A. Melchiorri, et A. Palazzo, "Global constraints on absolute neutrino masses and their ordering", in *Phys. Rev.*, vol.D95, no.9, p. 096014, 2017.

[15] K. Lande and P. Wildenhain, "The Homestake chlorine solar neutrino experiment:past, present and future", Nuclear Physics B - Proceedings Supplements, vol. 118, pp. 49-54, 2003.

[16] M. Altmann and Others, "Complete results for five years of GNO solar neutrino observations", *Physics Letters B*, vol. 616, no. 3, pp. 174 - 190, 2005.

[17] J. N. Abdurashitov, E. P. Veretenkin, V. M. Vermul, V. N. Gavrin, S. V. Girin, V. V. Gorbachev, P. P. Gurkina, G. T. Zatsepin, T. V. Ibragimova, A. V. Kalikhov, and et al., "Solar neutrino flux measurements by the soviet-american gallium experiment (sage) for half the 22-year solar cycle", in *Journal of Experimental and Theoretical Physics*, vol. 95, pp. 181-193, 2002.

[18] Q. R. Ahmad et al., "Direct evidence for neutrino flavor transformation from neutral current interactions in the Sudbury Neutrino Observatory", *Phys. Rev. Lett.*, vol. 89, p. 011301, 2002.

[19] Kamiokande-II, K. S. Hirata et al., "Real time, directional measurement of B-8 solar neutrinos in the Kamiokande-II detector", in *Phys. Rev.* D45, 2170, 1992.

[20] Y. Suzuki, "The Super-Kamiokande experiment", *The European Physical Journal C*, vol. 79, 2019.

[21] G. Giacomelli, "Neutrino physics and astrophysics with the MACRO experiment at the Gran Sasso lab", in *Braz. J. Phys.*, vol. 33, pp. 211 - 217, 2003.

[22] Adrian-Martinez et al., "Measurement of Atmospheric Neutrino Oscillations with the ANTARES Neutrino Telescope", *Phys. Lett.* B714, 224-230, 2012.

[23] M.G.Aartsen et al., "Measurement of Atmospheric Neutrino Oscillations at 6-56 GeV with IceCube DeepCore", arXiv:1707.07081.

[24] S. Boyd, "Recent results from the k2k (kek-to-kamioka) neutrino oscillation experiment",in *Nuclear Physics B - Proceedings Supplements*, vol. 98, pp. 175 - 181, Apr 2001.

[25] J. Evans, "The MINOS Experiment: Results and Prospects", in *Adv. High Energy Phys.*, vol. 2013, p. 182537, 2013.

[26] G. Alimonti et al., "The Borexino detector at the Laboratori Nazionali del Gran Sasso", in *Nuclear Instruments and Methods in Physics Research Section A: Accelerators, Spectrometers, Detectors and Associated Equipment*, vol. 600, pp. 568-593, 2009.

[27] S. Abe, T. Ebihara, S. Enomoto, K. Furuno, Y. Gando, K. Ichimura, H. Ikeda, K. Inoue, Y. Kibe, Y. Kishimoto, and et al., "Precision measurement of neutrino oscillation parameters with Kamland",in *Phys. Rev.*, vol. 100, 2008.

[28] I. Esteban, M. C. Gonzalez-Garcia, A. Hernandez-Cabezudo, M. Maltoni, T. Schwetz, "Global analysis of three-flavour neutrino oscillations: synergies and tensions in the determination of θ_{23} ; δ_{CP} , and the mass ordering", in *JHEP* vol. 01, p. 106, 2019.

[29] F. P. An et al., "Measurement of electron antineutrino oscillation based on 1230 days of operation of the Daya Bay experiment", in *Phys. Rev.,*vol. D95, no. 7, p. 072006, 2017.

[30] S. H, Seo et al., "Spectral Measurement of the Electron Antineutrino Oscillation Amplitude and Frequency using 500 Live Days of RENO Data" in *Phys. Rev.,* vol. D98, no. 1, p. 012002, 2018.

[31] A.Maregaglia, "Multi detector results from the Double Chooz experiment" *Proceedings, 52nd Rencontres de Moriond on Electroweak Interactions and Unified Theories: La Thuile, Italy, March 18-25, 2017,* pp. 359-366, 2017.

[32] M. Apollonio et al., "Search for Neutrino Oscillations on a Long Base-Line at the CHOOZ Nuclear Power Station." in *Eur. Phys. Journ*, vol.C27.3, pp. 331-374, 2003.

[33] F. Boehm et al., "Final Results from the Palo Verde Neutrino Oscillation Experiment." in *Phys. Rev.* vol. D64, no. 11, (2001).

[34] OPERA collaboration , "Discovery of tau neutrino appearance in the CNGS neutrino beam with the OPERA experiment", in *Phys. Rev. Lett.*, vol. 115, 121802 (2015)

[35] K.Abe et al., "Measurement of neutrino and antineutrino oscillations by the T2K experiment including a new additional sample of ν_e interactions at the far detector" in *Phys. Rev. D,* vol. 96, p. 092006, Nov 2017.

[36] Lee-Franzini et al."The KLOE electromagnetic calorimeter",in *Nuclear Instruments and Methods in Physics Research Section A: Accelerators, Spectrometers, Detectors and Associated Equipment.* 360. 201-205. 10.1016/0168-9002(94)01607-0, 1995.

[37] R.Acciarri et al., "Long-Baseline Neutrino Facility (LBNF) and Deep Underground Neutrino Experiment (DUNE) Conceptual Design Report Volume 1: The LBNF and DUNE Projects" in arXiv:1601.05471 [physics.ins-det], Jan 2016.

[38] DUNE Collaboration, "Long-Baseline Neutrino Facility (LBNF) and Deep Underground Neutrino Experiment (DUNE) Conceptual Design Report Volume 2: The Physics Program for DUNE at LBNF", in arXiv:1512.06148 [physics.ins-det], Jan 2016.

[39] DUNE Collaboration, "Long-Baseline Neutrino Facility (LBNF) and Deep Underground Neutrino Experiment (DUNE) Conceptual Design Report Volume 3: Long-Baseline Neutrino Facility for DUNE", in arXiv:16012.05823 [physics.ins-det], Jan 2016.

[40] DUNE Collaboration, "Long-Baseline Neutrino Facility (LBNF) and Deep Underground Neutrino Experiment (DUNE) Conceptual Design Report Volume 4: The DUNE Detectors at LBNF" in arXiv:1601.02984 [physics.ins-det], Jan 2016.

[41] DUNE Collaboration, "Deep Underground Neutrino Experiment (DUNE), Far Detector Technical Design Report, Volume II: DUNE Physics" in arXiv:2002.03005 [hep-ex] , Feb 2020.

[42] DUNE Collaboration, "Deep Underground Neutrino Experiment (DUNE), Far Detector Technical Design Report, Volume I: Introduction to DUNE" in arXiv:2002.02967 [physics.ins-det], Feb 2020.

[43] Argoncube Website. https://argoncube.org/duneND.html.

[44] M. Auger et al. [ArgonCube Collaboration], "ArgonCube: a Modular Approach for Liquid Argon TPC Neutrino Detectors for Near Detector Environments", CERN-SPSC-2017-025. SPSC-I-246 (2017), available at https://cds.cern.ch/record/2268439, accessed: 2018-09-29.

[45] LBNE Collaboration, "The Long-Baseline Neutrino Experiment: Exploring Fundamental Symmetries of the Universe" in arXiv:1307.7335 [hep-ex], Apr 2014.

[46] GLoBES software.https://www.mpi-hd.mpg.de/personalhomes/globes/

[47] G.Adamov et al., "Proposal to enhance the DUNE Near-Detector Complex", DUNE Document Database, DUNE-doc-13262, 2019

[48] G.P.Zeller et al., "A Precise determination of electroweak parameters in neutrino nucleon scattering", *Phys. Rev. Lett.,* vol. 90, pag. 239902, 2002.

[49] William J.Marciano and Zohreh Parsa, "Neutrino electron scattering theory", J. Phys., G29: pag.2629-2645, 2003.

[50] Stephen L. Adler, "Tests of the Conserved Vector Current and Partially Conserved Axial-Vector Current Hypotheses in High-Energy Neutrino Reactions", in *Phys. Rev.,* vol 136, pag.B963-B966, 1964.

[51] David J. Gross and Chris H. Llewellyn Smith, "High-energy neutrino - nucleon scattering, current algebra and partons", in *Nucl. Phys.*, B14:337-347, 1969.

[52] Sergey Alekhin, Johannes Blümlein, Sergey Kulagin, Sven-Olaf Moch, and Roberto Petti, "Strange and non-strange distributions from the collider data", *PoS*, DIS2018:008, 2018.

[53] P Astier et al., "Final NOMAD results on muon-neutrino - tau-neutrino and electron-neutrino - tau-neutrino oscillations including a new search for τ-neutrino appearance using hadronic tau decays", in *Nucl. Phys.,* vol. B611, pag 3-39, 2001.

[54] https://cdcvs.fnal.gov/redmine/projects/dune-neardet-design/wiki/DUNE_NearDet_Design

[55] https://github.com/gyang9/dunendggd

[56] https://github.com/brettviren/gegede

[57] https://home.fnal.gov/ljf26/DUNEFluxes

[58] Costas Andreopoulos et al., "The GENIE Neutrino Monte Carlo Generator: Physics and User Manual" in arXiV:1510.05494 [hep-ph], 2015.

[59] https://github.com/ClarkMcGrew/edep-sim

[60] https://zenodo.org/record/1314669#.X1jo_nUzY8o

[61] A.Andreazza, "Tracking Systems", Lecture notes from *"Acceleratori di Particelle"*, Dipartimento di Fisica, Universitá degli studi di Milano, http://www2.fisica.unimi.it/andreazz/AA TrackingSystems.pdf